WYVERN

42nd Annual VFS Student Design Competition

Pioneering Hydrogen-Electric VTOL

Sponsored by: AIRBUS

UNIVERSITY OF MARYLAND

Alfred Gessow Rotorcraft Center
Department of Aerospace Engineering
University of Maryland
College Park, MD 20742 U.S.A.

Alfred Gessow Rotorcraft Center
Department of Aerospace Engineering
University of Maryland
College Park, MD 20742

Kumardip Basak
Graduate Student (Team Lead)
kbasak@umd.edu

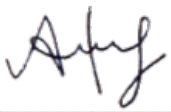

Apurva Anand
Graduate Student
apurva01@umd.edu

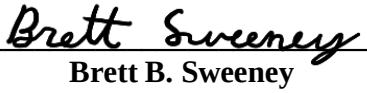

Brett B. Sweeney
Graduate Student
bsweens@umd.edu

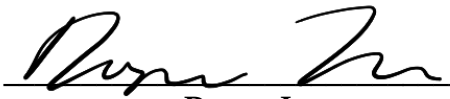

Dogyu Jun
Graduate Student
djun1127@umd.edu

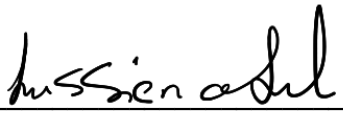

Hussein A. A. H. Hussien
Graduate Student
hhussien@umd.edu

Jacob C. McCallum
Graduate Student
jmccall2@umd.edu

Radu Teodorescu
Graduate Student
rteodore@umd.edu

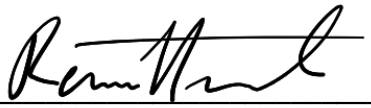

Remi J. Hensel
Graduate Student
henselr@umd.edu

William M. Ogle
Graduate Student
wogle@umd.edu

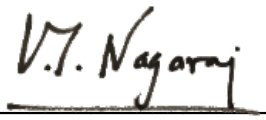

Dr. Vengalattore T. Nagaraj
Faculty Advisor
vnagaraj@umd.edu

Dr. Inderjit Chopra
Faculty Advisor
chopra@umd.edu

Dr. Anubhav Datta
Faculty Advisor
datta@umd.edu

Academic Course:
ENAE634: Helicopter Design (3 credits)

ACKNOWLEDGEMENTS

The UMD graduate design team acknowledges the following people for their invaluable discussion, guidance, and support throughout this project.

Dr. Andreas Bernhard — Director, Tech Road Maps, Advanced Development Programs, Lockheed Martin Aeronautics

Dr. Mrinalgouda Patil — Loads and Dynamics Engineer, Joby Aviation

Prof. James D. Baeder — Igor Sikorsky Distinguished Professor in Rotorcraft, Department of Aerospace Engineering

Prof. Umberto Saetti — Assistant Professor, Department of Aerospace Engineering

Tomasz Krysinski — Visiting Scientist, Department of Aerospace Engineering

Vivek Uppoor — Graduate Student, Alfred Gessow Rotorcraft Research Center

Sridatta Satuluri — Graduate Student, Alfred Gessow Rotorcraft Research Center

Logan Swaisgood — Graduate Student, Alfred Gessow Rotorcraft Research Center

Matt Arace — Graduate Student, Alfred Gessow Rotorcraft Research Center

Muneeb Safdar — Graduate Student, Alfred Gessow Rotorcraft Research Center

Nathan O'Brien — Graduate Student, Alfred Gessow Rotorcraft Research Center

Alfred Gessow Rotorcraft Center
Department of Aerospace Engineering
University of Maryland
College Park, MD 20742 U.S.A.

To the Vertical Flight Society:

The members of the University of Maryland Graduate Student Design Team hereby grant VFS full permission to distribute the enclosed Executive Summary and Final Proposal for the 42nd Annual Design Competition as they see fit.

Thank you,

The UMD Graduate Design Team

Contents

List of Figures

List of Tables

RFP Deliverable	**Source**	**Section/Figure**
Trade Studies	RFP 2.4.1	2, 3
Configuration choice		2
Rotor design		6, 7
Powerplant selection		12
Transmission design		13
Wing design		9
Fuselage design		11
Vehicle Performance	RFP 2.4.2	17
Total power		17.8
Aerodynamic power		17.8
Transmission efficiency		17.8
Motor RPM/Torque		17.8
PEMFC efficiency		17.8
Hydrogen flow rate and consumption		17.8
Maximum level flight speed		17.5
HOGE ceiling diagram		17.4
Required shaft power breakdown		17.5
V_{be} and V_{br}		17.5
Weight & Balance	RFP 2.4.3	15
Component weight breakdown		15
Weight and CG evolution		Fig. 15.1
Center of gravity analysis		15
Aerodynamic Metrics	RFP 2.4.4	17
D/q, and M/q at zero degrees vehicle pitch and yaw		17.3
Drag estimation		17.1
Airframe aerodynamic L/D and performance graph		17.3, 17.5, 17.4
Vehicle Drawings	RFP 2.4.5	
Three-view geometry		Page 1
Fuselage and wing internal layout		Page 52
PEMFC-related system		12
Multidisciplinary Design Optimization (MDO)	RFP 2.4.6 (grad only)	4
MDO problem		1
Optimum design variables and objective function		4, Table 4.2
Sensitivity analysis		4.2

Vehicle Overview

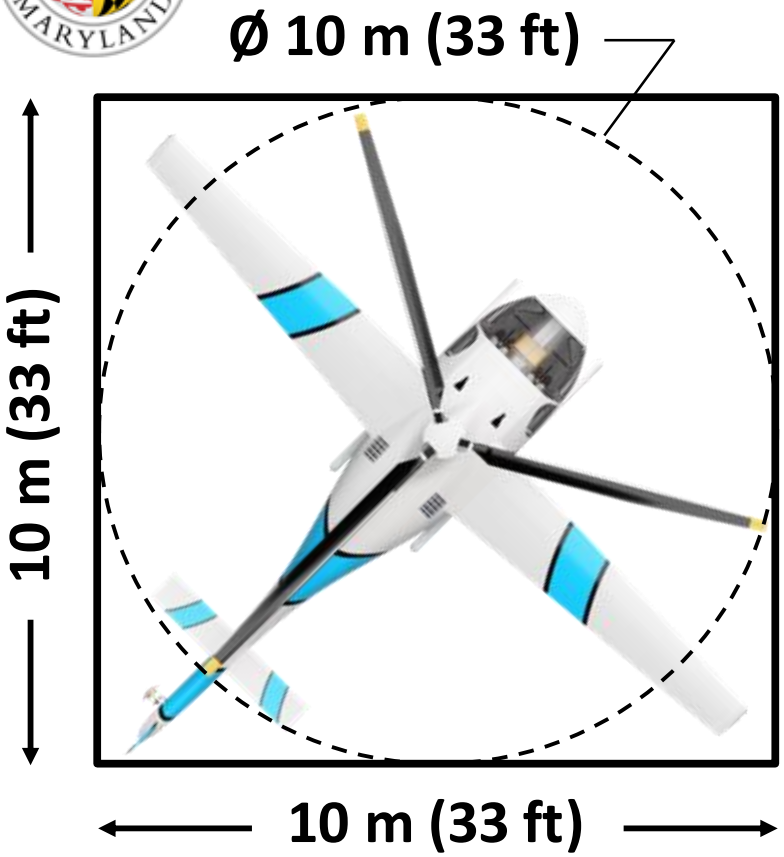

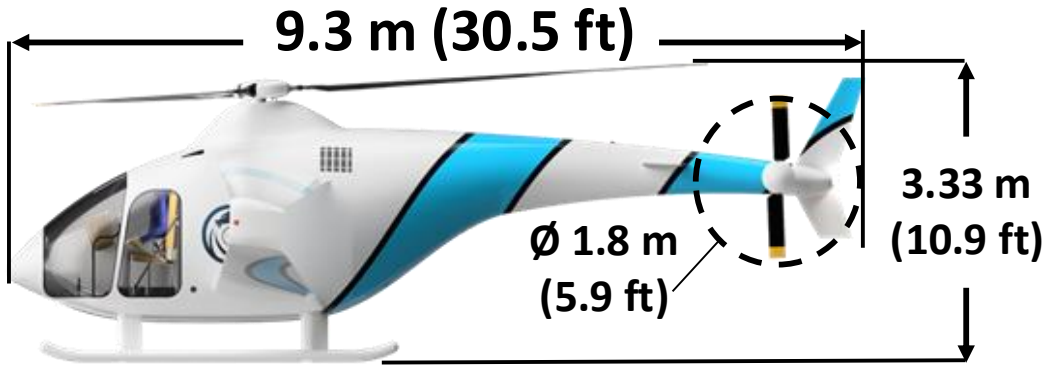

Characteristics	Value
GTOW	1648 kg (3633 lb)
Installed Power	277 kW (371 hp)
Hydrogen Mass	24.8 kg (55 lb)
Loiter Endurance	4.5 hours @ 57 knots
Payload	185 kg (408 lb)

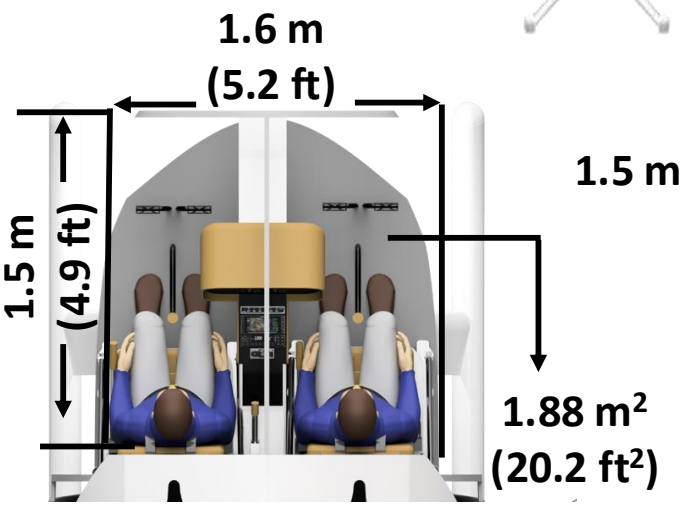

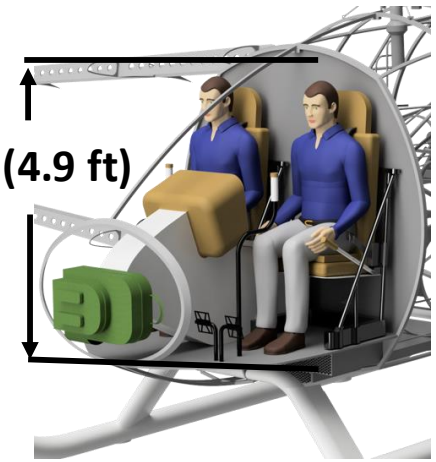

1 Introduction

The aviation sector is approaching an inflection point where the reduction of greenhouse-gas emissions is no longer a long-term aspiration but an immediate global imperative. Governments and industry alike have pledged net-zero CO_2 for air transport by 2050 [1,2], and life-cycle analyses show conventional turbine technology with Sustainable Aviation Fuel (SAF) alone cannot close that gap. Even though aviation accounts for only 2.5% of emissions, as other sectors decarbonize that number can rise to 22% [3, 4]. Electric powertrains eliminate emissions, but battery-only solutions remain constrained to only very short-range missions. Hydrogen (H_2), with its high specific energy and compatibility with renewable production pathways, is emerging as a viable fuel for truly zero-carbon flight, especially when coupled to high-efficiency fuel cells that convert chemical energy directly to electricity. H_2 is increasingly recognized as vital for U.S. energy independence and resilience as well, with the recent bipartisan FAA Reauthorization Act that supports the development of H_2 aviation [5].

Figure 1.1: *Wyvern* in flight over Wright brothers' memorial in Kitty Hawk

Credible efforts toward hydrogen-powered aircraft have emerged from both industry and academia [6–9]. In rotorcraft, where the goal extends beyond clean flight to advanced vertical air mobility, conceptual studies have identified hydrogen as a viable alternative to batteries for enabling practical eVTOL operations [10,11]. Airbus has signaled its commitment to clean-flight through initiatives such as ZEROe hydrogen demonstrators. With the growth of fuel cell technology, small-scale prototypes have demonstrated the feasibility of hydrogen-powered vertical flight [12]. Full-scale hydrogen-electric flight demonstrator programs are also advancing rapidly [13–18]. Notable efforts include Joby's full-scale unmanned flight [19] and Unither's full-scale manned flight [20]. The 42nd VFS Student Design Competition challenges academia to push these concepts beyond demonstrators into certifiable, commercially viable, and mission-ready aircraft.

In response to the 42nd Annual VFS Student Design Competition, the Graduate Student Design Team from the University of Maryland introduces *Wyvern*, a novel hydrogen-powered electric compound rotorcraft engineered for maximum loiter and operational safety. Named after a mythical dragon that defies convention by not breathing fire, *Wyvern* only breathes water vapor by forgoing hydrocarbon combustion in favor of the quiet and clean power of hydrogen. This design reflects not only an aeronautical solution to an engineering challenge but a greater aspiration to reshaping how practical and clean vertical flight can be achieved.

Wyvern is a compound rotorcraft that adopts a 3-bladed slowed rotor configuration enhanced by box-wing lift-compounding, inspired by the Airbus Rapid and Cost-Effective Rotorcraft (RACER), for maximum endurance. It is powered by a Proton Exchange Membrane Fuel Cell (PEMFC) system operating on compressed gaseous hydrogen, hybridized with a high-voltage buffer battery for peak power demands and enhanced autorotation safety. This propulsion architecture enables quiet, efficient, and low-emission flight over sensitive ecological areas like the Alligator River National Wildlife Refuge, fulfilling the mission scenario outlined in the RFP.

The architecture is governed by five key drivers: maximizing aerodynamic efficiency, minimizing structural and systems weight, embedding fail-safe redundancy, ensuring high technological maturity, and assuring a path to near-term certification. *Wyvern* adopts a 10 m (32.8 ft)-diameter single main rotor mated to a box-wing lift-compounding system. The high-aspect-ratio upper and lower wings, joined by load-bearing gusset plates, offload the rotor by up to 60% in cruise, thereby increasing the aircraft lift-to-drag ratio above 9.5. This offloading is enabled by the electric drive, which can slow the rotor to 30% of hover RPM. A streamlined Carbon Fiber Reinforced Polymer (CFRP) fuselage, faired rotor hubs, and an aerodynamically clean skid landing gear yield an airframe drag area near 0.58 m^2 (6.24 ft^2), while tailored blade airfoils, aspect ratio, taper, and twist secure a hover Figure of Merit exceeding 0.785, through multi-objective rotor optimization.

Propulsion is delivered through a mechanically simple, all-electric drivetrain. A Type-IV composite tank of 700 bar (10.1 ksi) feeds a 210 kW (282 hp) PEMFC stack through a 795 V high-voltage DC bus. A 6.7 kWh (9.0 hp· hr) Lithium-ion Silicon anode battery, rated at 10C, covers power peaks along with transients during take-off, hover, vertical climb, and minimizes stack weight. Stack temperature is capped at 90°C (194°F) by a highly weight and power-efficient water-cooling system that circulates through two 150 kW (201 hp) heat exchangers and a variable-speed axial fan delivering 9300 CFM (263 m^3/min) of air in hover. High-efficiency SiC DC-DC converters and two direct-drive 180 kW (241 hp) high power-density Permanent-Magnet Synchronous Motors (PMSM) complete a tank-to-shaft conversion chain operating at better than 30% overall efficiency. Vibration isolation mounts, a low-vibration hub, and wing-bourne loiter reduce passenger fatigue and protect sensitive electronic components during long-endurance flights.

Weight is critical in any rotorcraft. Topology-optimized composite frames, lightweight rotor hub, ultra-lightweight M50 steel bevel gears, supercritical shaft, wings with hinged connections, and simplex flight controls compress the structural-weight fraction to 0.47 at a 1648 kg (3633 lb) Maximum Take-Off Weight. The airframe houses crash-worthy hydrogen tanks behind fire barriers secured using energy-absorbing cradle mounts. Safety protocols include fast-acting pressure relief devices and crash-resistant valve placement. The integrated health-monitoring suite includes stack temperature, cell voltage deviation detection, hydrogen leakage sensors, and predictive diagnostics for both electrical and mechanical subsystems. Additionally, shock-resistant occupants' seats, Nomex honeycomb structures for the tank and the cockpit crash survivability, a four-axis stability-augmentation system with hydraulic actuation, redundant cooling loops for safety-critical components, and a simple floiler deploy mechanism for autorotation allow continued operation after any single-point failure. All major hardware, including Type-IV tanks, PEMFC stacks, and high power electronics operate at TRL ≥ 6, aligning *Wyvern* with the EASA CS-27 certification basis.

Mission performance is calibrated to the RFP's wildlife survey scenario. Launching from the Wright Brothers National Memorial, *Wyvern* executes a vertical departure, transits 30 km to the Alligator River National Wildlife Refuge, and provides an unprecedented four and a half hours loiter in a 2 km × 2 km (1.2 mi × 1.2 mi) area at 30 m (98 ft) above MSL before returning, all while carrying 185 kg (408 lbf) full payload under VFR flight conditions. The configuration delivers more than five hours total flight time with 26 kg (57 lbf) of onboard gaseous H_2, without CO_2, NO_x or particulate emissions of any kind and with a low noise signature. By fusing proven H_2 technologies with an aerodynamically refined, weight-optimized slowed rotor compound configuration, *Wyvern* offers a certifiable, zero-emission VTOL platform that achieves endurance, range, and safety on par with, or exceeding, legacy turbine designs, with silent, flame-free propulsion befitting the mythical dragon whose name it bears.

2 Configuration Selection

The configuration was selected through a rigorous top-down process, beginning with the identification of mission-critical requirements from the RFP and translating them into quantifiable design drivers. Par-

ticular emphasis was placed on minimizing empty weight, ensuring compact footprint compatibility, and achieving efficient cruise and loiter performance for the long-endurance pioneering mission profile. To systematically evaluate competing configurations, an Analytical Hierarchy Process (AHP) was employed to score and rank design drivers derived from the RFP, as detailed in Section 2.1.1. Each team member completed the AHP matrix individually, and the averaged weights with low standard deviation were used to construct a normalized priority vector. A Pugh matrix was then developed using these weights to evaluate and rank six candidate configurations. Each configuration was rated against the design drivers, and total scores were computed as explained in Section 2.3 and shown in Table 2.3. The top four performing concepts were downselected for further detailed analysis.

2.1 Voice of the Customer

2.1.1 Design Drivers

Careful analysis of the RFP determined seven key design drivers. These drivers are listed below:

1. **Cruise L/D:** The vehicle should have the lowest minimum power in loiter for a given weight and cruise velocity. This calls for maximizing the aircraft Lift-to-Drag ratio (L/D) at loiter speed.
2. **Empty Weight Fraction:** The ratio of the empty weight must be minimized to carry H_2 to maximize the loiter.
3. **Safety:** The H_2 storage and supply system is designed with multiple failsafe measures to explosion and fire. The redundancy in the propulsion system ensures a soft landing is possible in an emergency. The robustness of the onboard systems to failure goes beyond routine rotorcraft and propulsion system crashworthiness. Autorotation capability was given special attention.
4. **System Complexity:** Minimizing system complexity reduces potential failure points and ensures reliable performance and low pilot workload.
5. **Technology Readiness Level (TRL):** The RFP prioritizes high-TRL components, such as mature PEMFC systems, drive train, and a certifiable airframe structure. This minimizes development risk and supports the timely prototyping and testing of a credible, near-term demonstration of a hydrogen-powered VTOL platform.
6. **Passenger Experience:** The mission necessitates a smooth, low-vibration wildlife watching experience for passengers with minimal acoustic disturbance to sensitive natural environments.
7. **Lifecycle Costs:** Designs with lower lifecycle costs - through modularity, maintainability, and reduced part count - enhance operational feasibility beyond demonstration missions, supporting widespread humanitarian, logistics, and utility applications in diverse terrains.

2.1.2 Ranking of the Design Drivers

The Analytical Hierarchy Process (AHP) was used for *Wyvern* to systematically rank the design drivers by translating the voice of the customer, derived from the RFP, into quantifiable design drivers. Each driver was pairwise compared against all others using Saaty's 1/9–9 scale, where values above 1.0 indicated greater importance of the row driver over the column driver, and values below 1.0 indicated the opposite. Team members individually constructed AHP matrices, and the averaged

Table 2.1: Normalized priority vector

Design Driver	Weight
Cruise L/D	31.6%
Empty Weight Fraction	25.8%
Safety	14.1%
System Complexity	8.7%
Passenger Experience	7.7%
TRL	6.4%
Cost	5.7%
Total	100%

matrix was reviewed to ensure a low standard deviation and acceptable Saaty consistency index, reducing personal biases and interpretations on the voice of the customer. The final matrix, Table 2.2, was normalized column-wise, and the row averages produced a priority vector indicating the relative weights of each driver, as shown in Table 2.1. These weights served as scaling factors in the configuration selection Pugh matrix described in the next section.

Table 2.2: Analytical Hierarchy Process (AHP) matrix

Design Drivers	Cruise L/D	Safety	TRL	Passenger Experience	Cost	System Complexity	Empty Weight Fraction
Cruise L/D	1.00	2.67	3.53	3.82	6.22	3.58	1.49
Safety	0.37	1.00	2.21	1.47	2.63	2.46	0.52
TRL	0.28	0.45	1.00	0.58	1.09	0.67	0.27
Passenger Experience	0.26	0.68	1.74	1.00	1.02	0.60	0.26
Cost	0.16	0.38	0.92	0.98	1.00	0.64	0.22
System Complexity	0.28	0.41	1.50	1.66	1.55	1.00	0.28
Empty Weight Fraction	0.67	1.92	3.70	3.78	4.63	3.61	1.00

The AHP conducted reflects a mission-driven prioritization of design drivers aligned with the RFP's requirements for a H_2 eVTOL. The normalized priority vector places **Cruise L/D** (31.6%) and **Empty Weight Fraction** (25.8%) as the top two drivers. Safety (14.1%) received significant weight, underscoring the importance of operational reliability and certification viability in early design. System Complexity (8.7%), Passenger Experience (7.7%), and TRL (6.4%) followed. Cost was given the lowest weight (5.7%), typical of a novel conceptual design where performance takes precedence over economics. The pairwise comparison matrix shows consistency and consensus, with Cruise L/D and Empty Weight Fraction scoring dominantly across comparisons.

2.2 Candidate Vehicle Configurations

A study of 12 candidate configurations was conducted using a Pugh decision matrix to identify the most suitable architecture for the mission profile outlined in the RFP. Each configuration was evaluated and ranked based on the weighted design drivers from the AHP. The conventional single main rotor with tail rotor (SMR) served as the baseline for comparison due to its proven reliability and maturity. A brief description of each configuration, along with its key advantages and disadvantages, is presented below. The configurations are categorized into three groups based on their ability to meet the RFP requirements and the level of technological risk involved: (1) Incapable of meeting the RFP; (2) Moderately Capable, but with significant complexity and reliance on unproven technologies; and (3) Capable, with integration of innovative technologies with manageable challenges.

2.2.1 Not Capable of Meeting the RFP

The configurations in this category are the following (shown in Figure 2.1):

- **Coaxial:** The coaxial configuration features two vertically stacked, counter-rotating rotors that cancel torque without a tail rotor, offering a compact footprint. However, it introduces significant mechanical complexity, higher cost, and increased empty weight due to a heavier mast and hub

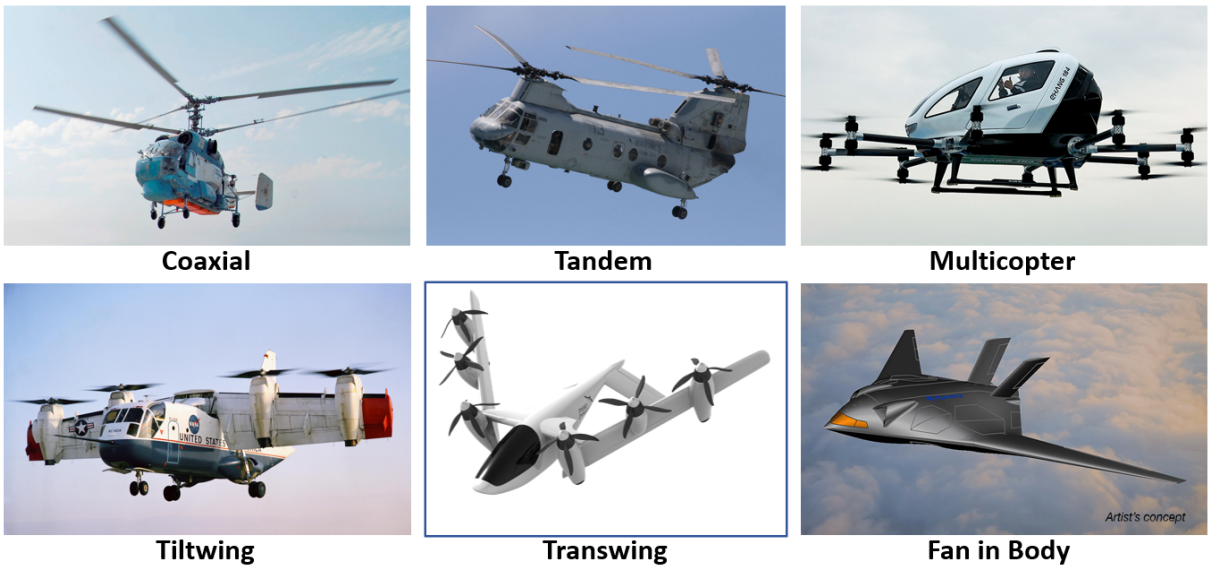

Figure 2.1: Configurations incapable of meeting the RFP

structure. Yaw control authority is inherently lower. The taller mast also increases hub drag, reducing cruise and loiter efficiency.

- **Tandem:** Tandem rotorcraft, with two longitudinally spaced counter-rotating rotors, offer natural anti-torque and excellent longitudinal CG tolerance. Overlapping rotors, which are needed due to footprint limits, increase drag and reduce cruise efficiency. A second rotor system and interconnecting structure raise structural mass, while rotor wake interactions lead to higher vibrations. Tank integration would be easier, but fuel weight fraction is higher, which is a critical drawback for H_2.
- **Multicopter:** Multicopters use multiple fixed-orientation rotors controlled via rotor speed variation, offering simple control, gust tolerance, and redundancy. Their swashplateless design reduces mechanical complexity. However, the large number of rotors introduces significant failure modes, and hub drag, degrading cruise performance, critical during loiter. Thus, it conflicts with weight and endurance requirements. Autorotation is not feasible either.
- **Tiltwing:** Tiltwing designs rotate the entire wing and mounted rotors for vertical and forward flight, potentially improving hover efficiency by avoiding wing-rotor interference. However, hover is not for long and does not warrant the mechanical complexity and weight. Gust tolerance is poor, as the wing acts like a sail during hover. Transition flight introduces aerodynamic instabilities, such as buffeting.
- **Transwing:** Transwing aircraft morph between a high-aspect-ratio monoplane (cruise) and a quad-like layout (hover) using folding wings. The complex transformation mechanisms have all the drawbacks of multicopter and tiltwing.
- **Fan in Wing/Body + Pusher propeller:** This design uses ducted fans embedded in the airframe for VTOL, with a separate pusher for forward thrust. Covered fan inlets improve cruise aerodynamics. While sleek and integrated, the configuration faces major weight packaging and control challenges. Swashplate integration is impractical, and control authority during hover is limited.

2.2.2 Moderately Capable of Meeting the RFP

The configurations in this category are the following (shown in Figure 2.2):

- **Lift + Cruise Hybrid with Fixed Wing (tiltable or fixed propellers):** The lift + cruise hybrid eVTOL configuration uses dedicated vertical lift rotors and separate cruise propellers, with

Figure 2.2: Configurations moderately capable of meeting the RFP

a fixed wing providing lift during cruise. Each propulsion system is optimized for its flight regime to maximize hover efficiency and cruise performance. During transition, lift rotors are stopped or stowed to reduce drag, while cruise propellers and the wing take over. While good on paper, lift props are prone to failure, and two-bladed props on pylons are prone to dangerous instability and vibrations due to variable inertia.

- **Conventional Tiltrotor:** Tiltrotors rotate wingtip-mounted proprotors between vertical and horizontal flight modes, enabling VTOL and efficient high-speed cruise. Fixed wings improve lift-to-drag ratio and range. However, tilting mechanisms add structural weight and complexity. Power loading is reduced by wing download and smaller rotor diameters.
- **Single Main Rotor with Lift and Thrust Compound:** The Single Main Rotor (SMR) with lift and thrust compounding, as seen in configurations like the Airbus RACER and X^3, augments a conventional main rotor with wings and a pusher propeller for cruise. The rotor handles hover, while wings and the propeller take over in forward flight, allowing significant rotor speed reduction and improved cruise efficiency. While offering a good L/D and lower noise, the configuration adds weight and complexity from a rear-mounted transmission. Its cruise advantages are more beneficial at higher speeds than required by the RFP.

2.2.3 Highly Capable of Meeting the RFP

The configurations in this category are the following (shown in Figure 2.3):

Figure 2.3: Configurations highly capable of meeting the RFP

- **Single Main Rotor and Tail Rotor:** The SMR configuration is the most established and widely adopted rotorcraft architecture, serving as the baseline for all configuration comparisons due to its proven performance, simplicity, and reliability. It employs a single large-diameter main rotor for lift, propulsion, and control in pitch and roll, while a conventional tail rotor provides anti-torque and yaw control. Its mechanical layout is well understood, extensively validated through decades of military and civilian use, and supported by a mature certification pathway. While its forward flight performance is limited by advancing blade compressibility, high hub drag, and retreating blade stall at very high speeds, these limitations are outside the required flight envelope of the RFP. Instead,

its low empty weight, favorable hover, and minimal complexity make it highly suitable. Its only drawback is its poor L/D in cruise (around $4-5$).

- **Single Main Rotor with Lift Compound:** The lift-compounded SMR configuration integrates a fixed wing to share the lifting burden with the rotor, significantly improving cruise efficiency while maintaining the simplicity and reliability of a conventional helicopter architecture. By offloading the main rotor during forward flight, the wing enables a higher L/D and allows for reduced rotor tip speed, leading to lower vibration and noise. Mach-scaled wind tunnel and hover tests at the University of Maryland have shown the feasibility of high L/D (around $6-7$) with only 3–6% of hover download penalty [21, 22]. Although the wing adds structural weight, it is manageable within the RFP's footprint and performance constraints.
- **Multicopter Tiltrotor:** The multicopter tiltrotor configuration, exemplified by the Joby S4, offers the hover agility of a multicopter with the cruise efficiency of a fixed-wing aircraft. Multiple distributed electric rotors tilt from vertical to horizontal, enabling full rotor utilization in both hover and cruise, unlike lift + cruise hybrids, where unused rotors generate drag. Compared to conventional 2-rotor tiltrotors, this architecture reduces individual rotor loading and provides redundancy while electric transmission avoids mechanical cross-shafting. Tilt mechanisms are mature. The configuration demonstrated long-endurance flight using liquid H_2, albeit unmanned. While this configuration is capable of performance, multiple rotors introduce multiple fault scenarios, which is a challenge for certification from unmanned to manned.

2.3 Ranking of the Configurations

The team ranked the moderately capable and the highly capable vehicle configurations using a Pugh decision matrix (Table 2.3) to select the best vehicle configuration. The SMR configuration was used as the baseline, so all its values were set to zero. A grading scale of -5 (poor) to +5 (excellent) with increments of 1 was used to rate each configuration relative to every design driver. The final score was determined by weighting the Pugh matrix result with the normalized priority vector from the AHP to account for the voice of the customer properly.

Table 2.3: Pugh matrix for vehicle configuration selection

Design Drivers	Weight	SMR	SMR + Lift compound	SMR + Lift + Thrust compound	Multicopter tiltrotor	Conventional tiltrotor	Lift + Cruise hybrid
Cruise L/D	0.316	0	3	3.5	4	2	2.5
Empty weight Fraction	0.258	0	-2	-3	-3	-3	-3
Safety	0.141	0	1	2	-1	-2	-1
System complexity	0.087	0	-1	-3	-4	-3	-2
TRL	0.077	0	-1	-1	-1	0	-2
Passenger Experience	0.064	0	2	2	3	3	2
Cost	0.057	0	-2	-3	-3	-3	-4
Score	1	0	0.423	0.233	-0.055	-0.664	-0.553

For *Wyvern*, the Pugh matrix results identified the top four configurations as the lift-compounded SMR,

the lift+thrust compounded SMR, SMR, and the multicopter tiltrotor. These four were downselected for detailed analysis, described in Section 3. While all four offered strong performance across mission metrics, the lift-compounded SMR emerged as the optimal choice due to its superior balance of cruise efficiency, hover performance, low empty weight, system simplicity, and technological maturity.

3 Configuration Trade Studies

As concluded in the Section 2, SMR, SMR+L, SMR+L+T, and the Multicopter Tiltrotor were the top four configurations. In this section, these are sized and analyzed through detailed trade studies to make a final selection. The final selection is then subjected to Multidisciplinary Design Optimization (MDO).

3.1 Preliminary Vehicle Sizing

The initial sizing of all four vehicle configurations was carried out using in-house sizing tools developed by the team. For aircraft components, the U.S. Army Aeroflightdynamics Directorate (AFDD) weight models [23] were used. A series of trade studies was conducted to examine the impact of rotor, wing, and propeller design parameters on overall aircraft weight and performance.

3.1.1 Mission Profile

The mission is shown in Figure 3.1. There are 16 segments in the RFP pioneering mission which takes off from Kitty Hawk, NC, USA, loiters over the Alligator River, and returns to the take-off point.

1. Normal vertical takeoff to HIGE, at MSL ISA
2. HIGE at MSL [for 15s]
3. Vertical Climb to 60 m (197 ft) above MSL [Vertical ROC = 0.76 m/s (150 ft/min) OGE]
4. HOGE at 60 m (197 ft) above MSL [for 10s]
5. Steady climb to 300 m (984 ft) above MSL [Flight path angle = 9° with respect to ground, V_{climb} horizontal speed]
6. Cruise at 300 m (984 ft) above MSL [at V_{br}]
7. Steep descent to 30 m (98 ft) above MSL [-7.6 m/s descent rate at V_{climb} horizontal speed, autorotation authorized]
8. HOGE at 30 m (98 ft) above MSL [30s sustained hover]
9. **Loitering at 30 m (100 ft) above MSL within a 2×2 km (1.2×1.2 mi) square at V_{be}, horizontal speed only**
10. Steady climb to 300 m (984 ft) above MSL [Start of return segment, flight path angle = 9° with respect to ground, V_{climb} forward speed]
11. Cruise at 300 m (984 ft) above MSL [at V_{br}]
12. Steady descent to 60 m (197 ft) above MSL [5° descent angle at $V_{descent}$ vertical speed]
13. HOGE at 60 m (197 ft) above MSL [for 10s]
14. Vertical descent to HIGE MSL [Rate of descent = 0.50 m/s (98 ft/min) OGE]
15. HIGE at MSL [for 15s]
16. Normal vertical landing from HIGE

The constraints set by the RFP for this manned eVTOL mission are as follows:

1. Full-electric aircraft, powered by PEM fuel cells, with pressurized gaseous H_2 storage.
2. Carry 1 pilot and 1 passenger with luggage, equivalent to a total payload of 185 kg (408 lbf).
3. Complete aircraft with full rotor disk(s) must fit within a rectangular prism of dimensions $10 \times 10 \times 4\ m^3$ ($33 \times 33 \times 13\ \text{ft}^3$).
4. A minimum interior usable cabin floor dimension of 1.25 m (4.1 ft) (width) $\times$1.5 m (5 ft) (length).
5. The weight of the integrated battery (cells and casing) is limited to 30 kg (66 lbf).

This mission profile is simulated for all four vehicle configurations to find which maximizes the loiter time in segment 9 of the mission.

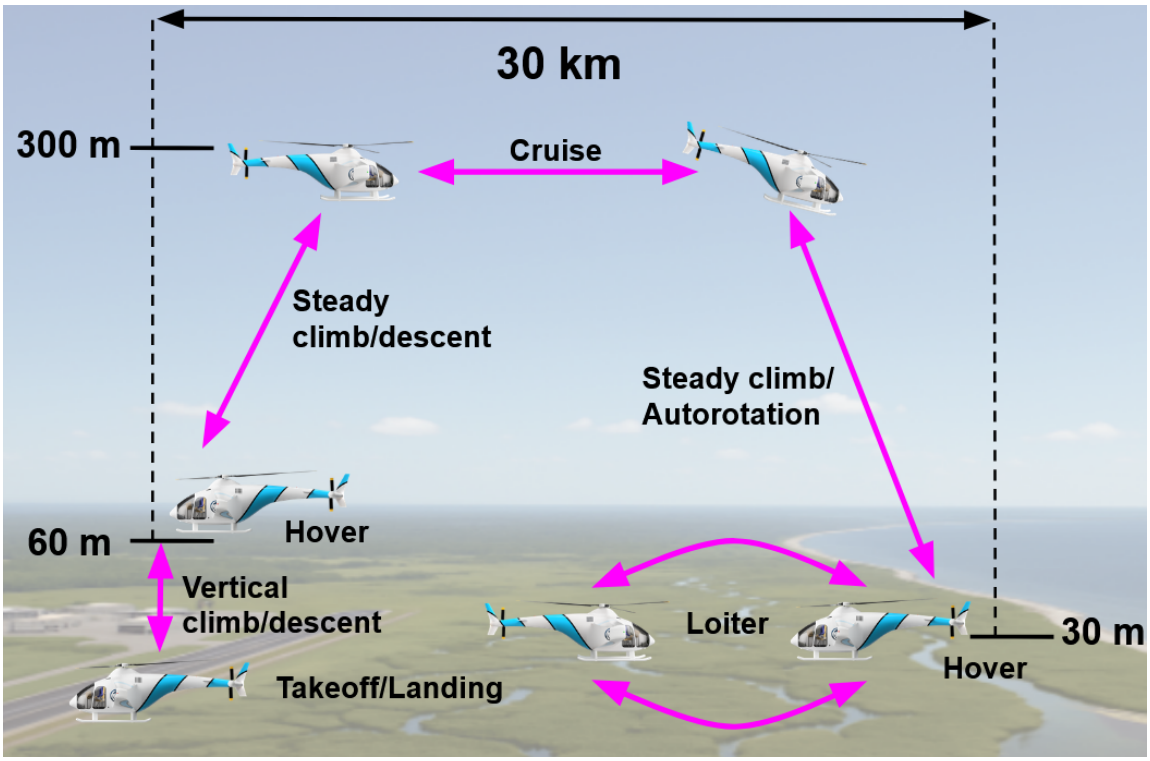

Figure 3.1: Mission profile

3.1.2 Sizing Methodology

Each of the configurations was sized using an in-house modified blade element code. The configuration sizing algorithm is depicted in Figure 3.2. For a given T_9, the sizing algorithm is iterated to converge to a Gross Takeoff Weight (GTOW). The rotor and wing aerodynamic properties, airframe drag, and fixed propeller efficiency were used to achieve the propulsive trim of the vehicle. To maximize the loiter time, the main rotor RPM was varied, taking advantage of the electric motor. The SMR and SMR+L used rotor speed, aircraft pitch, and blade loading as parameters to trim the aircraft. In the SMR+L+T, an additional parameter was the propeller thrust. Airframe drag used the Harris drag equation $D = qF$ [24], where q is the dynamic pressure and $F = \kappa(W/1000)^{2/3}$, where W is in lb. The Harris drag factor, κ, is typically 2.95 for SMR and SMR+L, 3.15 for SMR+L+T, and 3.2 for multicopter tiltrotor.

The hover and vertical climb/descent download in SMR was considered to be 6%, and decreases linearly to 0 from hover to 20 m/s (66 ft/s) forward speed. Accordingly, for SMR+L, the download is calculated from wake contraction [25] using the wetted wing area by the rotor downwash, and varied from 7% to 15% with wing area. For SMR+L+T, it was considered as 14%. The combined transmission and motor efficiency at all the mission segments was considered to be 91%.

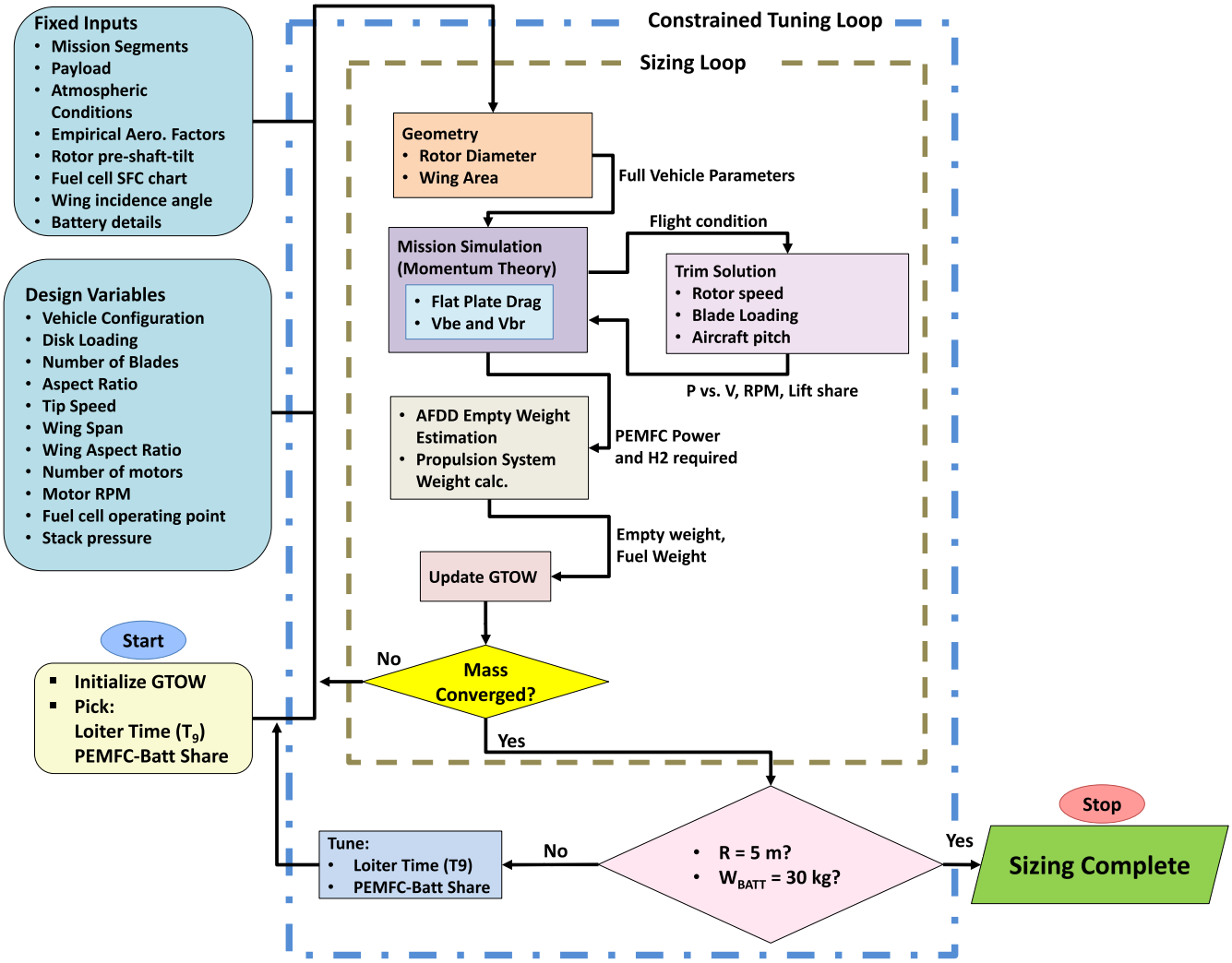

Figure 3.2: Flowchart of vehicle sizing procedure

Weights were calculated using the U.S. Army AeroFlight Dynamics Directorate (AFDD00) models [23]. Technology factors were used in NASA Design and Analysis of Rotorcraft (NDARC) models for rotorcraft components using [26] to account for advancements in materials, manufacturing, and design. The RFP allowed a peak power augmentation by using a hybrid battery. Realistic pack-level battery energy density of 150 Wh/kg (91 hp·hr/lbf) (available and installed) and maximum continuous discharge rate of 10 C were considered to compute the battery weight. This peak power share was tuned appropriately for each configuration. The weight of the PEMFC stack and the balance of plant components were computed from [27, 28], and informed by measurements in-house. The number of cells of the stack was kept constant at 589 (from design Stack voltage at Hover = 330 V and design Cell voltage at Hover = 0.56 V). The stack operating pressure, temperature, and altitude were set to 1 atm, 80 °C (176 °F), and 30 m (100 ft) from MSL, respectively. The output weight of the Stack + BOP system was calibrated based on the commercial system-level specific power from Horizon [29]. The specific fuel consumption (SFC) for each mission segment was computed as a function of the operating/design stack power. The Hydrogen fuel and the fuel tank weight were accordingly computed using 5.7% H_2 storage weight fraction.

3.2 Sizing Drivers

The McHugh stall boundary [30] limits the hover blade loading coefficient to $C_T/\sigma = 0.16$. However, to account for ample margin during forward-flight transition as well as sufficient control authority under gusts, the target blade loading in hover was limited to 0.12. In edgewise flight, the blade loading stall limit decreases significantly at higher advance ratios following [30]. The minimum and maximum advance ratios to be set at 0.2 and 0.4 to avoid the free-wake dominated high vibration regime during the transition and the high-μ related aeroelastic problems [31]. Disk loading was capped at 287 N/m^2 (6 lbf/ft^2) to minimize hover downwash. In addition, a higher disk loading contributes to an increase in noise generated by the aircraft, which is antithetical to the benefits of eVTOL. The minimum and maximum hover tip speeds were set based on the autorotation performance, and the acoustics limit based on the maximum tip Mach number to 0.65, respectively.

3.3 Configuration 1: Single Main Rotor

The sizing for SMR determined the rotor-specific parameters, which were later passed onto the compound configurations. Because the RFP restricted the main rotor diameter to 10 m (33 ft) and the battery weight to 30 kg (66 lbf), a trade study was performed to determine these two parameters first.

3.3.1 Main Rotor Radius and Battery Weight

Figure 3.3 shows the loiter time variation with increasing main rotor radius for different battery weights. The rotor input parameters were set to blade number = 3, aspect ratio = 20, (solidity = 0.0477), disk loading = 201 N/m^2 (4.2 lb/ft^2), tip speed = 185 m/s (607 ft/s). It is observed that for any set of rotor and powerplant parameters, the loiter time increased monotonically with larger radius and a heavier battery. Hence, in all of the cases, they were set to 5 m (16.4 ft) and 30 kg, respectively.

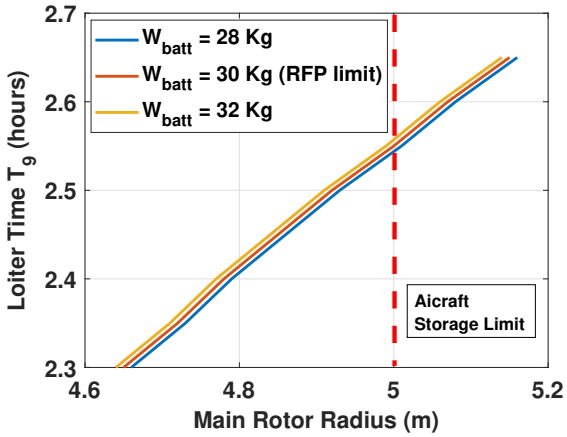

Figure 3.3: Trade study for main rotor radius and battery weight

3.3.2 Number of Blades

The number of main rotor blades N_b was varied from 2 to 5, while keeping the solidity and the tip speed constant. Figures 3.4(a) and 3.4(b) show the effect of the increasing number of blades for two different solidities $\sigma = 0.05$ and $\sigma = 0.06$ at $M_{tip} = 0.54$. These low solidities were appropriate for high loiter time. For a given solidity and disk loading, increasing the number of blades reduces the blade chord by increasing the aspect ratio, keeping the hover power unchanged. The combined effect results in the reduction of the rotor mass with more blades, improving the empty weight fraction, and hence, achieving a longer loiter time. For these solidities, 4 and 5-bladed rotors resulted in blades too slender to be structurally feasible. Thus, $N_b = 3$ was selected. Fewer blade count also decreased vehicle manufacturing and purchasing costs later.

3.3.3 Aspect Ratio and Solidity

With the number of blades selected, a trade study was performed on the blade aspect ratio b_{AR} (effectively changing the blade solidity), at $V_{tip} = 185$ m/s. Figure 3.5 shows the variation of the loiter time with disk loading for $b_{AR} = 12, 16, 20, 24$. Increasing the b_{AR} from 12 to 20 showed improvement in the loiter time

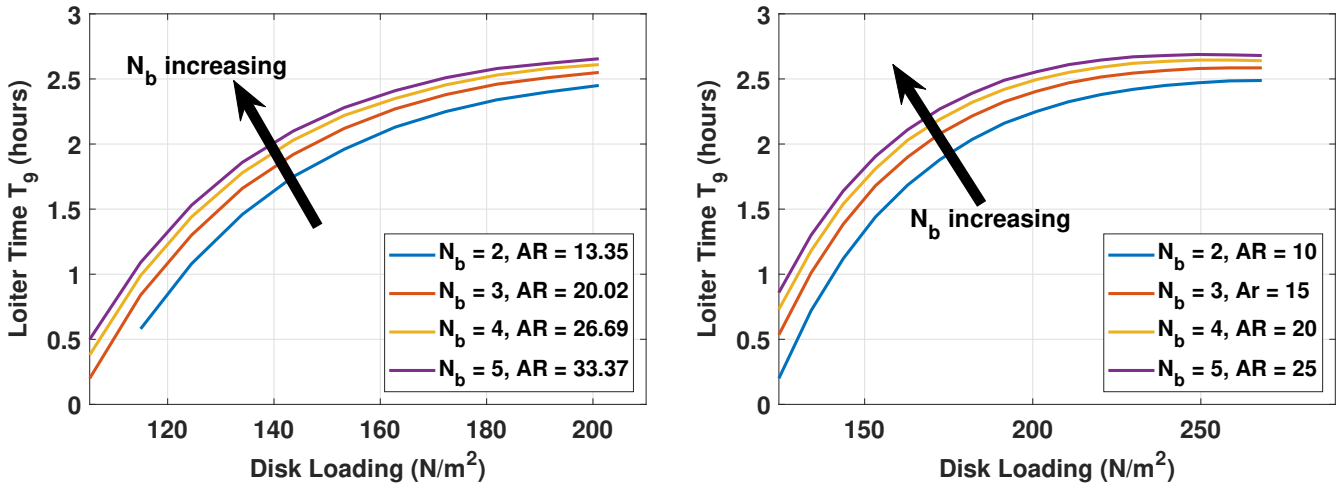

(a) $\sigma = 0.06$ (b) $\sigma = 0.05$

Figure 3.4: Trade study for number of blades

for the same disk loading, as it reduced the profile drag and tip losses from reduced solidity. Each aspect ratio trend line for disk loading variation was limited by the rotor stall condition. Although the $b_{AR} = 24$ blade resulted in the highest loiter, it was too slender and flexible to be feasible. Hence, the aspect ratio of 20 ($\sigma = 0.05$) was selected.

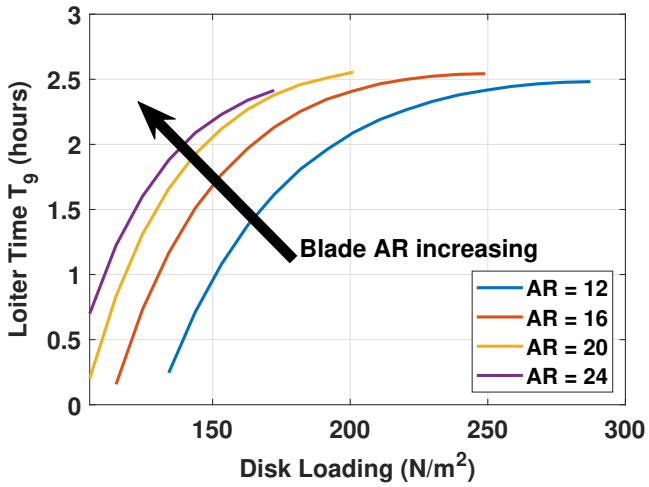

Figure 3.5: Trade study for blade aspect ratio and solidity

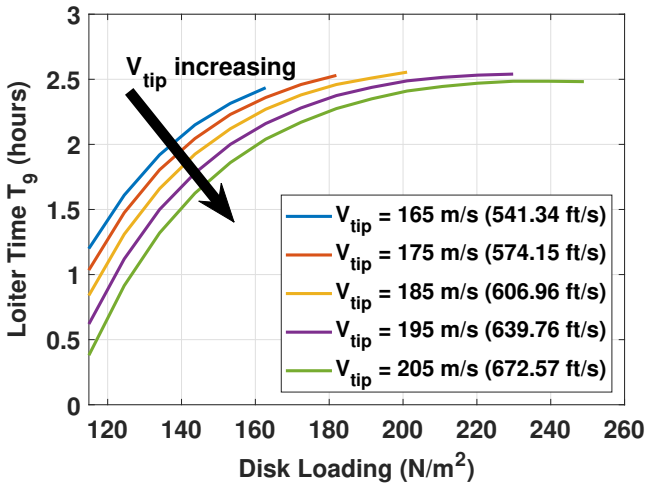

Figure 3.6: Trade study for main rotor tip speed and disk loading

3.3.4 Tip Speed and disk Loading

With the number of blades and blade aspect ratio selected, a trade study was performed with the disk loading for different tip speeds (Figure 3.6). The maximum disk loading for a given tip speed is limited by the blade loading $C_T/\sigma = 0.12$. For a given tip speed, loiter increases with DL up to a limit, when any further increase is detrimental due to the penalty from the stack system weight outweighing the benefit from more fuel. The maximum loiter time was achieved for a disk loading of 201.1 N/m^2 (4.2 lbf/ft^2) and a tip speed of $V_{tip} = 185$ m/s (607 ft/s).

3.4 Configuration 2: Single Main Rotor with Lift Compound

The number of blades, blade aspect ratio, disk loading, and the hover tip speed selected from the SMR trade studies are kept the same for the SMR+L configuration. In this section, the wingspan and the wing aspect ratio are varied to achieve the maximum loiter time. The main rotor radius and battery weight are kept constant at 5 m (16.4 ft) and 30 kg (66 lbf), respectively.

3.4.1 Wingspan and Wing Aspect Ratio

Lift compounding aims to bridge the gap in L/D from an SMR aircraft to a fixed-wing aircraft by offloading the rotor and loading the wing. A trade study on loiter time with wingspan for various wing aspect ratios was performed for a wing incidence angle of 8° and no taper. The pitch of 8° was selected based on the vehicle's nose-down required to trim in cruise. The results are shown in Figure 3.7. Increasing the wing area by increasing the wing span and decreasing the wing aspect ratio increases the wing share; however, reducing the aspect ratio also increases induced drag, and a large wing area increases download. The footprint constraint restricted the AR and the tip chord. From the trade study, a wingspan of 5.5 m (18 ft) and the wing AR of 10 resulted in the maximum loiter time.

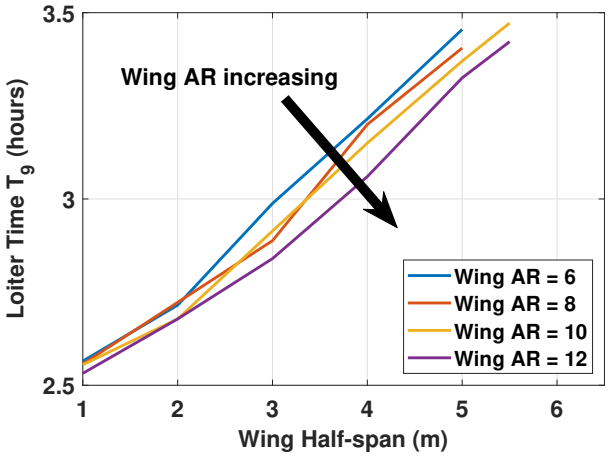

Figure 3.7: Trade study for wing half span and aspect ratio

3.5 Configuration 3: Single Main Rotor with Lift and Thrust Compound

Auxiliary thrusters to provide the propulsive force can offload the rotor in cruise even more and potentially increase the vehicle L/D further. Two different configurations for SMR+L+T were considered for sizing: SMR and Tail rotor with wing and a pusher prop, SMR and wing with two wingtip propellers (no tail rotor). The second configuration was selected, as an antitorque capability is inherent in the design and there is redundancy if one propeller failed. Also, the pusher prop resulted in a tail-heavy design and lower propulsive efficiency. Reduced propulsive efficiency is due to the fuselage impinging the propeller inflow and wing wake ingestion by the propeller [32, 33].

3.6 Configuration 4: Multicopter Tiltrotor

While most existing designs are battery-powered, hydrogen-powered variants are emerging. In cruise, all rotors tilt forward, with the wing carrying full weight.

3.6.1 Number of Rotors

To maximize loiter time within the RFP's dimensional limits, a trade study was conducted on rotor count. A V-tail layout was chosen to allow two additional rotors, resulting in a baseline of four rotors—two on the wing and two on the tail. Only even-numbered rotor configurations were considered for their simplicity and control robustness. Odd-numbered setups were excluded due to their complex dynamics and reduced scalability for larger, hydrogen-powered aircraft [34].

Figure 3.8(a) shows the change of the rotor radius due to the increasing number of rotors. The radius must change due to the limitation of the dimension of the wing. Figure 3.8(b) presents the change in the loitering time by the number of rotors. From 8 rotors onward, the loiter time goes to 0. As the number of rotors increases, the motor and tilt mechanism weights penalty outweighs the benefit from each rotor weight reduction. Also, the radius decreases exponentially, which increases disk loading, increasing hover power significantly, and increasing the stack weight for a fixed battery. This limited the disk loading to 600 N/m^2, allowing loiter capability for only up to 6 rotors.

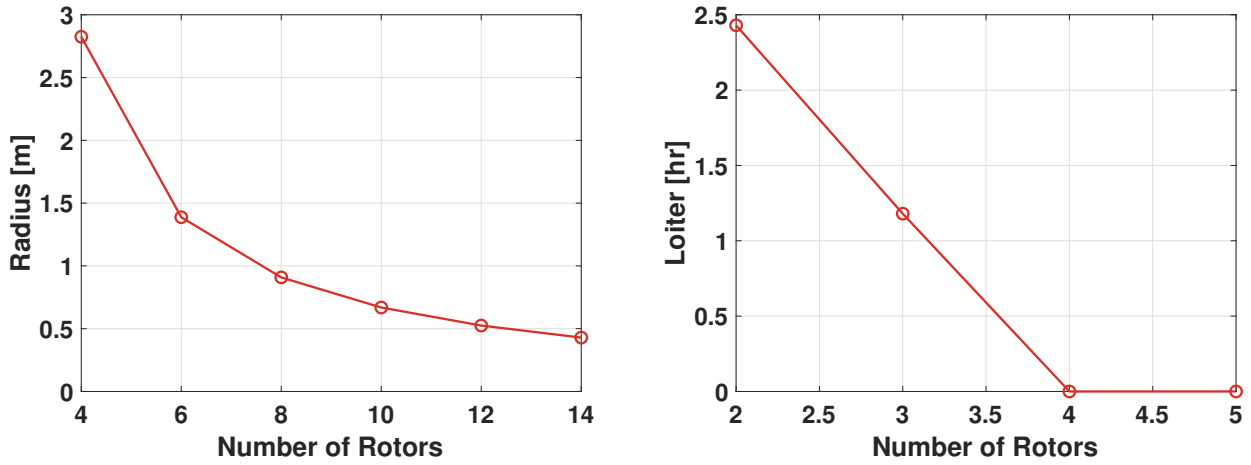

(a) Rotor radius vs. number of rotors (b) Loiter time vs. number of rotors

Figure 3.8: Change in radius and loitering time due to different number of rotors

3.7 Configurations Trade Study Summary

The SMR, SMR + L, SMR + L + T, and multicopter tiltrotor are compared in Table 3.1. The SMR,

Table 3.1: Comparison of vehicle configurations

Parameters	**SMR**	**Lift Compound**	**Lift+Thrust Compound**	**Multicopter Tiltrotor**
Disk Loading [N/m^2, (lb/ft^2)]	201 (4.2)	201	201	520 (11)
Number of Blades	3	3	3	3 per rotor
Blade Aspect Ratio	20	20	20	8
Rotor Solidity	0.0477	0.0477	0.0477	0.050 per rotor
Rotor Tip Speed [m/s, (ft/s)]	185 (607)	185	185	198 (650)
Hover M_{tip}	0.54	0.54	0.54	0.58
Rotor Radius [m, (ft)]	5 (16.4)	5	5	2.83 (9.28) per rotor
Wing Aspect Ratio	-	10	10	10
Loiter Wing Loading [N/m^2, (lb/ft^2)]	-	542 (11)	530 (10)	718 (15)
Wing Share in Loiter	-	54%	58%	100%
Harris Factor	2.95	2.95	3.15	3.2
Hover Download, %GTOW	6%	12%	14%	20%
Structural Weight Fraction	0.421	0.470	0.502	0.660
Empty Weight Fraction	0.866	0.870	0.871	0.892
Loiter Time [hours]	2.56	**3.47**	2.89	2.71
Max. Power Required (Seg. 3) [kW, (hp)]	268 (360)	**286 (383)**	301 (404)	278 (372)

lift compound, lift plus thrust compound, and multicopter tiltrotor are compared in Table 3.1. All configurations met the RFP mission requirements, adhering to the constraints. Specific parameters were set

accordingly for each configuration from the trade studies to maximize the loiter. The maximum loiter time increased with the wing share percentage as the cruise L/D increased, as well as the reduction of the empty weight fraction. The cruise L/D of the SMR+L+T was slightly lower than the SMR+L. The penalty for loiter time was also significant due to its higher hover power, which increased the stack weight penalty. Propellers on a high wing resulted in an even higher empty weight fraction.

Minimizing the hover power is equally important to maximize loiter, as the PEMFC stack and motor-specific power are lower compared to internal combustion engines. The SMR, SMR+L+T, and multicopter tiltrotor configurations were ruled out based on the preliminary vehicle sizing. The SMR + L emerged as the best configuration with 20% more loiter time than the next best. In the following section, an MDO of the SMR + L was performed to refine the vehicle parameters.

4 Multi-Disciplinary Design Optimization (MDO)

Multidisciplinary Design Optimization (MDO) is a formal design methodology that simultaneously considers and optimizes all interacting disciplines—such as aerodynamics, propulsion, energy systems, structures, noise, controls, and mission performance—rather than treating them in isolation. Section 2.4.6 of the RFP requires a constrained MDO of the aircraft to maximize the loiter time of the mission. Figure 4.1 shows the MDO framework used in this study. The sizing flowchart in Figure 3.2 was used for the function evaluation, coupled with a global optimizer (Genetic Algorithms [GA]), and the methodology of GA explained in Section 4.1 was implemented. The function evaluation was subdivided into **4 domain-specific segments**: Rotor, Wing, Drivetrain, and Powerplant (design variables explained in Section 4.2). As already explained in Section 3.3.1, each configuration was tuned to have the main rotor radius of 5 m and the battery weight of 30 kg, adhering to the RFP constraints. In addition to that, the constraints mentioned in the Section 3.1.1 were also instated. Each domain-specific design variable was also constrained based on physical justifications, explained in the sensitivity analyses. The mathematical model of the optimization problem is shown in Equations 1, 2, and 3 and Table 4.1.The results of the Global Optimization of the aircraft, along with its optimal inputs and the output, are presented in Table 4.2.

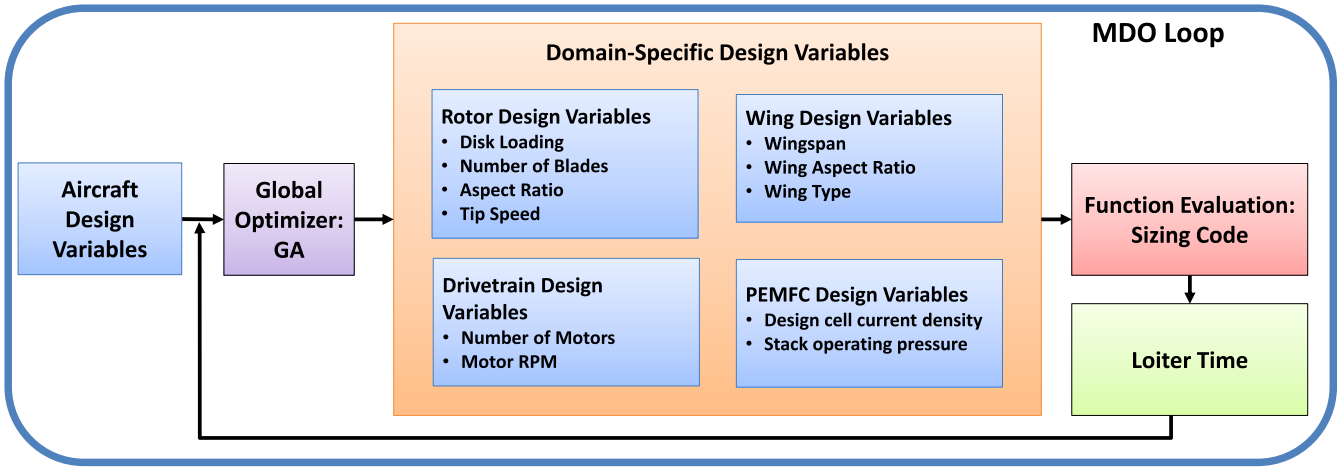

Figure 4.1: Flowchart of multi-disciplinary optimization framework

$$
\begin{aligned}
&\max_{\mathbf{x}\in\mathcal{X}} \; T_9(\mathbf{x}) \\
&\mathbf{x} = \Big[\underbrace{\mathbf{x}_{\text{rotor}}}_{4},\ \underbrace{\mathbf{x}_{\text{wing}}}_{3},\ \underbrace{\mathbf{x}_{\text{drive}}}_{2},\ \underbrace{\mathbf{x}_{\text{PEMFC}}}_{2}\Big]^{\top} \in \mathbb{R}^{11} \\
&\mathbf{x}_{\text{rotor}} = [N_b, b_{\text{AR}}, DL, V_{\text{tip}}]^{\top}, \quad \mathbf{x}_{\text{wing}} = [\,b_W,\ W_{\text{AR}},\ s]^{\top}, \quad s \in \{\text{planar}, \text{box}\}, \\
&\mathbf{x}_{\text{drive}} = [\,N_{\text{motor}}, \text{RPM}_{\text{motor}}]^{\top}, \quad \mathbf{x}_{\text{PEMFC}} = [\,j_{\text{des}}, p_{\text{stack}}]^{\top}
\end{aligned}
\tag{1}
$$

All design constraints are collected in the feasible set:

$$
\chi = \{\mathbf{x} | \text{ bounds in Table 4.1 and fixed limits in Equation 3}\} \tag{2}
$$

$$
\begin{aligned}
&W_{\text{battery}} = 30 \text{ kg (66 lbf)}, \qquad R_{\text{MR}} = 5 \text{ m (16.4 ft)} \\
&\text{Full aircraft within 10 m} \times 10 \text{ m} \times 4 \text{ m box}
\end{aligned}
\tag{3}
$$

Table 4.1: Design variables, bounds, and data-types

Subsystem	Variable	Symbol	Range	Units	Type
Rotor	Number of blades	N_b	2–5	–	integer
	Blade aspect ratio	b_{AR}	14–22	–	continuous
	disk loading	DL	170–220 (3.56–4.97)	N /m^2 (lbf /ft^2)	continuous
	Tip speed	V_{tip}	180–210 (591–689)	m /s (ft/s)	continuous
Wing	Span	b_W	10–12.8 (33–42)	m (ft)	continuous
	Wing aspect ratio	W_{AR}	6–12	–	continuous
	Planform type	s	planar / box	–	categorical
Drivetrain	Number of motors	N_{motor}	1–4	–	integer
	Motor speed	$\text{RPM}_{\text{motor}}$	4 000–20 000	RPM	continuous
PEMFC	Desired current density	j_{des}	0–1.6	A /cm^2	continuous
	Stack pressure	p_{stack}	1–1.25	atm	continuous

4.1 Genetic Algorithms

Genetic Algorithms take inspiration from natural selection. It starts by randomly generating a population of potential solutions (design variables). A fitness function is defined to evaluate the solutions. Based on the fitness scores of the solutions, individual samples are selected to form a mating pool, often termed as selection. Superior solutions have a higher chance of getting selected, which then undergo crossover and mutation to create a new pool of solutions. After each cycle, the best solution is retained. This is termed elitism. The process of selection, crossover, and mutation is repeated until convergence. For this study, convergence is defined based on the difference in the cost function between two consecutive generations. The randomness associated with crossover and mutation ensures that the solution does not get stuck in a local optimum.

4.2 Sensitivity Analysis

Sensitivity analysis is crucial to identify how variations in design variables impact the loiter time. It helps prioritize design parameters for effective optimization. The sampling-based global sensitivity method has been utilized here for all the input variables. The sensitivity analysis focused on the input parameter: number of rotor blades (N_b), blade aspect ratio (b_{AR})(effectively rotor solidity (σ)), hover disk loading

Table 4.2: Optimization results for *Wyvern* loiter-time MDO

Discipline	Variable	Symbol	Optimal value
Rotor	Blade count	N_b	3
	Blade aspect ratio	b_{AR}	20
	Disk loading	DL	205.89 N/m^2 (4.3 lbf/ft^2)
	Tip speed	V_{tip}	182 m/s (597 ft/s)
Wing	Span	b_W	12.8 m (42 ft)
	Wing aspect ratio	W_{AR}	10.6
	Wing type	s	Box Wing
Drivetrain	Number of motors	N_{motor}	2
	Motor speed	RPM_{motor}	10,000
PEMFC stack	Design current density	j_{des}	1.33 A/cm^2
	Stack pressure	p_{stack}	1 atm
Objective (loiter endurance)			$T_9^* = 4.04$ hour

(DL), hover tip speed (V_{tip}), wing type (planar or box), wingspan (b_W), wing aspect ratio (W_{AR}), number of electric motors (N_{motor}), motor RPM (RPM_{motor}), stack operating pressure (p_{stack}), and fuel cell design current density (j_{des}), evaluating their impact across aerodynamics, structures, propulsion, and mission performance disciplines. In each of the sensitivity plots, the green star shows the design optimum.

4.2.1 Sensitivity of Number of Rotor Blades, Blade Aspect Ratio, and Rotor Solidity

The rotor profile power reduces with solidity, thus increasing the rotor Figure of Merit (FM) in hover and Lift-to-Drag ratio (L/D) in forward flight, strongly enhancing the loiter time. The reduction of solidity could be achieved by reducing the number of blades and increasing the aspect ratio. For the optimization, 2-bladed results are discarded due to vibrations, risk of mast bumping, and noise. Results above a blade aspect ratio of 20 are discarded due to aeroelastic problems. Figure 4.2(a) shows that a 3-bladed rotor with an aspect ratio of 20 is the optimal design of slenderness. Changing the blade number impacts loiter time more than the aspect ratio due to a greater impact on solidity. This is clear from the rotor system weight group sensitivity to aspect ratio and blade number (Figure 4.2(b)). For a fixed rotor radius, fewer blades and a higher aspect ratio will produce lighter blades, improving the empty weight fraction.

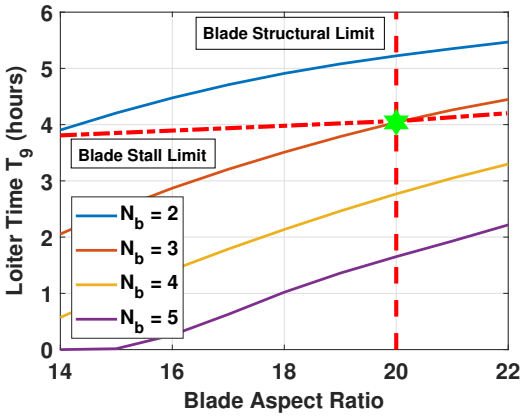

(a) Loiter time sensitivity to N_b and b_{AR}

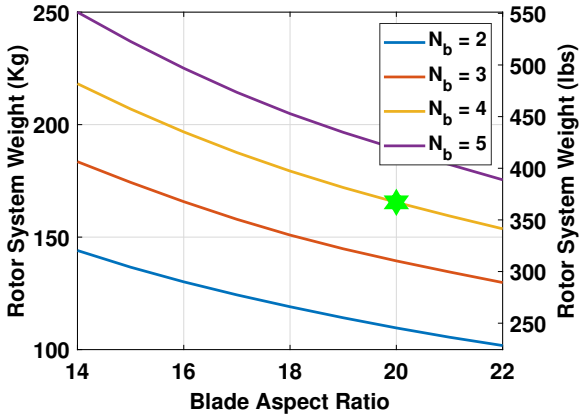

(b) Rotor group weight sensitivity to N_b and b_{AR}

Figure 4.2: Sensitivity analysis results for N_b and b_{AR}

4.2.2 Sensitivity of Hover Disk Loading and Hover Tip Speed

For a fixed rotor radius, increasing the hover disk loading increases the GTOW. This means more fuel can be carried, which increases loiter time up to a point. However, a heavier aircraft requires increased hover power and, thus, a larger PEMFC, raising the empty weight fraction. The combined effect is an optimum for the disk loading (Figure 4.3). For a specified tip speed, the maximum DL is limited by blade stall. For a specified DL, the hover tip speed can be dropped to reduce the power, increasing the loiter time. The minimum and maximum limits of the tip speed are bounded by the blade stall and the limiting tip Mach number. The minimum achievable tip speed results in the highest loiter time for any given DL. For *Wyvern* MDO, the optimum was achieved at DL=205.89 N/m^2 (4.3 lbf/ft^2) and V_{tip} = 182 m/s (597 ft/s).

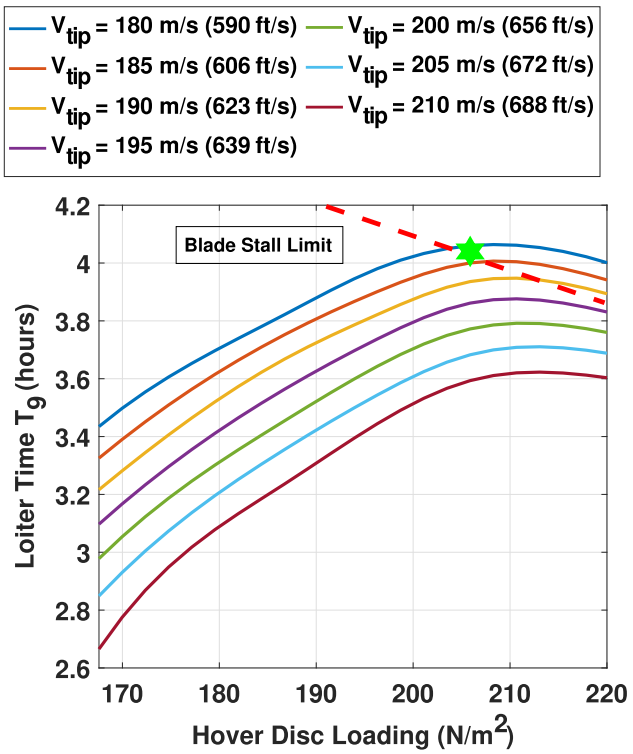

Figure 4.3: Loiter time sensitivity to DL and V_{tip}

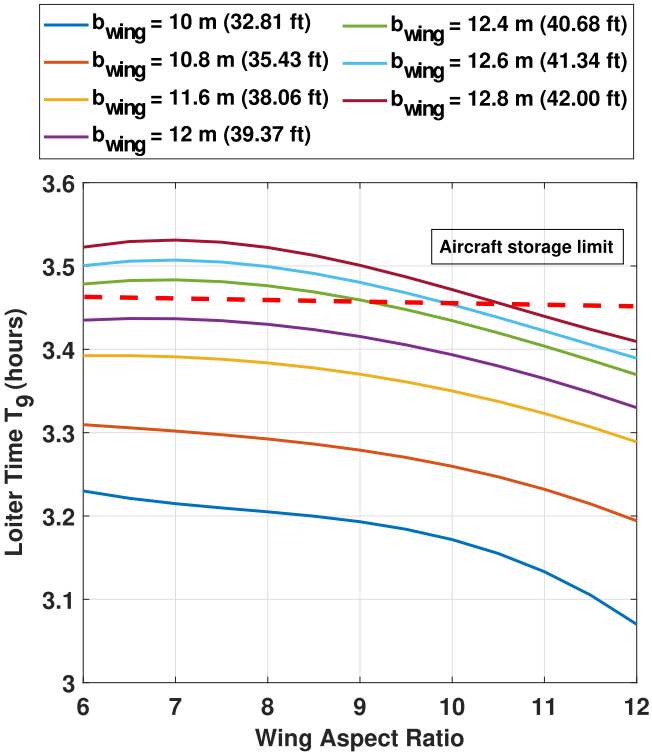

Figure 4.4: Loiter time sensitivity to planar wing b_W and W_{AR}

4.2.3 Sensitivity of Wing-Span and Wing Aspect Ratio

Loiter time is directly proportional to the aircraft cruise lift-to-drag ratio (L/D). For a given GTOW, increasing the wing's lift share enhances endurance, as the fixed wing offers far more efficient lift generation than the rotor. This can be achieved by increasing the wingspan and reducing the wing aspect ratio (W_{AR}), although each introduces trade-offs. For a fixed W_{AR}, a larger span increases wing weight. Conversely, increasing W_{AR} raises structural weight due to slenderness-induced stiffness requirements. Wing weight scales with maximum lift share, making it a key driver in endurance optimization. Loiter performance results from the combined effects of wing induced power, rotor downwash-induced hover power, empty weight fraction, and wing lift share. Structural limits constrain the maximum feasible W_{AR}, while footprint requirements constrain wingspan. Figure 4.4 presents the sensitivity to planar wing span and aspect ratio under footprint limits.

A significant 22% gain in loiter time is observed with a box wing configuration (Figure 4.5(a)) at the MDO optimum b_W = 12.8 m (42 ft) and W_{AR} = 10.6. The box wing maintains the same planform area as a planar wing but effectively doubles the aspect ratio, enhancing L/D and reducing hover download –

mechanisms detailed in Chapter 9. Corresponding weight sensitivities are shown in Figure 4.5(b).

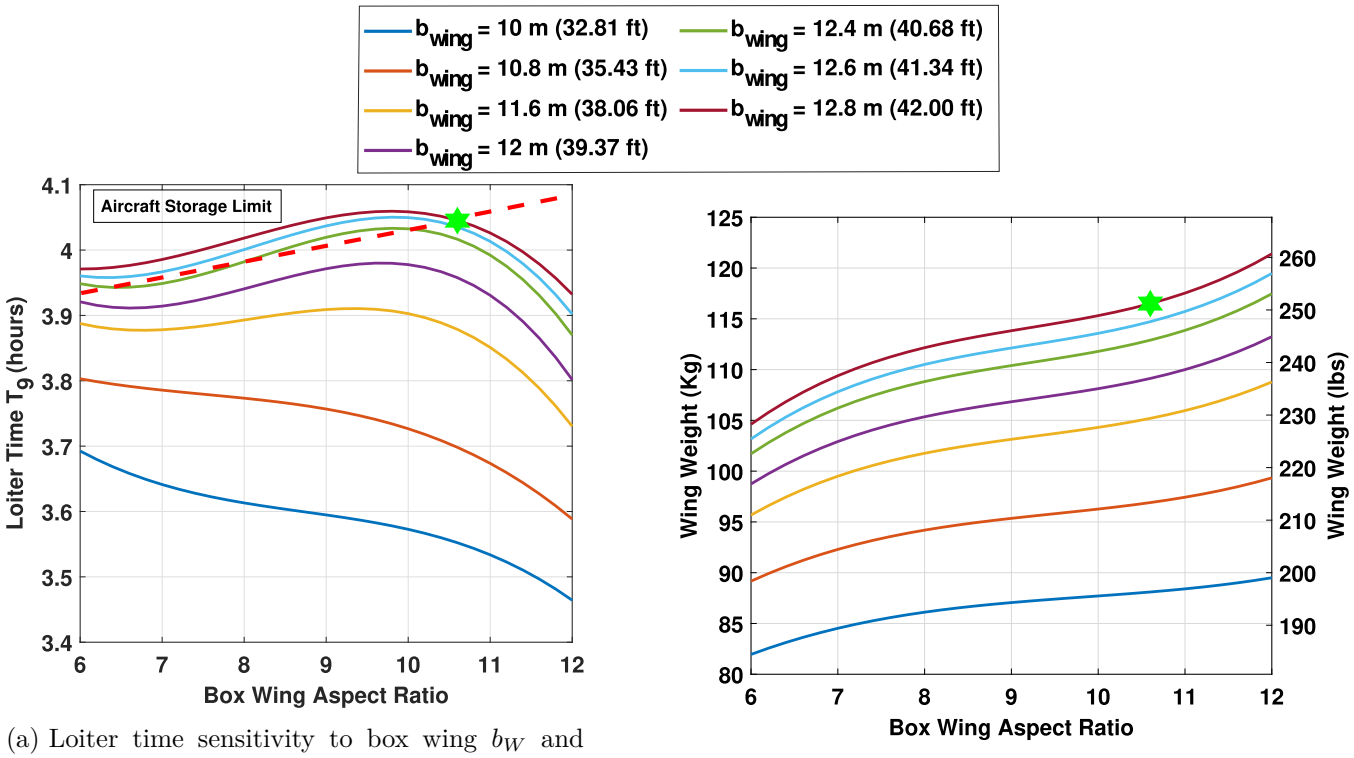

(a) Loiter time sensitivity to box wing b_W and W_{AR}

(b) Wing weight sensitivity to box wing b_W and W_{AR}

Figure 4.5: Sensitivity analysis results for box wing b_W and W_{AR}

4.2.4 Sensitivity of Number of Electric Motors and Motor-RPM:

The combined effect of the motor RPM in hover and the number of electric motors impacts the overall drivetrain weight, influencing the loiter time through the empty weight fraction. Many motors may be apparently preferable from a safety point of view, but they also add to numerous failure modes. They reduce motor weight, but add to the support structure. The combined effect was observed to be detrimental to loiter time. Higher motor RPM reduces motor torque, hence weight (weight is proportional to torque). The resulting higher gear reduction and lower efficiency of higher reduction stages increased the overall weight. The design optimization picked $N_{motor} = 2$ and $RPM_{motor} = 10,000$ in Figure 4.6(a) as the optimal drivetrain values, which minimized the calibrated AFDD drivetrain weight group in Figure 4.6(b).

4.2.5 Sensitivity of Fuel Cell Design Current Density and Stack Operating Pressure

The PEMFC stack and the High-Temperature Cooling (HTC) have been designed for the maximum power condition in the mission. These are the heaviest components of the powerplant. The system also includes the air intake, humidification, electrical, and the battery weights. For a fixed maximum power, the hover operating point in the cell i-v was selected to obtain the weight condition. The number of cells (n_{cell}), and the cell active area (A_c) were derived for this point. For a fixed stack voltage requirement, increasing j_{des} reduces the A_c, but increases the n_{cell}. The stack weight reaches the minimum towards the higher end of the current density. Whereas the cooling system weight reaches a maximum. Hence, there exists a weight optimum point. Figure 4.7 shows $j_{des} = 1.334$ A/cm^2 is the optimum for a modern cell, detail in Section 12.3.1.

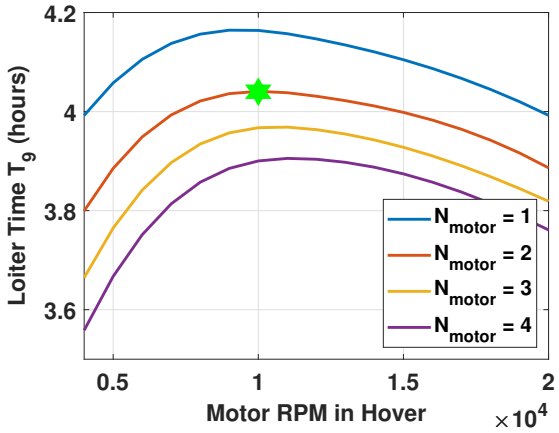

(a) Loiter time sensitivity to N_{motor} and RPM_{motor}

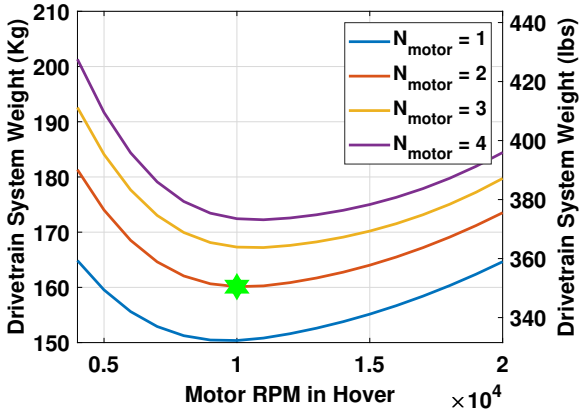

(b) Drivetrain weight sensitivity to N_{motor} and RPM_{motor}

Figure 4.6: Sensitivity analysis results for N_{motor} and RPM_{motor}

The variation of power from hover to cruise is significant, which necessitates a wide variation in the operating current density j during different segments. The specific fuel consumption (SFC) at j affected the net H_2 requirement, particularly for a loiter-heavy mission. Choosing a low j_{des} in hover would produce a very high SFC in loiter.

A slight improvement in the polarization curve was observed with stack pressure increasing from 1 atm to 1.25 atm. Hence, a sensitivity analysis was performed on the p_{stack}. However, the loiter time was higher for $p_{stack} = 1$ atm, as the weight and power requirements from the air system offset more than the benefits of a lighter stack. Operating pressure $p_{stack} \geq 1.25$ atm would necessitate a compressor and raise BOP further. This was considered unnecessary for this mission, as the maximum cruising altitude is only 300 m (984 ft) above MSL.

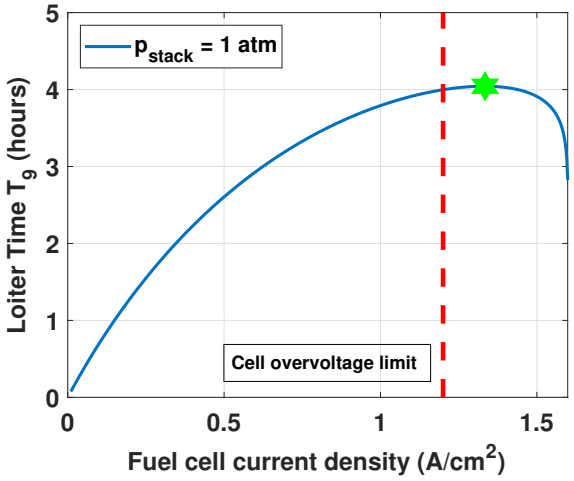

Figure 4.7: Loiter time sensitivity to fuel cell current density

4.3 Further Modification and Final *Wyvern* Specifications

Wyvern is a three-bladed SMR+L with a box wing. Although the global MDO of the aircraft resulted in the optimal parameters in Table 4.2 with loiter time $T_9^* = 4.04$ hours, the final vehicle has improved further by domain-specific higher fidelity optimizations. These improvements are listed below.

1. The main rotor and the tail rotor were optimized as explained in Chapter 6 using GA and deep learning techniques for airfoil, taper, and twist to improve both the FM and L/D.
2. The wingspan was reduced, maintaining the same aspect ratio, with taper added for more efficient lift distribution, in keeping with structural restrictions, explained in Chapter 9. The hover efficiency was improved using downward deflected trailing-edge floilers.
3. An ultralight drivetrain was designed using lightweight gears and belt design, and a supercritical driveshaft. The motor RPM was optimized to achieve high motor efficiency and low gear weights, as described in Chapter 13.
4. The stack + BOP system weight was reduced with a high-voltage electrical architecture, explained

in Chapter 12.

5. The airframe drag was reduced through component-wise drag minimization of fuselage, landing gear, and hub fairing, as explained in Chapter 17.

The improvements led to $T_9 = 4.5$ hours of loiter with a total flight time of 5 hours. The final configuration specifications are summarized in Table 4.3.

Table 4.3: *Wyvern* final selected parameters

Parameter	**Value**
Rotor Radius	5 m (16.4 ft)
Disk Loading	205.9 N/m^2 (4.3 lb/ft^2)
Number of Blades	3
Solidity	0.0477
Hover Blade Loading	0.1159
Hover Tip Speed	182 m/s (597 ft/s)
Climb Tip Speed	158 m/s (518 ft/s)
V_{climb} (forward speed)	32.5 m/s (63.2 knots)
Loiter Tip Speed	123 m/s (404 ft/s)
V_{be} (Loiter velocity)	29.3 m/s (57 knots)
Cruise Tip Speed	118 m/s (387 ft/s)
V_{br}	34.7 m/s (64.7 knots)
$V_{descent}$ (vertical speed)	39.5 m/s (76.8 knots)
Wing Area	18.75 m^2 (61.52 ft^2)
Wing Aspect Ratio	10.67
Figure of Merit	0.786
Design GTOW	1648 kg (3633 lb)
Empty Weight Fraction	87%
Loiter Time	4.48 hours
Total Mission Time	5.04 hours
Fuel Weight	24.8 kg (54.7 lb)
Power Required (max)	271.6 kW (364.2 hp)
Power Installed (max continuous)	277 kW (371.5 hp)

5 Concept of Operations

The primary mission of *Wyvern* as depicted in Figure 3.1 is to enable quiet, sustained wildlife observation above the Alligator River National Wildlife Refuge in North Carolina, USA. The mission begins and ends at the Wright Brothers National Memorial in Kitty Hawk, NC (36.0170°N, 75.6684°W), covering a 30 km (16.2 nmi) outbound and inbound route across low-lying coastal terrain. All mission segments are performed under standard atmospheric conditions (ISA), at sea level pressure and 15 (59), with zero wind, as specified in the RFP.

5.1 Unique Mission Control Capabilities

5.1.1 Collective Twist Grip

Wyvern features an innovative twist-grip throttle integrated into the collective stick, marked with five distinct modes – `IDLE`, `HOVER`, `CLIMB`, `LOITER`, and `CRUISE` – enabling intuitive rotor speed selection across mission segments. Unlike traditional collective controls, this novel interface leverages the precision of

electric propulsion to seamlessly adjust RPM via the motor control module. The twist grip simplifies pilot workload while enabling mission-adaptive rotor speed control, improving the mission performance.

5.1.2 Floiler Toggle Switch

The wings of *Wyvern* are equipped with unique floiler mechanisms to destroy the wing lift in autorotation, and reduce the wing download in hover. The design is thoroughly explained in Section 9.11. To deploy the floiler, there is a three-position toggle switch on the cyclic stick. The nominal position indicates the retracted floilers, where the up and down positions accordingly indicate the floilers deployed up or down.

Both of these actuation mechanisms are familiar to the pilot, ensuring simplicity and less training time.

5.2 Pre-Flight and Start-Up Procedure

The aircraft is fueled first, then rolled over by a pushback tractor or aircraft tug for full pre-flight inspections. It undergoes pre-flight preparation while stationed on a level concrete pad adjacent to the memorial field. The following ground procedures are conducted:

1. **Hydrogen Refueling:** It is fueled at a 700 bar (10.1 ksi) refueling interface similar to that of heavy-duty tanks. The interface hardware is H70F90 ISO 17268-1 or similar, fueling protocol SAE TIR J2601-5 F90 with communications standard IRDA/SAE J2799. Typical time of fill of *Wyvern* would be around 10 minutes. The refueling port is thermally isolated. Refueling stops automatically upon reaching maximum tank pressure, verified via pressure transducer and overpressure shutoff valve.
2. **Battery Charging:** The onboard lithium-ion battery is charged via a 240V AC ground-connected supply. Battery SOC must reach $\geq 90\%$ to complete the mission, just in case the battery fails to recharge in flight.
3. **Avionics and Power-Up:** Pilot powers on avionics using the LV DC/DC bus. A health check of the PEMFC system, cooling loops, and Battery Management System (BMS) is conducted via the cockpit display interface.
4. **Fuel Cell Start Sequence:** Twist grip is already set at `IDLE`. The PEMFC stack is initialized via the engine start button. The air blower and hydrogen regulator initiate flow into the cathode and anode sides, respectively. HV bus reaches nominal voltage (795 VDC) and stack temperature (80°C).
5. **Rotor Engagement:** Twist grip is set to `HOVER` to bring rotor to hover operating RPM of 348. Floilers (flap-spoiler control surfaces) are deflected downward by the pilot to reduce wing download. The aircraft is now ready for vertical takeoff.

5.3 Vertical Takeoff and Hover (Segments 1–4)

At takeoff, *Wyvern* initiates a controlled vertical ascent to 60 m (197 ft). The main rotor receives 77% of power from the PEMFC stack and 23% from the battery. Rotor thrust is trimmed using cyclic and collective inputs with anti-torque control via antitorque pedals.

5.4 Climb and Cruise (Segments 5–6)

Upon reaching 60 m (197 ft), the aircraft transitions to forward climb with a 9° climb angle to 300 m (984 ft) cruise altitude. Floilers are retracted to their nominal position. Pilot selects `CLIMB` mode on the twist grip. Rotor RPM reduces to 302. During this segment, the PEMFC stack alone supplies all power, where the battery stays in idle.

Figure 5.1: *Wyvern* refueling

At cruise altitude, the twist grip is set to `CRUISE`, slowing the rotor RPM to 226. *Wyvern* maintains best range speed $V_{br} = 33.3$ m/s (64.7 kts).

5.5 Steep Descent and Pre-Loiter Hover (Segments 7–8)

Upon entering the loiter zone, the aircraft performs a rapid descent to 30 m (98 ft) MSL at a vertical rate of –7.6 m/s (150 fpm) and a flight path angle of –13°, executed in autorotation mode. This maneuver begins by setting the twist grip to `HOVER`, accelerating the rotor to its nominal hover RPM. The aircraft then pitches down to maintain the desired descent angle, while the wing lift is deliberately neutralized by deploying the floilers upward. Simultaneously, the collective is dropped, and the shaft power is disengaged by switching the twist grip to `IDLE`, cutting motor power, and offloading the drivetrain. The flight battery continues to power the vehicle's avionics during this segment. As the vehicle approaches the target altitude, the twist grip is returned to `HOVER` and the collective is raised to re-establish nominal thrust. Once a controlled hover is achieved, the floilers are redeployed downward.

5.6 Loiter Phase (Segment 9)

The loiter segment is the most critical portion of the *Wyvern* mission, designed for extended wildlife observation at 30 m (98 ft) MSL over the Alligator River. The aircraft operates within a 2 km ×2 km (1.2 mi ×1.2 mi) box, executing low-speed steady flight at best endurance speed $V_{be} = 29.3$ m/s (57 knots). Floilers are retracted. The pilot sets the twist grip to `LOITER`, adjusting rotor RPM to 235. Altitude and speed hold modes engage through the dual-axis SAS. Collective and cyclic trim are stabilized to maintain height and heading. The PEMFC stack supplies all propulsion power. Reduced rotor thrust and retracted floilers reduce drag and improve endurance. The flight battery is recharged via the HV DC bus. *Wyvern* stays in its loiter phase for 4.5 hours.

5.7 Return Climb, Cruise and Descent (Segments 10–12)

The aircraft transitions back to climb mode, ascends to 300 m (984 ft), and cruises back to Kitty Hawk using the same optimized rotor RPMs. Then it performs a steady descent up to 60 m (197 ft) above MSL at 5° glide slope, with the twist grip set to `HOVER` mode.

5.8 Contingency Hover, Descent, Landing, and Shutdown (Segments 12–16)

HOGE at 60 m (197 ft) above MSL, vertical descent to HIGE, and landing are performed once the aircraft returns to the initial takeoff position. Rotor RPM is gradually reduced after touchdown by twisting the grip back to `IDLE`. PEMFC is turned off using the engine switch. The aircraft is powered down and secured.

6 Blade Aerodynamic Design

Maximizing the loiter time by increasing cruise L/D, along with sufficient hover performance by increasing the FM, necessitates a rigorous rotor optimization. A multi-objective constrained design optimization was performed for blade design.

Traditional design optimization frameworks like grid or random search become computationally expensive without guaranteeing a global optimum. Special care has to be taken for gradient-based methods as they are more likely to get stuck in local minima. Therefore, there has to be a balance between computational cost for the optimization process and the robustness of the optimizer.

In this work, Genetic Algorithms (GA), which is an evolutionary optimization algorithm, are used. The framework of GA is explained in section 4.1. A multi-objective optimization is employed for two important mission segments: hover and loiter. UMARC-II [35], an in-house comprehensive code, is used to evaluate performance parameters and embedded with the GA.

6.1 Design Objective

The objectives of the aerodynamic optimization is to increase the loiter time. There are two key objectives: the FM of the rotor and L/D of the aircraft. The L/D throughout this report represents the lift-to-drag ratio of the entire aircraft as presented in Equation 4. Since the magnitude of FM and L/D have an order of magnitude difference, weights are added to ensure equal preference is given to both. In Equation 6, w_1 and w_2 are the weights used for FM and L/D . In addition, preferential weights (α_1 and α_2) are added to change the order of preference. The preferential weights α_1 and α_2 are varied between 0 to 1 such that their sum is always equal to 1. The objective function is defined by Equation 6:

$$\frac{L}{D} = \frac{Weight}{Power/Velocity} \tag{4}$$

$$Power = \text{Main Rotor Shaft Power } = P_{induced} + P_{profile} + P_{propulsive} \tag{5}$$

where $P_{propulsive}$ overcomes aircraft drag.

$$J = \alpha_1 \cdot w_1 \cdot FM + \alpha_2 \cdot w_2 \cdot (L/D) \tag{6}$$

6.1.1 Design Space

A wide range of design space is considered for rotor optimization. There are 8 design variables as presented in Table 6.1. A bilinear-twist is allowed along the span with a variable twist location. A single taper ratio is allowed with a variable taper location. Two airfoil geometries are allowed along the span. The first airfoil near the root is chosen from 10 standard rotorcraft airfoils as presented in Table 6.1. The second airfoil from 73% span to tip is inverse-designed using an in-house Neural Networks solver, Alfred Gessow Rotorcraft Center - Airfoil Polar Predictor (AGRC-APP) [36–38]. AGRC-APP uses Tandem Neural Networks (TNNs)

to generate an airfoil geometry for a given target performance polar with geometric constraints. The airfoil in the outboard section (73% to tip) is specially designed and is called AGRC-foil8. AGRC-foil8 has a maximum thickness of 8%. Optimization ensures that the inboard airfoil is thicker and the outboard airfoil is thinner. Constrained GA ensures a constant solidity throughout.

Table 6.1: Design space for Genetic Algorithm

Geometric Variables	**Lower bound**		**Upper bound**
Inboard twist rate (deg)	0		20
Outboard twist rate (deg)	0		20
Twist junction (r/R)	0.4		0.7
Taper ratio	1		3
Taper location (r/R)	0.4		0.7
Inboard Airfoil	NACA0012	OA212	RC4-10
	OA209	RC3-8	SC1012R8
	SC1095	SSCA09	VR12
	VR15		
Outboard Airfoil	AGRC-foil8		
Airfoil transition	0.3		0.9

6.1.2 Baseline and Optimized Blades

A HART-II blade is modified to a radius of 5 meters (16.4 ft) and an aspect ratio of 20 is chosen as a baseline. The blade is trimmed at the same thrust level and shaft tilt as that of the target. UMARC-II is executed for the baseline blade to determine its FM and L/D . A multi-objective optimization is also performed with 8 design features as explained in Table 6.1. From the baseline to the optimized rotor, an improvement of 15.4% is achieved in FM (reduction in power by 12.7% in hover) and 23.5% in L/D (reduction in power by 19.6% in loiter). The comparison of performance of baseline and optimized rotor is presented in Table 6.2. The improvement of FM and L/D with generations is presented in Figures 6.3(a) and 6.3(b). The trend of improvement of L/D with generations in Figure 6.3(b) is interesting. The improvement in L/D in the first generation is from 7.31 (baseline rotor L/D) to 8.94 and this increases to 9.03 after 20 generations. Every generation has 800 unique solutions and the GA picks the best among them.

Table 6.2: Comparison of performance of baseline and optimized rotor

Main Rotor Design	**FM**	**L/D**	**Power Loading N/kW (lbf/hp)**
Baseline	0.681	7.31	41.5 (12.51)
Optimized	0.786	9.03	46.7 (14.10)

6.1.3 Navigating Tradeoffs

A combination of optimization cases with varying weights (α_1 and α_2) is performed to determine the best balance between the competing objectives; FM and L/D. For each weight fraction, the optimizer samples 40 distinct cases for 20 generations, making a total of 800 cases (Figure 6.3). The best among these cases is selected to plot a Pareto-frontier as presented in Figure 6.1. As can be seen in Figure 6.1, the L/D does not vary as much as the FM. This slowed rotor compound design allows the wing to bear most of the lift in loiter. The optimized L/D is significantly higher (23.5%) than the baseline. From this Pareto plot, the blade design corresponding to the FM of 0.786 and the L/D of 9.03 is selected.

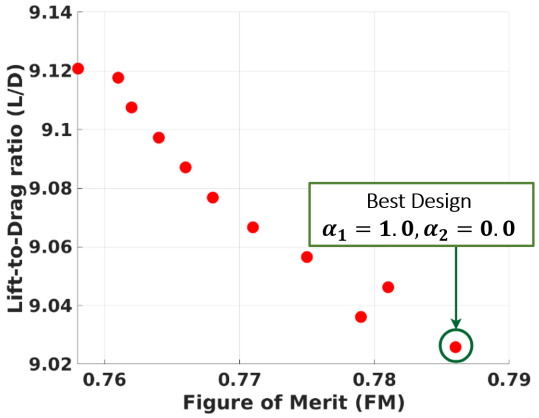

Figure 6.1: Pareto frontier for FM and lift-to-drag ratio

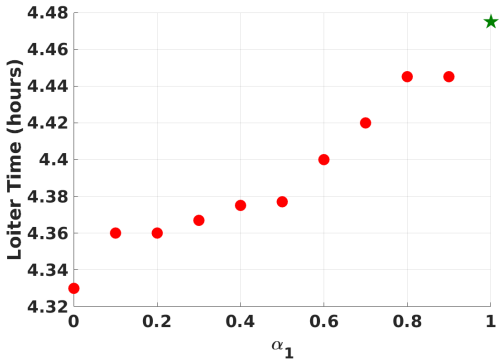

Figure 6.2: Loiter time vs. weight fraction given to FM (α_1)

6.1.4 Optimized Rotor Geometry

From the Pareto-Frontier in Figure 6.1, the top performing design is selected where the FM is 0.786 and L/D is 9.03. The optimum geometry corresponds to the weight distribution of 1 for FM and 0 for L/D ($\alpha_1 = 1$ and $\alpha_2 = 0$). This weight distribution is particularly interesting because the objective of the optimization is to maximize the loiter time, but the highest weight fraction is given to the FM to select the optimal geometry. A very high power in hover increases the size of the stack significantly (for a fixed battery weight and C-rate), which in turn increases the empty weight and hence, reduces the loiter time. This was an interesting observation, where the weight of the powerplant is significantly increased with a small increase in power, unlike combustion engines. The comparison of loiter time with α_1 is presented in Figure 6.2, where it is observed that $\alpha_1 = 1$ for FM gives the highest loiter time.

The chord and twist distribution of the optimized rotor blade is presented in Figures 6.4 and 6.5. The optimized blade has a constant chord from root to 60% of span and tapers linearly to the tip. It has a bi-linear twist of -16°and -13°outboard with the junction at 70% span. It has a taper ratio of 1.7 from 60%R to tip. The twist rate ensures near-uniform inflow in hover while avoiding negative lift at the tip region in loiter. Two airfoil geometries are used along the span, RC410 from root to 67%R and AGRC-foil8 from 73% span to tip. The details of the optimized main rotor blade are presented in Table 6.3. Figure 6.6 shows the comparison of RC(4)-10 and AGRC-foil8. The tip region has higher dynamic pressure, and therefore, a thinner airfoil has better aerodynamic performance near the tip. The thicker airfoil provides better structural stiffness, whereas the thinner airfoil extends the stall margin at higher Mach numbers. The profile of the optimized rotor blade is presented in 6.7.

7 Blade Structural Design

Wyvern features a three-bladed articulated main rotor constructed from advanced composite materials, selected for their superior fatigue life, high specific strength, and tailored stiffness properties. The blade structure is optimized to withstand the combined effects of centrifugal forces, steady aerodynamic loads, and oscillatory loads in flap, lag, and torsion. It is designed for a fatigue life of 5000 hours. To minimize vibratory loads at 3/rev, the rotor was designed with targeted modal characteristics. A (first) flap frequency of 1.031/rev ensured enough controllability, a (first) lag frequency of 0.49/rev mitigated ground resonance and in-plane vibratory loads, and a (first) torsion frequency of 6.4/rev reduced pitch link loads. A sectional center of gravity (C.G.) at quarter chord (1/4-c) eliminated pitch-flap flutter.

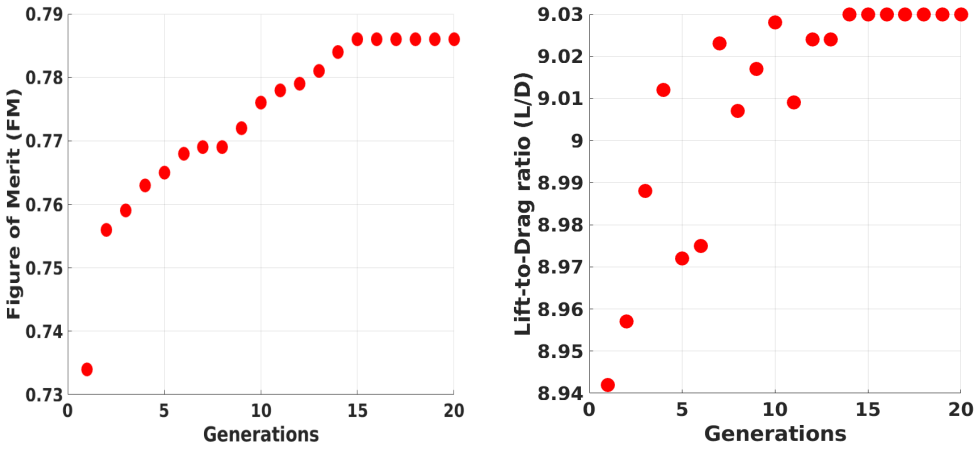

(a) FM vs Generations (b) L/D Loiter vs Generations

Figure 6.3: Improvement of FM and L/D with generations

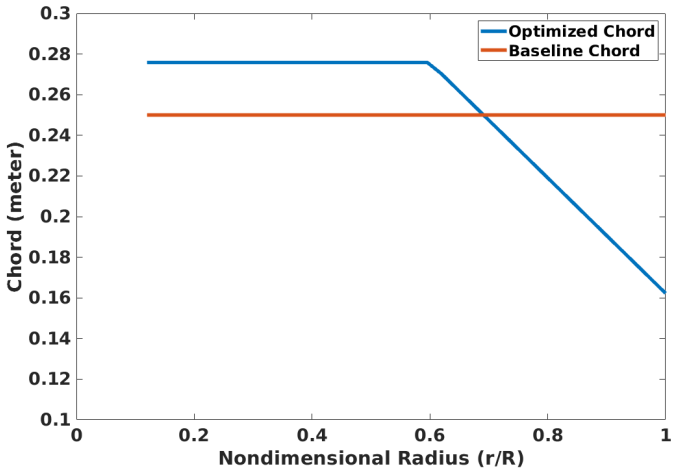

Figure 6.4: Chord distribution of optimized main rotor

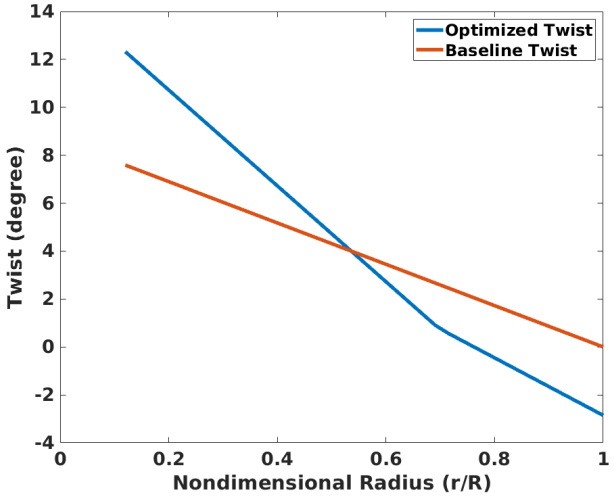

Figure 6.5: Twist distribution of optimized main rotor

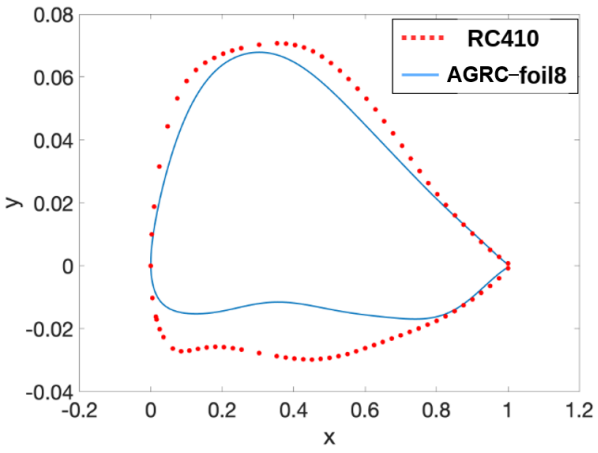

Figure 6.6: Baseline and optimized airfoils

Table 6.3: Optimized main rotor geometry

Geometric Variables	Optimized values
Radius	5 m (16.4 ft)
Root cutout	12%
Inboard Twist rate (deg/span)	-16
Outboard Twist rate (deg/span)	-13
Twist junction (r/R)	0.70
Taper ratio	1.70
Taper location (r/R)	0.60
Inboard Airfoil	RC410
Outboard Airfoil	AGRC-foil8
Airfoil transition (r/R)	0.67-0.73

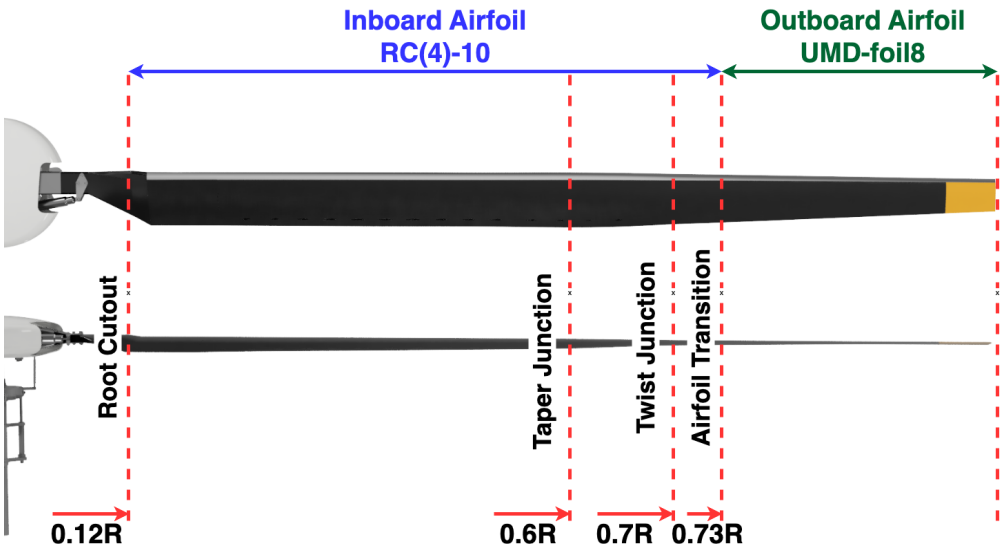

Figure 6.7: Profile of the optimized main rotor

7.1 Structural Design

An in-house Finite Element Analysis tool was utilized to design and calculate blade stiffnesses and inertias along the span, considering varying airfoils, skin and spar, taper and twist, tuning masses, ply orientations, and ply drop-off. The design parameters included the shape and location of the spar, the thickness of the spar, fillers (foam or honeycomb), leading-edge weights, and material properties for all components. To prevent pitch-flap instability, leading-edge weights maintain the C.G. at the quarter-chord (1/4-c).

The spanwise stiffness and inertial properties were inputs to UMARC-II, which modeled flap, lag, and torsion to calculate natural frequencies for all of the rotor operational speeds and blade root shears and moments, and the hub loads. Thus, the blade loads were used to size the D-spar and number of plies. The final blade structure is shown in Figure 7.1. From the hub, the blade grip attaches to a forked root cutout section that spans 12% of the blade radius. The forked geometry was chosen because of the positive reactions with centrifugal loads. The fork evenly distributes these loads to separate connections to the hub, while the centrifugal forces pulling on the fork cause it to clench together, tightening the connection to the hub and further securing the blade, thus enhancing safety. The root insert section has titanium bushings through which the bolts connecting the blade to the hub are inserted and centrifugal loads are transferred. Within the root cutout, a graphite epoxy spar wraps fully around the titanium bushings, running throughout the cutout and becoming the D-spar. The cutout region smoothly transitions to the lifting surface between 10%R and 15%R. The profile of the transition region was made airfoil-shaped. The primary lifting surface spans from the transition region to the tip of the blade to maximize the lifting area.

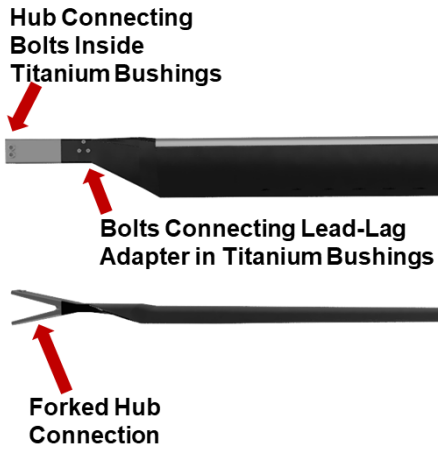

Figure 7.1: Rotor blade-hub connection

7.2 Internal Structure

A cross-sectional view of the internal structure is shown in Figure 7.2. The D-spar, the primary load-carrying component, is composed of unidirectional T300 graphite-epoxy plies. The most inboard section

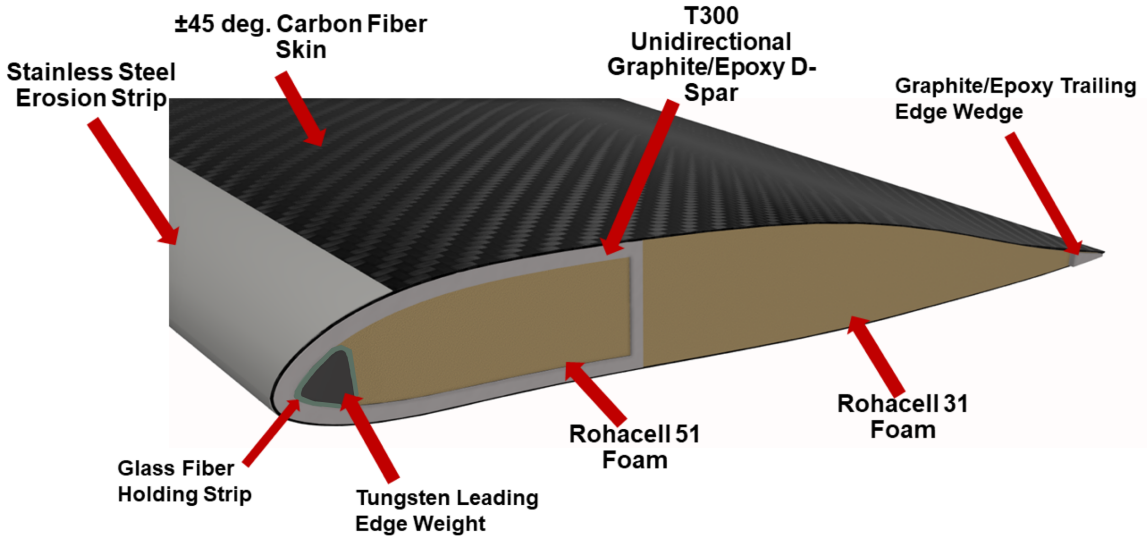

Figure 7.2: Cross-section of the main rotor blade

utilized eight plies, with a drop-off to four at the thinner tip. The plies are given in [0/90/0/0/90/0/0/90]. The unidirectional [0°] fibers are intermixed within the [90°] fibers to reduce the likelihood of delamination and mitigate the coalescence of microcracks. Being a simple closed shape, the D-spar provides sufficient supplemental torsional stability while maintaining simplicity of manufacturing. The number of D-spar plies was primarily determined from the UMARC-II centrifugal load in hover, with a factor of safety of 3. Accordingly, the root flap and chord bending moments in hover were calculated to ensure the bending strain of the spar is well below the allowable strain. Figure 7.3 shows the oscillatory 1/rev root moments during the loiter phase impacting the high-cycle-low-stress fatigue. The equivalent strain was computed for this loading cycle, and the ply layup was ensured to withstand it. The center of gravity is maintained at 24.9% chord throughout the blade by tungsten leading edge weights placed within the D-spar. The leading edge weights are shaped to the inner leading edge of the D-spar and are separated from the spar by a thin glass fiber layer to prevent displacement. The second flap mode was pushed away from resonance using an antinodal mass at 0.35 R. This mass is positioned aft of the D-spar and is held in place by a glass fiber sling. Glass fiber was chosen for both of these applications due to its ease of workability and low cost. The blade skin consists of four layers of ±45° carbon fiber weaves, supplying the majority of the necessary torsional stiffness. A trailing edge wedge of 7% chord of unidirectional graphite epoxy resists skin delamination and provides lag stiffness. The hollow portion within the D-spar consists of Rohacell 51 foam to maintain the airfoil profile. This foam, with a density of 51.2 kg/m^3 (0.1 slug/ft^3), is less expensive and easier to manufacture compared to a honeycomb material. The foam after the D-spar is Rohacell 31, which has a lower density of 31 kg/m^3 (0.06 slug/ft^3). This lighter foam is chosen so that the C.G. positioning accomplished by the leading edge weights is not counteracted by a heavier aft mass. A stainless steel erosion strip is placed over the leading edge to protect against corrosion.

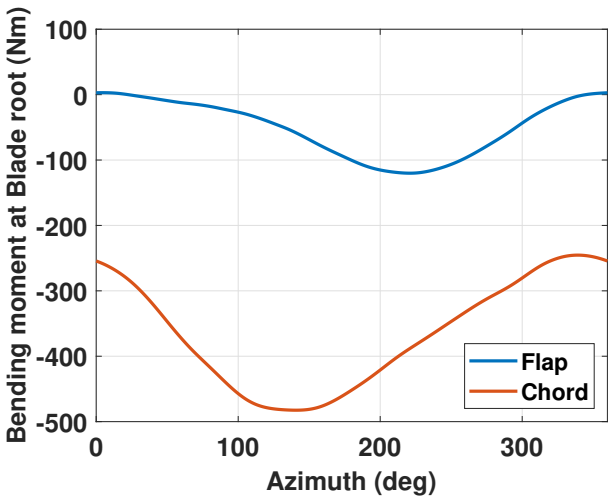

Figure 7.3: Flap and chord bending moments at blade root in loiter.

7.3 Blade Manufacturing

First, the leading edge Rohacell 51 foam is machined to the internal shape of the D-spar. Slots for the tungsten leading edge weights are evenly cut into the foam, and individual weights, each wrapped on a layer of glass fiber, are placed throughout the blade span so they are flush to the foam. Using automated fiber placement, Graphite/Epoxy fibers are laid over the foam and leading edge weights, sweeping from root to tip and back to root, accurately creating the forked root section and wrapping around the titanium bolt bushings (Figure 7.4). This is done from the top to the bottom of the spar until the complete spar is formed. This automated fiber placement process accurately captures the blade twist, taper, ply drop-offs, and airfoil changes. The entire D-spar assembly is then cured in a mold. The outer profile Rohacell 31 foam core is machined to the required airfoil profile and pressed to the back of the D-spar. The trailing edge wedge plies are then laid using automated fiber placement.The four $\pm 45°$ plies of carbon fiber are wrapped around the entire blade, including the root cutout, transition region, and blade lifting region. Next, the blade is placed in an aluminum mold to cure, which includes a pocket to compensate for the thermal expansion of the aluminum. Once cured, a preformed stainless steel erosion guard is bonded to the leading edge.

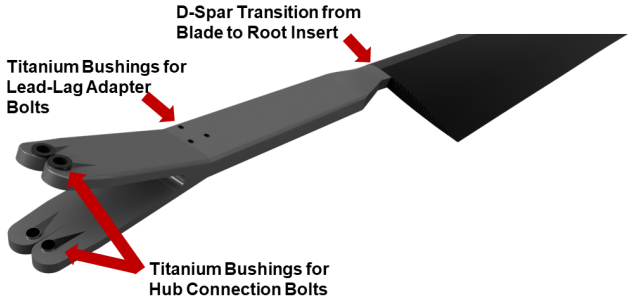

Figure 7.4: D-Spar transition from blade to forked hub connection

7.4 Blade Properties

Each main rotor blade of *Wyvern* weighs 20 kg (44 lb), reflecting a lightweight composite construction optimized for high performance and low vibratory structural loading. The non-dimensional flap, chord, torsion stiffnesses and mass are shown in Figure 7.5. The structural layout integrates ply drop-offs and material transitions to achieve desirable dynamic properties across various operating conditions. The D-spar begins from the very blade connection to the hub, designed to provide sufficient load-carrying capability, allowing for controlled compliance and transition of bending loads. The blade aerodynamic surface initiates at approximately 12% span. Outboard of the root cutout, the sectional properties are determined by the skin, spar, and leading-edge mass, with spanwise variations due to airfoil taper, ply drop-offs, and aerodynamic tailoring. To optimize vibratory performance, a discrete tuning mass of 3.82 kg (8.4 lb) is incorporated at the 35% span station. This mass placement shifts the second flap frequency away from 3/rev primary excitation harmonics, helping to reduce vibratory loads during forward flight.

The first flap frequency is 1.031/rev, providing enough control bandwidth for the required mission while avoiding any excessive hub moments. The first lag frequency is tuned to 0.49/rev, striking a balance between enough stiffness for ground resonance avoidance and limiting higher steady and vibratory loads. In contrast to stiff in-plane systems, which often demand active vibration control, *Wyvern* mitigates hub loads by integrating a moderately soft in-plane rotor design coupled with wing lift sharing during cruise and rotor speed variation at high advance ratios (μ up to 0.27). The first torsional frequency is positioned at 6.4/rev, sufficiently high to ensure aeroelastic stability across the flight envelope. This high torsional stiffness, combined with the relatively low advancing tip Mach number, keeps pitch link loads within acceptable limits.

The first seven natural frequencies for all the operating rotor speeds are shown in Table 7.1. Figure 7.6 shows the fan plot of the main rotor. All modes are adequately separated from critical /rev crossings, avoiding resonance and ensuring robust aeroelastic and vibratory performance throughout the mission. Overall, *Wyvern*'s rotor blends simplicity with high performance.

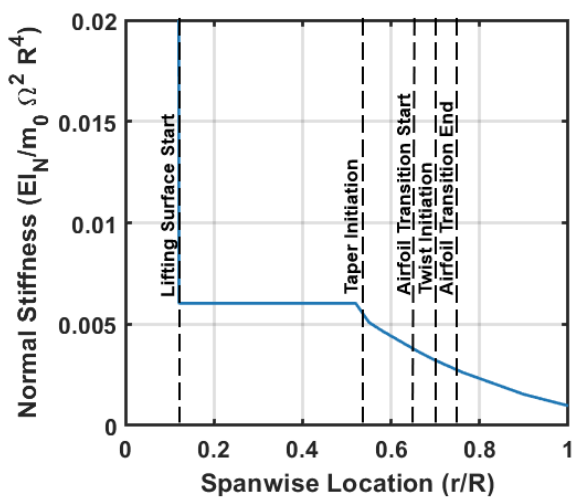

(a) Flap stiffness distribution

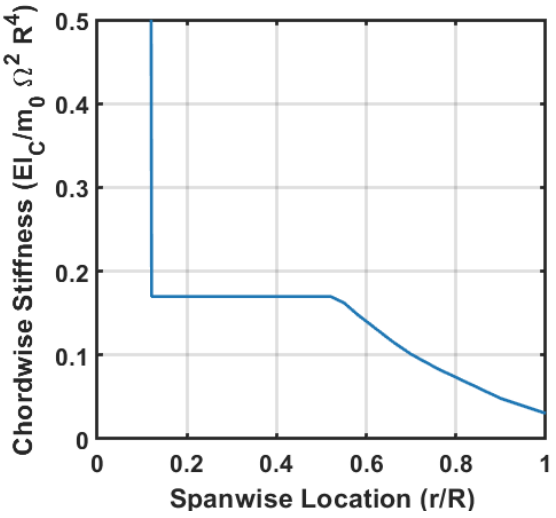

(b) Lag stiffness distribution

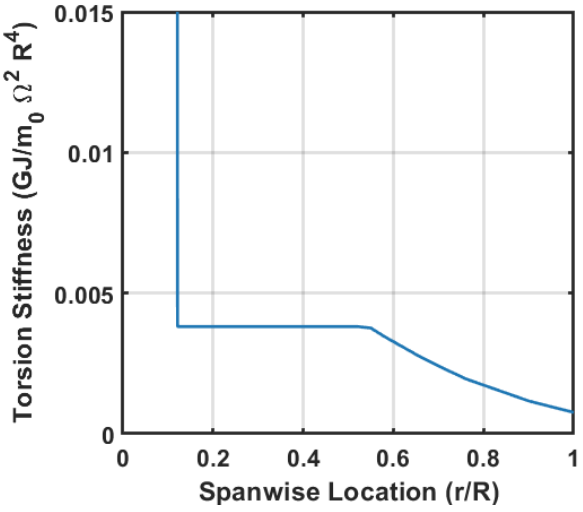

(c) Torsional stiffness distribution

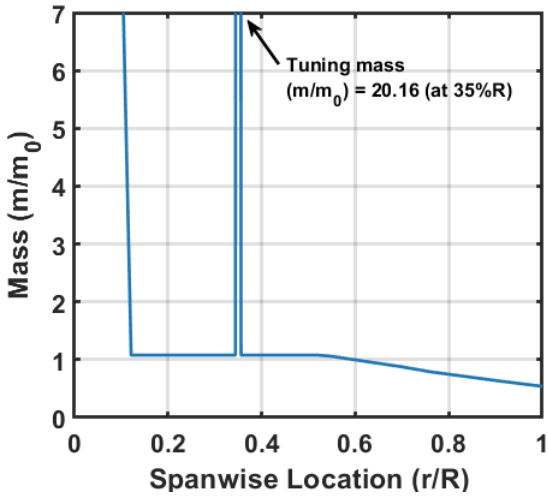

(d) Mass distribution

Figure 7.5: Main rotor sectional properties; Ω is rotor speed in hover, $m_0 = 4$ kg/m (2.7 lbf/ft)

7.5 Aeroelastic Stability Analysis

Aeroelastic instabilities were rigorously evaluated to ensure sufficient stability margins under hover and high-speed cruise conditions.

7.5.1 Pitch-Flap instability

Pitch-flap instability arises from dynamic coupling between the blade torsional and flapping modes, potentially leading to diverging oscillations. This instability is strongly influenced by the torsional frequency and the C.G. location relative to the pitch axis (at the quarter chord). For *Wyvern*, the first torsional frequency is placed at 6.4/rev by tuning the pitch link stiffness to enhance the system compliance to pitch deformations and provides robust aeroelastic stability under varied rotor RPMs. The blade C.G. is located at 24.9% chord, slightly ahead of the (1/4-c) point, which is favorable for pitch-flap decoupling. Figure 7.7(a) presents the pitch divergence and pitch-flap flutter boundaries as a function of C.G. location and torsional frequency.

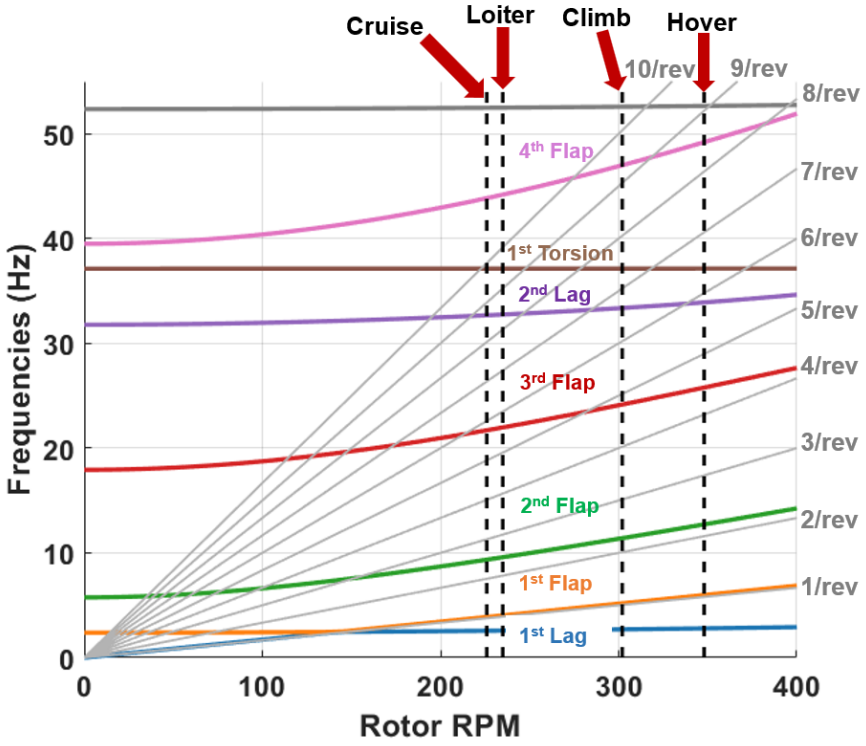

Figure 7.6: Fan plot of main rotor blade

Table 7.1: Rotor mode frequencies (in /rev) vs rotational speed (in RPM)

Omega (RPM)	1st Lag	1st Flap	2nd Flap	3rd Flap	2nd Lag	1st Torsion	4th Flap
348 (Hover)	0.49	1.03	2.19	4.44	5.85	6.40	8.48
302 (Climb)	0.54	1.03	2.27	4.80	6.63	7.38	9.34
235 (Loiter)	0.66	1.03	2.45	5.61	8.36	9.48	11.28
226 (Cruise)	0.68	1.03	2.48	5.76	8.68	9.86	11.64

7.5.2 Flap-Lag Flutter

Flap-lag flutter is another coupled instability, driven by the interaction of flapping and lagging motions of the blade, from Coriolis and structural coupling, particularly exacerbated by low aerodynamic damping in the lag direction. *Wyvern* employs a moderately soft-in-plane articulated rotor with first flap and lag frequencies at 1.03/rev and 0.49/rev, respectively. This rotor is, by design, much less likely to go into Flap-lag flutter, unless in hot and high conditions, not required by the RFP. Figure 7.7(b) shows the egg plots with increasing blade loading, clearly illustrating that the design is well outside of the flutter boundary. Any chance of stall flutter is also mitigated by the high torsional frequency. Furthermore, the damping from the elastomeric lead-lag adapters is enough to avoid any unfavorable conditions.

7.5.3 Ground and Air Resonance

Ground resonance is a dynamic instability resulting from the coupling between the rotor regressive lag modes and the fuselage/landing gear modes. It is especially a concern for soft in-plane rotor systems and during operations on compliant or uneven terrain, where reduced damping and structural asymmetry can initiate diverging oscillations. The support frequencies of the landing gear were analyzed using the Finite Element Method in a zero support damping condition with rigid body mass and inertia properties for the fuselage provided. The landing gear frequencies were 4.05 Hz and 8.85 Hz for body roll and pitch, respectively. Although *Wyvern* employs a moderately soft in-plane rotor to reduce vibratory hub loads,

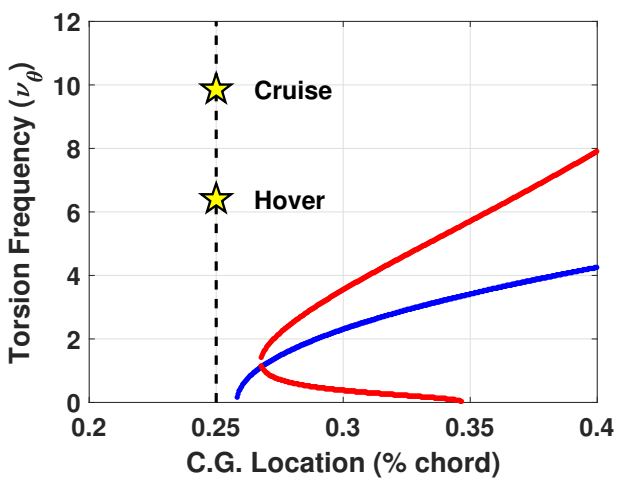

(a) Pitch-flap stability boundaries

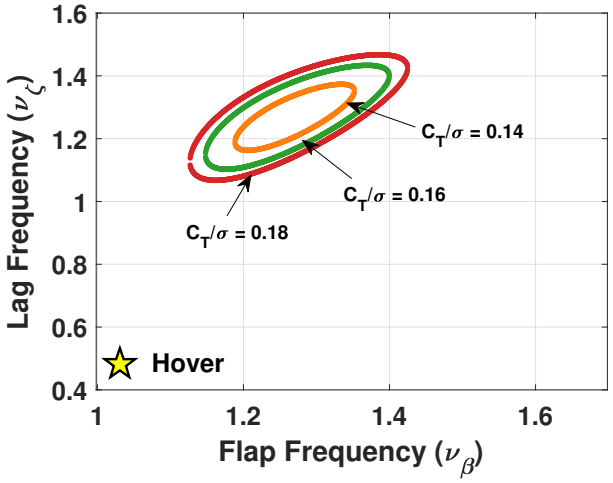

(b) Flap-lag stability boundaries

Figure 7.7: Pitch-flap and flap-lag aeroelastic stability margins

the design has been carefully tailored to maintain sufficient separation between airframe and rotor dynamic modes. This includes achieving the 1st lag frequency (0.49/rev) via tuning the elastomeric lead-lag adapter stiffness to prevent modal coalescence. Figure 7.8(a) presents the coupled rotor-fuselage eigen analysis for *Wyvern* rotor system, showing that the first fuselage roll mode and regressing lag modes remain well-separated across the full rotor operating speed range, including low-RPM ground idle conditions. The critical ground resonance crossing—where an instability could potentially arise—was observed at a rotor speed of 41.5 rad/s (397 RPM), well above hover and cruise RPM ranges. At this crossing, the damping ratio was computed as 4.6% (Figure 7.8(b)), which will be provided by the damping from the lead-lag adapter. Henceforth, *Wyvern*'s integrated damping exceeds these minimums, providing a robust margin against ground resonance.

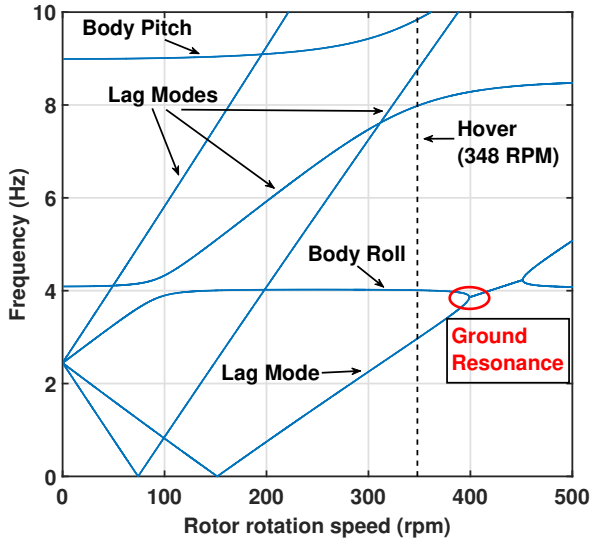

(a) Stability analysis of ground resonance

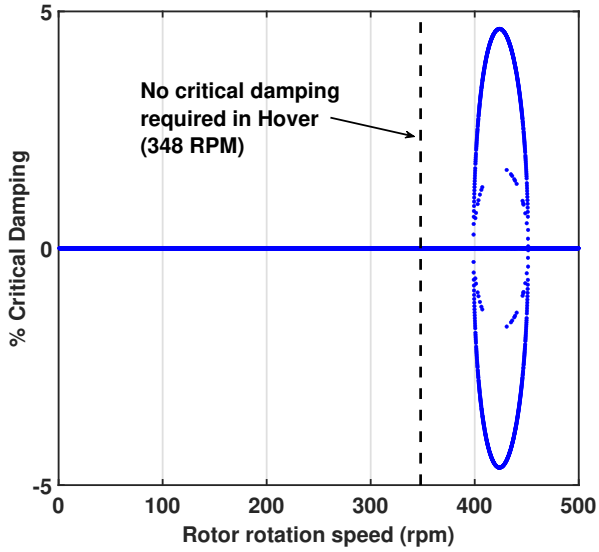

(b) Damping ratio of unstable mode for ground resonance

Figure 7.8: Ground resonance analysis for *Wyvern*

8 Hub Design

The rotor hub holds the blades, absorbs the loads, ensures stability, and connects the load path to the main shaft. It acts as a filter, transmitting only loads that are integer multiples of N_b/rev. *Wyvern* hub was designed for both steady and oscillatory hub forces and moments, along with a fatigue life of 5000 hours. Several types of hubs were analyzed before a fully articulated hub, with elastomeric bearings, inspired by Guimbal Cabri G2 [39], was selected. This hub achieves the following goals: 1) simple geometry and lower part count for lower manufacturing costs and easier maintenance; and 2) compact design and cleaner shank for low hub drag in loiter. A detailed assembly of the hub, swashplate, and pitch links, along with the necessary components, is provided in this section.

8.1 Hub Selection

For *Wyvern*, six key criteria guided the selection of the main rotor hub architecture to meet the demands of a simple and cruise-heavy mission profile: weight, drag (with fairing), control authority, parts count and maintenance, design and manufacturing complexity, and vibration level. The rotor needed to maintain adequate control authority in HIGE, HOGE, and vertical climb/descent segments. Since *Wyvern* includes significant loiter and cruise segments, to maximize the loiter time, low hub drag is important for minimizing power consumption. Low vibration is critical to improving ride quality. Hence, low weight and drag are critical to maximize vehicle performance for both mission segments. A low part count decreases part manufacturing and maintenance costs and time. The hub system also needed to be mechanically robust, simple in design, and resistant to particulate intrusion—essential for reliability and longevity in wetland environments. A rating matrix was used, evaluating hub types across these criteria on a scale from +5 (excellent) to -5 (poor), with 0 as neutral. Table 8.1 shows the hub selection matrix.

Table 8.1: Hub type selection matrix

Hub Type	Weight	Drag (with Fairing)	Control Authority	Parts count & Maintenance	Design & Manufacturing Complexity	Vibration Level	Total
Weight	0.22	0.24	0.12	0.11	0.15	0.16	1
Fully Articulated: Mechanical	0	0	0	0	0	0	0
Fully Articulated: Elastomeric	2	1	0	2	3	0	1.35
Semi Articulated	2	1	2	3	1	-1	1.24
Hingeless	4	2	3	4	-2	-4	1.22
Bearingless	3	3	3	3	-3	-3	1.14

Fully Articulated with Mechanical hinges: Articulated hubs require mechanical hinges to allow flap, lag, and pitch motion. The hinges increase part count, weight, complexity, and forward flight drag. These hubs also require continuous maintenance to ensure that the hinges are properly lubricated and free of contaminants. Articulated hubs with hinge offsets produce flap frequencies of 1.03-1.06/rev, which is adequate for a loiter-specific mission without aggressive maneuvers.

Fully Articulated with Elastomeric hinge: The mechanical hinges of the fully articulated hub are replaced by a single elastomeric bearing in this hub. Laminated elastomeric bearings require no lubrication and are lighter than conventional antifriction bearings for a given load capacity. Spherical elastomeric bearings are the most suitable for rotor systems. These bearings employ spherically shaped laminates, can support combined loads, and permit oscillatory motion in any plane. It replaces the tension-torsion strap

by resisting the centrifugal force and also performs the functions of virtual flap, lag, and pitch bearing. Hence, this hub design was selected.

Semi-Articulated: Semi-articulated hubs use flexures for flap and elastomeric bearings for pitch and lag motions. They are moderately gust tolerant and provide increased control authority compared to a fully-articulated hub, also increasing hub vibratory loads. However, the combined design of the flap flexure for precise control authority, along with an elastomeric bearing, relatively increases the weight and the number of parts required, raising the design complexity, and reducing robustness.

Hingeless: Hingeless hubs use flexures for flap and lag while retaining a bearing for pitch control. Higher control bandwidth is achieved from flap frequencies near 1.1/rev at the expense of higher out-of-plane vibratory loads. Hingeless hubs have a low part count and hub drag. However, they are also gust sensitive, and the soft-in-plane hub designs require elastomers for damping augmentation. Stiff-in-plane worsens the situation with an increase in in-plane vibratory loads, although reducing the overall weight. Precise design is required for careful property and frequency placement, increasing design and manufacturing complexity.

Bearingless: Bearingless hubs are essentially hingeless hubs with an expensive lag damper. They typically require a torque tube to house the snubber damper. Bearingless rotors are mechanically simple designs in which all three degrees of motion are controlled by the flexure design of the hub. However, because of redundant load paths, these designs add a significant level of complexity to the structural dynamics design and, because they have little in-plane damping, are more susceptible to aeromechanical instabilities.

8.2 Hub Assembly

The articulated hub assembly, made in Ctia v5, is shown in Figure 8.1. Major components include the aerodynamic hub fairing, the hub yoke, the elastomeric bearings, the lead-lag adapters, scissor arms, swashplate, and the splined rotor shaft, shown in Figure 8.2. The mast retention nut secures the hub assembly to the rotor shaft via secured threading in the direction of rotor rotation. It includes a wedge-lock mast retention washer that acts as a positive locking device, preventing the bolt from loosening due to vibrations. This bolt also serves as the attachment point for the hub fairing. The rotor shaft securely attaches to the hub yoke using a splined interface. The hub yoke attaches to a spherical elastomeric bearing via a bolt connection. Titanium Ti-6Al-4V alloy was selected for the hub yoke due to its high fatigue life and high strength-to-weight ratio. The hub yoke is surrounded by a fiberglass winding layer to provide additional stiffness and a factor of safety from the centrifugal loading. Both the rotor blade and pitch horn are attached directly to the elastomeric bearing, which allows rotation in flap, lead-lag, and pitch. The pitch horn contains a ball joint connection to the pitch links, chosen to alleviate the bending stresses on the pitch links. A lead-lag adapter was installed to dampen lead-lag movement, increasing stability and minimizing fatigue. A tuned mass vibration absorber was installed to absorb the 2/rev in-plane vibrations in the rotating frame.

8.2.1 Elastomeric Bearing

In the *Wyvern* rotor system, all flap, lag, and torsional loads—together with the centrifugal, lift, and drag forces generated by the blade are carried through the blade grip into a spherical elastomeric bearing (Figure 8.3. This bearing, inspired by LORD-type constructions, consists of alternating thin metallic shims and high-damping elastomer layers. The laminated construction greatly increases the stiffness of the elastomeric structure in the direction normal to the laminations, while maintaining virtually the same deflection characteristics in the plane of the laminates as would be found in a solid block of rubber [40]. This allows laminated elastomeric bearings to support high loads while permitting the degree of motion necessary in rotor system components. Consequently, the bearing provides fully articulated flap-lag-torsion freedom

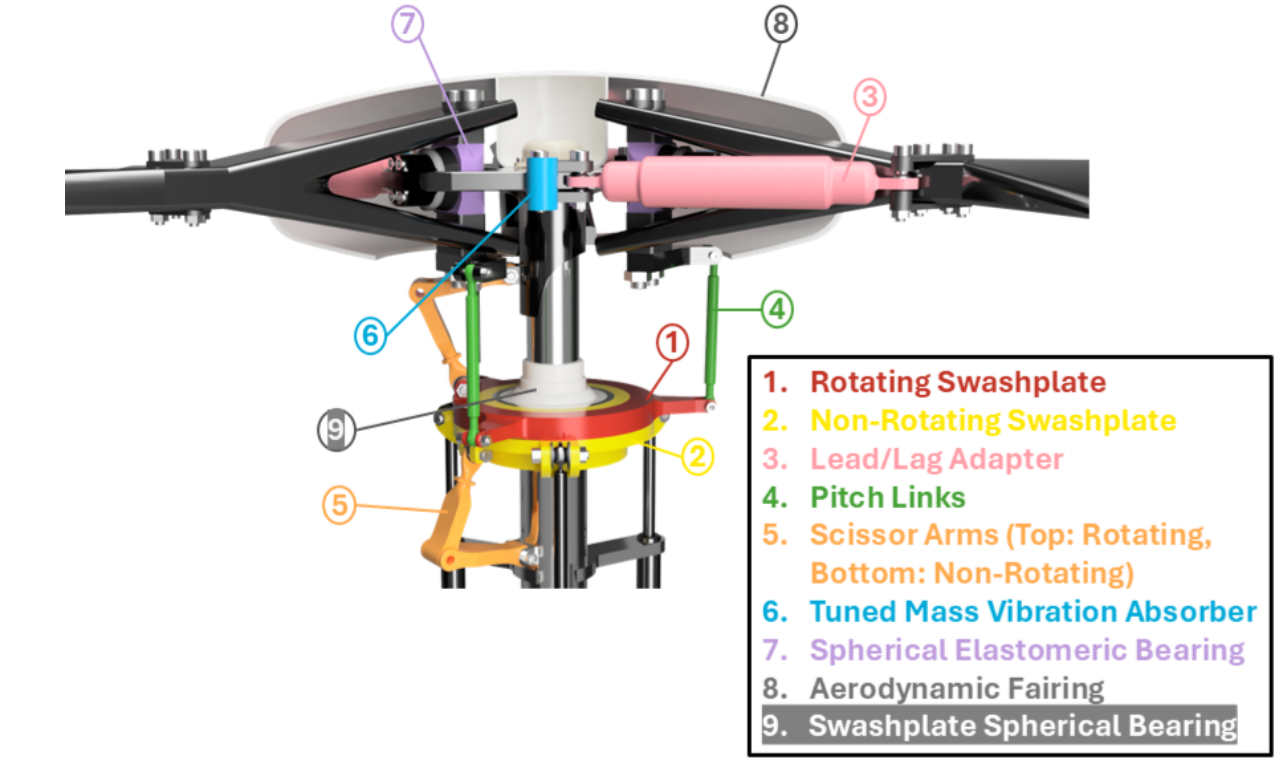

Figure 8.1: Articulated rotor hub assembly

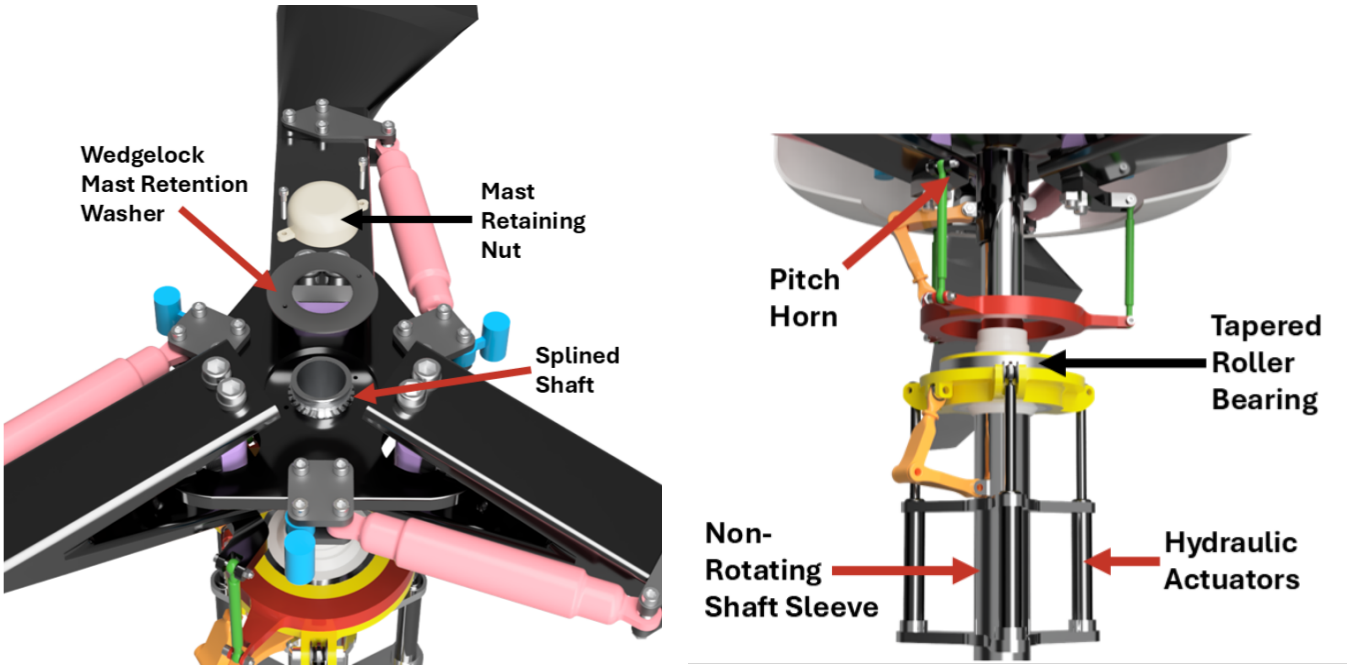

(a) Exploded view of the rotor hub attachment

(b) Swashplate exploded view

Figure 8.2: Rotor hub and swashplate exploded views

at approximately 3.1% span, eliminating the need for separate mechanical hinges and greatly simplifying the hub while maintaining the necessary stress resistance across the operating envelope. Finally, the elastomeric bearing was also chosen due its significantly reduced required maintenace in comparison to other systems.

8.2.2 Pitch Link and Pitch Horn

The pitch-horn is bolted to the bottom blade fork, which is directly connected to the main nut attaching the blade and the elastomeric bearing. It also carries an integral ball joint that mates with the pitch link. It experiences the pitching moments as bending stresses and transmits these loads axially into the pitch link. The horn sits exactly at the flap hinge (3.1%) far enough to clear the swashplate yet close enough to preserve blade torsional stiffness. Offsetting the ball-joint centre by 96 mm (3.8 in) radially outboard of the attachment to the blade allows the link to provide 1° blade pitch with 1.67 mm (0.066 in) stroke of the pitch link, accordingly from the hydraulic actuators. The blade can experience up to 23° of pitch from its nominal position before the pitch horn contacts the hub.

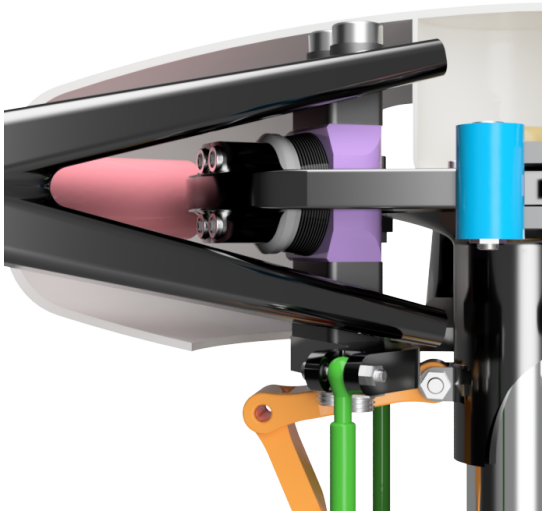

Figure 8.3: Closeup of elastomeric bearing

The length and diameter of the pitch links were computed based on two design considerations. First, to minimize bending loads, a constraint was placed on the maximum allowable angular deviation from the vertical. This angle, in conjunction with the chordwise offset of the pitch horn from the pitching axis and the maximum pitch deflection, was used to calculate the required pitch link length. Second, the pitch link diameter was sized based on the maximum loads experienced during operation, calculated using UMARC–II, accounting for three critical failure modes: pure axial loading, axial loading with superimposed bending stresses, and column buckling. Due to the critical nature of this component, a conservative safety factor of 5 was applied during the sizing process. Two candidate materials were evaluated: aerospace-grade stainless steel and Grade 5 titanium. Although titanium offered comparable strength with a lower weight, stainless steel was selected due to its significantly lower cost and ease of manufacturing, while still satisfying the stringent safety and performance requirements.

8.2.3 Lead-Lag Frequency Adapter

The soft-in-plane articulated rotor necessitates a lead-lag adapter to adjust the 1st lead-lag frequency to avoid ground resonance. It is accomplished by increasing the stiffness of the in-plane motion in the rotating frame, to reduce the regressive lag frequency. This avoids the frequency coalescence with the fuselage support roll mode, mitigating the ground resonance. The rotor 1st lag was calculated to be 0.27/rev from the blade-only structural properties, which was raised to 0.49/rev via an elastomeric rubber-made lead-lag adapter of linear stiffness of 104 daN/mm (5.9 kpi). The linear stiffness has been computed by the required angular stiffness at the lag bearing, and the adapter lever distance from the bearing of 120 mm (4.7 in). The adapter is connected to the adapter bearing in the hub to the blade fork initiation point at $0.1R$. It is subjected to compressive forces from lead-lag motion, which provides the necessary stiffness and damping. The adapter is placed close to the rotor mast, maintaining a compact hub design for an aerodynamically cleaner hub fairing, also maintaining enough moment arm relative to the lag bearing and enhancing the effectiveness of the system.

8.2.4 Tuned Mass Vibration Absorber

To mitigate transmission of in-plane vibratory loads from the rotor to the airframe, *Wyvern* incorporates a tuned mass vibration absorber (TMVA) mounted on the main rotor hub, specifically tuned to the dominant

2/rev in-plane vibratory mode in the rotating frame, contributing to 3/rev fixed-frame vibrations. Using simulated hub force harmonics from UMARC–II, the absorber was designed to target the peak vibratory mode contributing to a calculated 3/rev cabin g-level of 0.05 g at the transition flight condition. Hence, a provision of the TMVA has been made considering the flight test scenario. The TMVA, consisting of a tuned mass system mounted radially on the hub spider, effectively reduces transmission of in-plane oscillations to the mast by imposing destructive interference at the tuned frequency. This passive damping approach improves passenger comfort, reduces crew fatigue, and limits vibratory loading on PEMFC, battery, H2 tanks, avionics, and structural components, without adding active control complexity to the articulated hub architecture.

8.3 Swashplate Design

For *Wyvern*, a thorough evaluation of control actuation architectures was conducted to identify a solution that balances performance, reliability, and weight efficiency for its mission profile. Advanced swashplateless concepts, such as torsionally flexible blades with trailing edge flaps [41] or blade twist control [42] through higher harmonic control, were considered due to their potential to reduce hub drag and weight. However, these methods require exorbitant weight overhead, exceptionally low torsional frequencies, which compromise aeroelastic stability, and thus remain at low technology readiness levels. Individual Blade Control (IBC) systems, including both piezoceramic actuators and hydraulic mechanisms, were also examined for their promise in enhanced vibration control. The use of IBC utilizing hydraulic actuators requires a high actuation rate to provide adequate torque to counter the pitching moment generated by each blade. Yet, these systems demand complex high-frequency actuation within the rotating frame, resulting in bulky, heavy power conditioning or redundant hydraulic support systems, unfavorable for *Wyvern* weight-sensitive design. Given these constraints, *Wyvern* adopts a conventional swashplate mechanism.

8.3.1 Swashplate Architecture

The swashplate architecture for *Wyvern* was designed to ensure precise control while maintaining a compact, low-drag profile. The swashplate assembly is mounted atop a static mast and supported by an integrated aluminum sleeve that runs along the rotor shaft. A spherical bearing encircles the sleeve, separated by a low-friction, steel-coated Kevlar liner to allow smooth articulation in the collective and cyclic axes. The non-rotating swashplate is attached to the spherical bearing and constrained from rotating by a scissor linkage fixed to a lower shaft collar, thereby minimizing bending loads on the hydraulic actuators. A tapered roller bearing connects the non-rotating and rotating swashplates, enabling relative rotation while efficiently transmitting pitch link loads. The rotating swashplate is split into upper and lower halves that clamp around the roller bearing, and a rotating scissor linkage connects it to the shaft via splines and a splined collar to transmit torque. To maintain aerodynamic efficiency, all components—swashplate discs, scissor linkages, and pitch links—are positioned close to the shaft axis, allowing the entire mechanism to fit within the streamlined pylon and hubcap fairing.

UMARC–II hover predictions were used to estimate the pitch link loads in hover, exhibited on the rotating swashplate. Figure 8.4 shows the 3D stress and displacement analysis of the swashplate in Hover made in Catia v5. The design has a safety factor of 6 and deflections of below 5 mm (0.2 in).

8.3.2 Hydraulic Actuation System

The hydraulic control system in *Wyvern* is a closed-loop, main rotor gearbox-driven architecture designed to provide precise, low-force control inputs to the swashplate for both cyclic and collective axes. Drawing inspiration from the R44 system [43], it employs a lightweight, single-stage, positive-displacement hydraulic

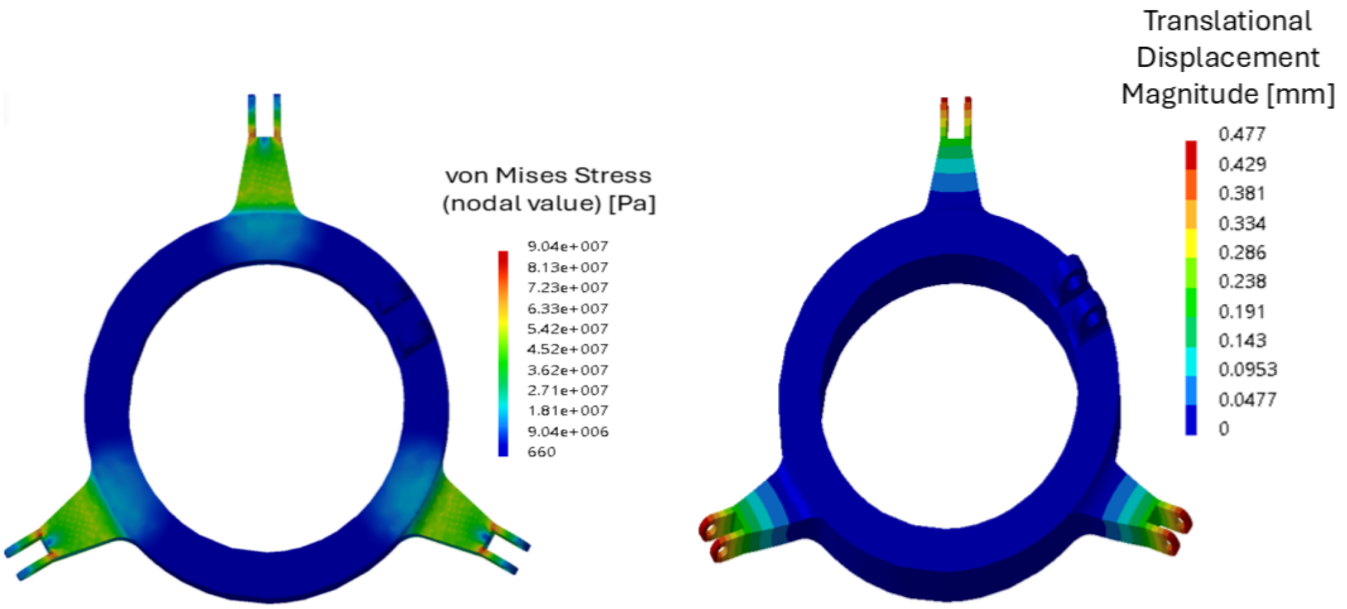

(a) von Mises stress analysis

(b) Translational displacement analysis

Figure 8.4: FEA results of *Wyvern*'s swashplate under hover pitch link loads

pump mounted on the output drive of the main gearbox. This pump delivers A257-15 hydraulic fluid at nominal pressures of 34.5 bar (500 psi) to a dedicated aluminum 1-liter (34 oz.). hydraulic fluid reservoir equipped with a sight gauge and internal baffle to prevent fluid aeration during dynamic maneuvers. Fluid is routed through flexible, high-pressure Teflon-lined stainless steel hoses to a set of three hydraulic servos—two for cyclic control and one for collective input—mounted directly beneath the non-rotating swashplate. Each servo features an internal pressure relief and bypass valve, enabling continued mechanical control in the event of hydraulic failure (system pressure below 5.5 bar (80 psi)). Servo arms are connected to the control rods via spherical rod-end bearings to accommodate multi-axis articulation and reduce backlash. Hydraulic return lines route back through the mast to the reservoir, maintaining a low-profile system footprint for aerodynamic integration within the rotor pylon.

9 Wing Design

Wyvern prioritizes loiter endurance with very high L/D, making a fixed-wing design crucial. However, they introduce other penalties- hover download, added weight, shaft-tilt constraints, and integration challenges like lift-sharing, flutter suppression, and attachment design. Our wing design balances these factors through a comprehensive trade study optimizing L/D, structural sizing, aeroelastic stability, and attachment architecture to ensure net endurance gains without compromising safety or performance. The size constraint as stated by RFP prevents the use of a traditional planar wing. *Wyvern* adopts a compact box-wing configuration (Figure 9.1). Key tunable parameters were wing gap, stagger, chord, taper ratio, and incidence angle for each segment.

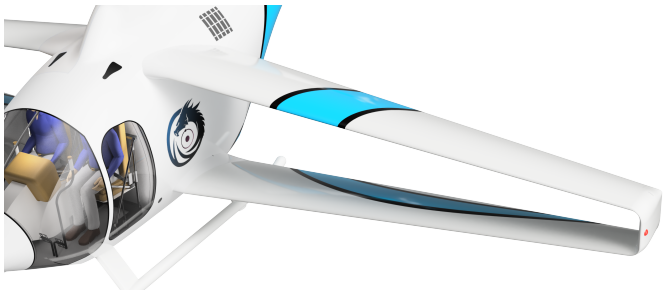

Figure 9.1: *Wyvern* box wing.

9.1 Airfoils Selection

The airfoil selection for the wing was driven by key aerodynamic goals: high L/D, gentle stall behavior, low pitching moment, broad drag bucket, and high stall Angle of Attack (AoA). An initial down selection of low-speed airfoils yielded seven candidates (Figure 9.2), prioritized for high c_l/c_d and low moment coefficients in loiter conditions. Each was evaluated via CFD using the in-house HAM2D solver [44], with results shown in Figure 9.3.

The Wortmann FX 63-120 emerged as the best, offering excellent efficiency, low drag, and moderate pitching moment. It features 12% thickness at 30.8% chord, 5.2% camber at mid-chord, and, at loiter Reynolds number and Mach number, achieves $c_{l_{\max}} = 1.97$, $(c_l/c_d)_{\max} = 72$, and stalls at 15.5°. Thus, FX 63-120 was selected for both wings, while NACA 0012 was used in the wing-connection region for its symmetric geometry and structural benefits.

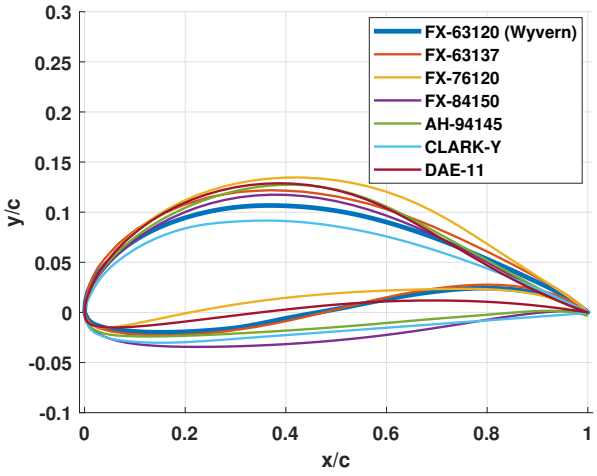

Figure 9.2: Candidate airfoils

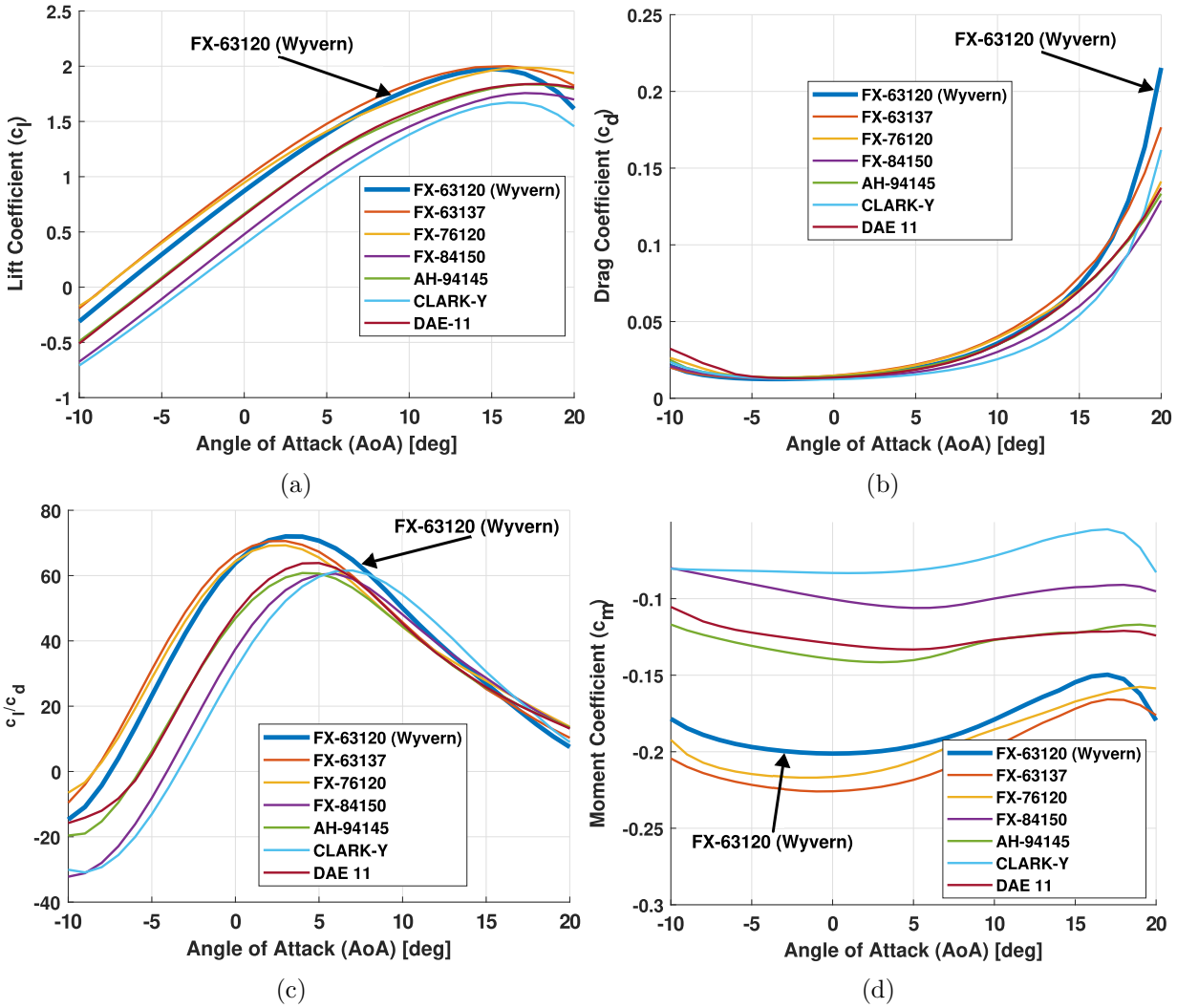

Figure 9.3: Performance curves of the selected airfoils.

9.2 Stagger and Gap

Figure 9.4 defines the key box wing parameters: stagger *st* (positive when the upper wing leads), vertical gap (distance between quarter chords), lower and upper chords (c_l, c_u), and incidence angles (θ_l, θ_u). A parametric study using the HAM2D solver (Figure 9.5) evaluated the aerodynamic impact of stagger and gap variations.

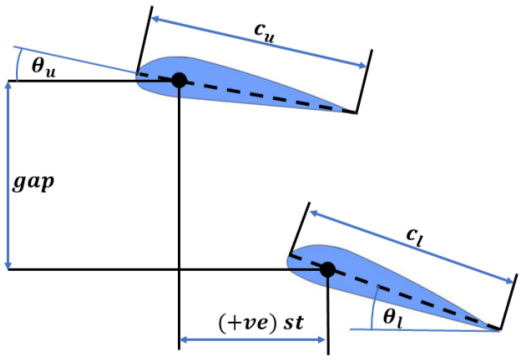

Figure 9.4: Stagger and gap.

Results showed that a positive stagger improves forward-flight lift by reducing wing interference but increases rotor download during hover. A vertical gap greater than one chord length minimized interference and enhanced efficiency. Given geometric constraints and the trade-off with hover performance, the final design adopted zero stagger and a gap slightly larger than the mean chord, prioritizing overall mission performance over marginal cruise gains.

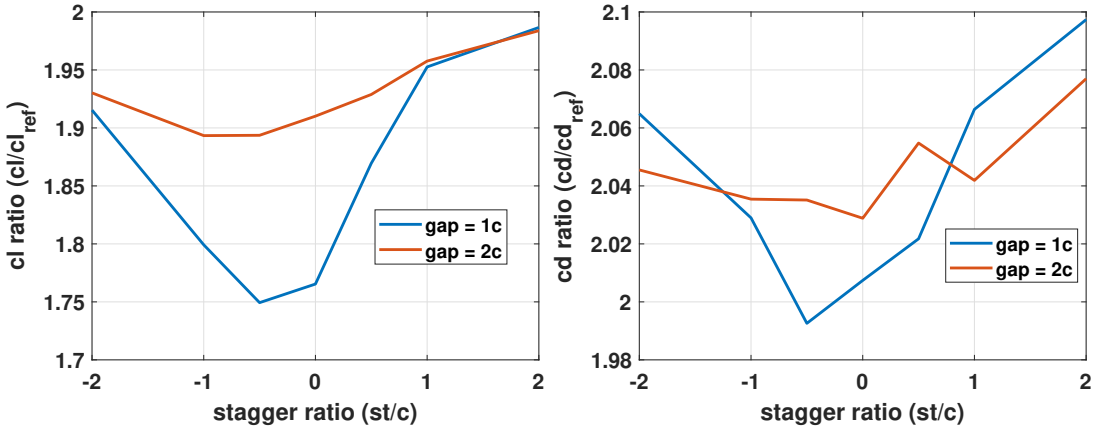

(a) Lift coefficient variation

(b) Drag coefficient variation

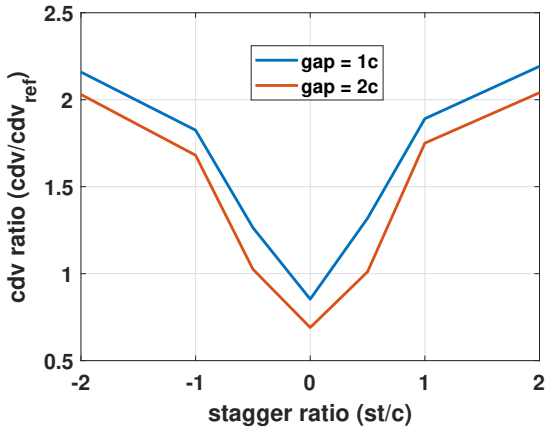

(c) cdv (Vertical drag coefficient variation)

Figure 9.5: Stagger and gap study.

9.3 Dihedral/Anhedral

To provide lateral stability and reduce aerodynamic interference, the lower wing is set to a +6° dihedral, while the upper wing has a -4° dihedral. Aerodynamically, it reduces interference between the wings by spreading the lift distribution and minimizing wake overlap. Structurally, the angled geometry allows for

more efficient load transfer through the spars, enhancing the overall rigidity and strength of the box wing system.

9.4 Taper

Both the upper and lower wings are designed with the same taper ratio of 2:1. This choice aims to mitigate any adverse effects on hover performance, particularly by minimizing additional rotor download. Moreover, tapering helps efficient spanwise lift distribution and reduces structural weight along the span, thereby decreasing the roll moment induced by the wing. To maintain geometric consistency and simplify the design, both wings share the same root chord.

9.5 Incidence

In *Wyvern* box wing, the incidence angle (with respect to the fuselage reference line) of the lower wing was increased by 1°, relative to the upper wing to reduce the interference between them and achieve equal lift share among them. This adjustment—setting the upper wing incidence $\theta_u = 8°$ and the lower wing incidence $\theta_l = 9°$. The major design parameters of the box wing are detailed in Table 9.1.

Table 9.1: Major design parameters of the box wing configuration

Parameter	**Description**	**Value**
Geometric Parameters		
L_{top}	Tip-to-tip of top wing	12 m (39.4 ft)
L_{bottom}	Tip-to-tip of bottom wing	12 m (39.4 ft)
AR_{top}	Aspect ratio of top wing	10.67
AR_{bottom}	Aspect ratio of bottom wing	10.67
b_{gap}	Mean vertical gap	0.953 m (3.13 ft)
Λ_{top}	Sweep angle of top wing	0
Λ_{bottom}	Sweep angle of bottom wing	0
Γ_{top}	Dihedral angle	-4°
Γ_{bottom}	Dihedral angle	+6°
c_{root}	Root chord (common for both wings)	1.25 m (4.1 ft)
c_{tip}	Tip chord	0.625 m (2.1 ft)
λ	Taper ratio (tip/root)	0.5
Aerodynamic Parameters		
C_L	Lift coefficient at loiter	1.1012
C_D	Drag coefficient at loiter	0.0524
L/D	Lift-to-drag ratio in loiter	17.13
α_{cruise}	Angle of attack at loiter	4.8^o
$L_{Wing}/GTOW$	Wing lift share in Loiter	55%
Structural Parameters		
Material	Wing structural material	Aluminum 7075, ±45 Carbon-fiber epoxy
Safety Factor	Structural safety margin	1.6 (under 2g loads)

9.6 CFD analysis for *Wyvern* box wing

The aerodynamic performance was assessed via CFD, using the in-house HAMSTR [44] and ANSYS-FLUENT solvers, using high-quality meshes with acceptable orthogonality, skewness, aspect ratio, and wall-normal resolution (y^+). Though mesh visualizations are omitted, quality metrics were carefully monitored

for numerical accuracy. Figure 9.6 shows velocity contours at the root and tip at V_{be}, near flat pitch. Near the root, flow fields around the upper and lower wings remain largely independent; near the tip, increased aerodynamic coupling appears, with overlapping flow regions. Despite the goal of mitigating tip vortices—reducing induced drag by 20% compared to a planar wing of equal span and area [45], streamline plots (Figure 9.7) reveal residual, though weakened, swirl flow near the tips. Pressure coefficient plots confirm both wings contribute comparably to lift. Overall, the flow remains attached, and lift distribution is balanced, affirming the drag-reduction benefits of a box wing without compromising lift.

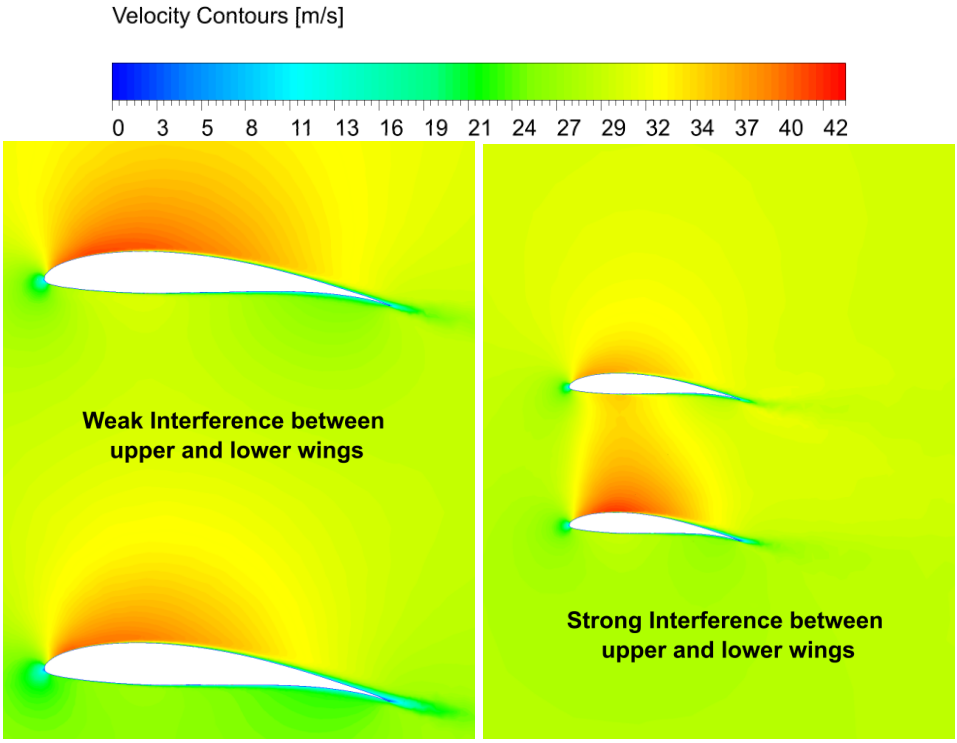

(a) Root velocity contours (b) Tip velocity contours

Figure 9.6: Velocity contours for the wing in loiter condition at the root and the tip sections.

9.7 Wing Structural Design

The wing features a separation of 1.5 m (4.9 ft) at the root and 0.6 m (2.0 ft) at the tip, resulting in a trapezoidal shape when viewed from the front. The wing incorporates two spars: one located at the quarter chord and the other at 60% chord. Based on CFD analysis of the airfoil, the quarter chord spar carries approximately 64% of the aerodynamic load, while the rear spar carries the remaining 36%. Each wing is connected to the fuselage via four hinged joints, located at the root of each spar. The box-wing layout enables the use of hinged rather than cantilevered connections, lowering the bending moments transferred to the fuselage, similar to the Airbus RACER [46]. As a result, the fuselage bulkheads and wing root structure were designed with no additional mass requirements. Further weight savings are achieved by incorporating lightening holes throughout the wing structure. Under a 2 g loading condition (four times the loiter load) the wing exhibits a maximum upward deflection of 250 mm (9.8 in) (5% wingspan).

9.8 Wing Manufacturing

Each wing consists of four aluminum I-beam spars located at the quarter chord and 60% chord, with 10 sheet-metal pressed ribs bolted to them. The spars have lightening holes machined throughout their span.

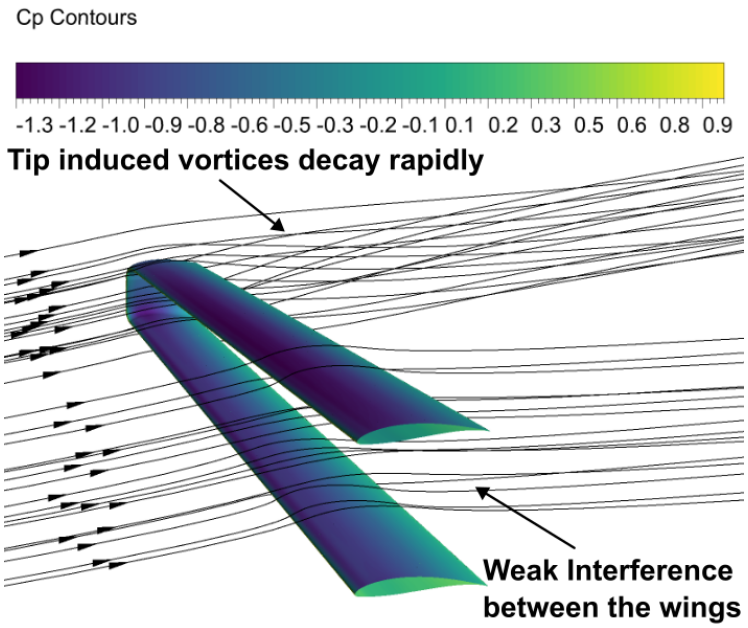

Figure 9.7: Flow streamlines for the wing in loiter condition.

Figure 9.8 shows the internal structure of the wing. The skin is a prepreg CFRP skin, composed of three

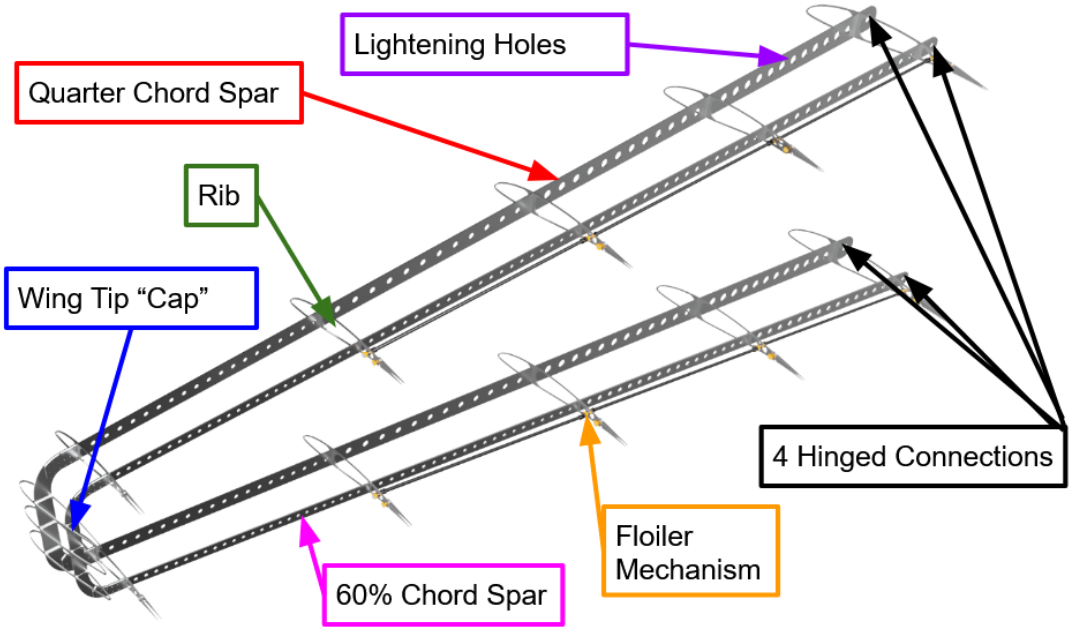

Figure 9.8: Wyvern box wing internal structure

plies of ±45° IM7 carbon fiber with a HexPly 8552 matrix. The skin is bonded over the ribs to give the necessary airfoil shape. Each wing end has a tip cap that is bolted to both the upper and lower wings. Inside this cap, the wing spars of the upper and lower wing halves are connected to their respective spars via a gusset joint. The skin of the tip cap is made up of three sections, one section for each of the bends required by the upper and lower wing, followed by a vertical section connecting these two bends to each other. The skin of the tip cap is of the same composite material as the rest of the wing skin. The skin of the vertical section of the tip cap is bonded to the tip cap skeleton, while the skin at the bends is screwed into the wing skin. The connections to the fuselage are facilitated by four hinged connections to the bulkheads

immediately fore and aft of the main rotor shaft.

9.9 Finite Element Analysis

A finite element analysis (FEA) was performed in CATIA on the wing structure under a 2g load condition. The aerodynamic load distribution was based on the results of the preceding CFD study, applying a 64/36 load split between the front and rear spars. Spanwise lift distribution was also applied following the CFD-derived profile. The simulation results (Figures 9.9) indicate that peak stress concentrations occur near the wing tip, which is consistent with the expected behavior of a hinged box-wing configuration. The maximum stress concentration was observed at the bottom edge of the upper wing quarter chord spar, reaching 320 MPa. This corresponds to a minimum safety factor of 1.6 relative to the yield strength of 7075 aluminum, the material used for the primary wing spars. Notably, the wing tip cap experienced slightly elevated stress levels, approaching the yield limit of the material. To address this localized overstress, riveted gusset plates were introduced as the interface between the tip cap and the main wing spars to improve load distribution.

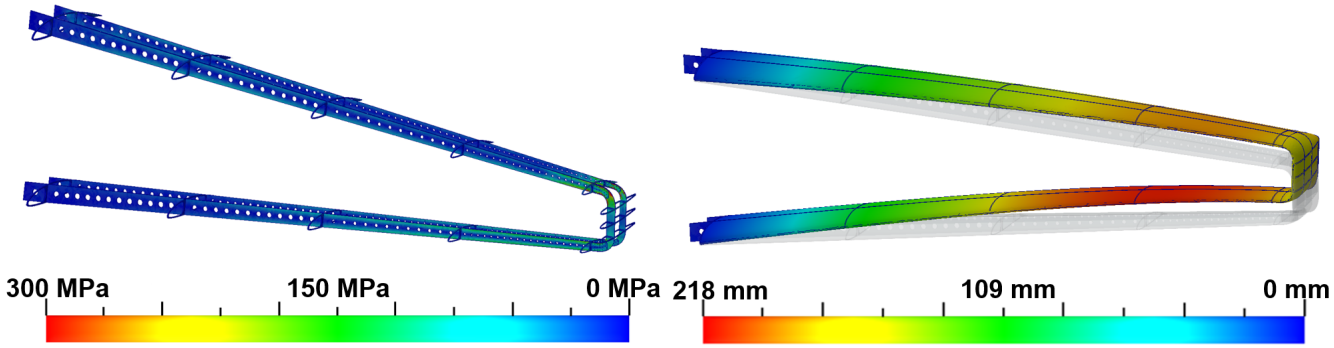

(a) Box wing stress distribution.

(b) Box wing displacement distribution with skin on.

Figure 9.9: Wing FEA under 2g loads

9.10 Aeroelastic Flutter Analysis

The closed-section architecture of a box wing yields exceptionally high torsional stiffness — its first torsion eigen-frequency 38.59 Hz is already more than eight times the fundamental bending mode at 4.38 Hz - so coupling is intrinsically weak by design. To quantify the margin, an equivalent 2-DOF bending-torsion system was extracted from the FEM results by applying transverse force and pitching moment at 75% span, and calculating the resulting deflections to find bending and torsional spring constants. These modal masses, stiffnesses, and frequencies were fed into a determinant-expansion (p-k) flutter solution [47], to clear it from flutter up to transonic Mach numbers.

9.11 Floiler

9.11.1 Lift Reduction Mechanism Selection

A steep descent in autorotation, as required in mission segment 7, is difficult with the current box wing due to two main factors: adverse roll disturbances due to detached wing flow at high angle of attack and rapid rotor RPM decay from upward flow being disturbed by the wing before reaching the rotor [48]. To address this, the box wing is modified with a **floiler**—a trailing-edge flap that acts as both a flap and a spoiler. Upward deflection reduces lift during descent by decreasing effective camber; downward deflection in hover reduces downwash, improving performance. As shown in Figure 9.10(b), upward floiler deployment reduces flow separation, cutting drag by 40% and lift by 70%.

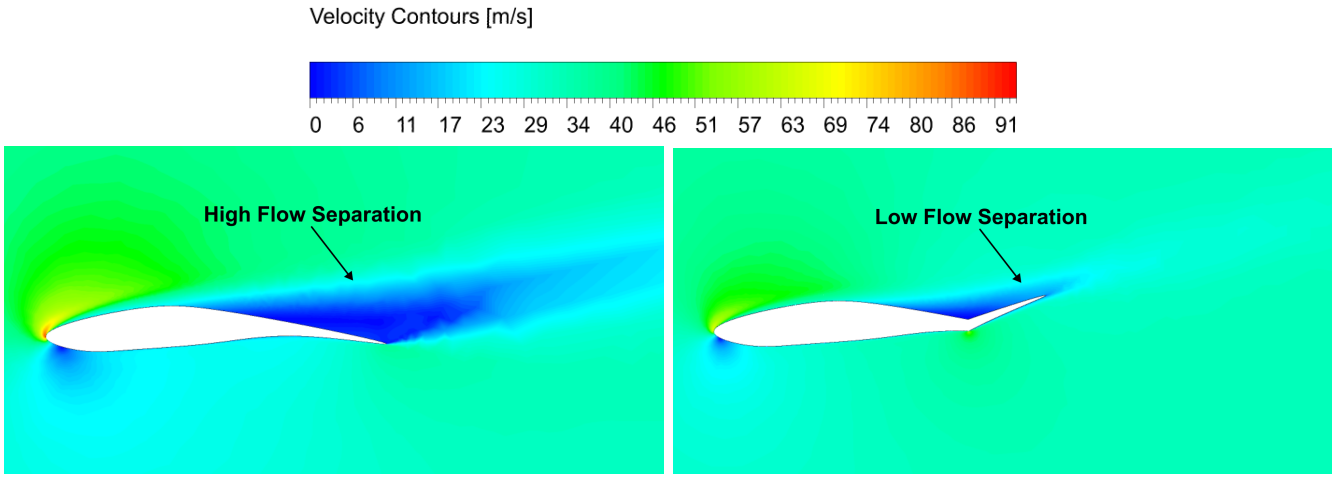

(a) Clean airfoil (b) Floiler deployed upward

Figure 9.10: Clean airfoil vs floiler deployed upward during steep descent

Hence, the roles of the floiler in *Wyvern* configuration are twofold: (i) to reduce the wing lift during the steep descent phase; 70% reduction in lift when deployed upward in descent and (ii) to decrease the download in the hover phase of flight; 15% reduction in vertical drag when deployed downward in hover.

9.11.2 Floiler Mechanism

The floiler is installed for the upper and lower wings through the entire span. The floiler is comprised of a set of ribs that pivot about hinges located at 75% of each wing rib and are covered by the same type of composite skin as the wing. The floiler ribs are additionally secured to a gear that is connected to another gear (located inside the wing) via a chain. The gear, which is inside the wing (Figure 9.11) is fitted onto a torque tube that spans from the root of the wing to the fourth outboard wing rib. The rotation of the torque tube translates into a rotation of the floiler in the same direction. The floiler can be deflected 30° upwards during the descent phase and 67° downwards during the hover phase (Figures 9.12). The simplex hydraulics present in the aircraft are used to actuate the servo for this movement. As this is a safety-critical feature, the control was made redundant via an additional control lever in the cockpit, which could be manually controlled in case of hydraulic failure.

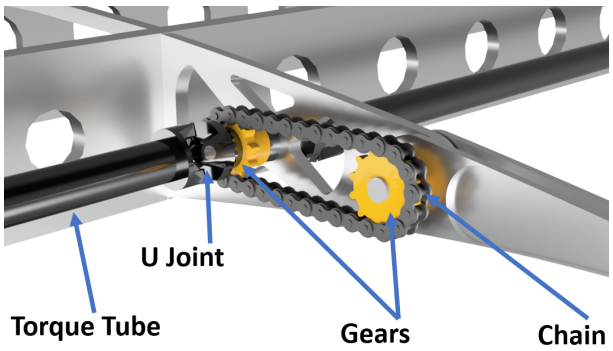

Figure 9.11: Floiler mechanism closeup

10 Tail Rotor Design

Although the RFP assumes no-wind conditions, certification standards (CS-27) require helicopters to remain controllable in crosswinds up to 31 km/h (17 knots) from all azimuths. This presents a critical design challenge for the tail rotor, particularly in avoiding vortex ring state (VRS), which can lead to loss of tail rotor effectiveness (LTE). To address these challenges, the design process resulted in an optimized two-bladed teetering tail rotor with twisted blades. The initial design is developed in the early part of this chapter and later optimized using the same algorithm (in Chapter 6) applied to the main rotor.

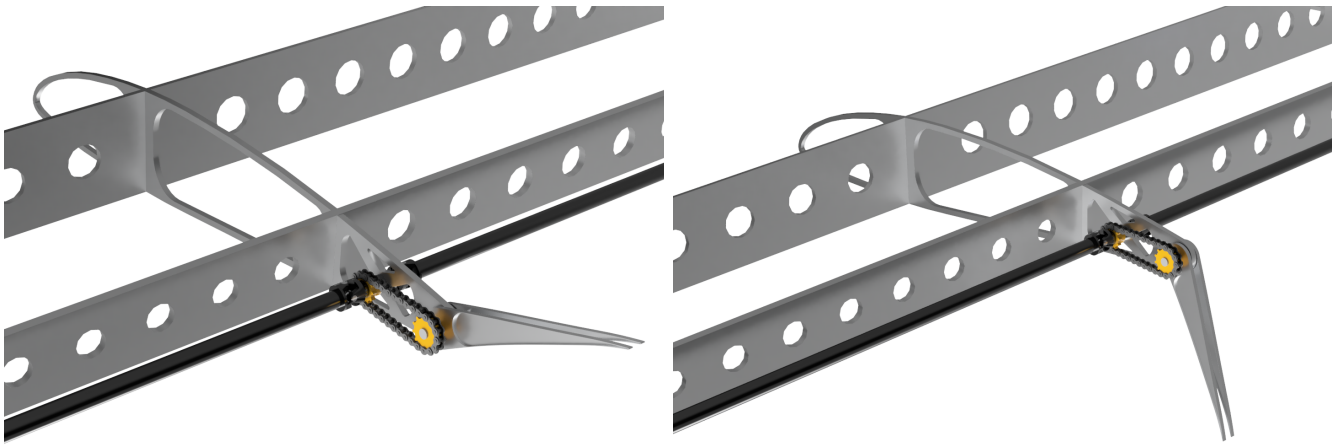

(a) 30° Upward deflection.

(b) 67° Downward deflection.

Figure 9.12: Floiler deflection positions

10.1 Tail Rotor Sizing

The primary design drivers for the tail rotor were the avoidance of loss of tail rotor effectiveness (LTE), the minimization of weight, and low power in hover, while ensuring sufficient anti-torque and yaw control across all flight segments. The design process utilized momentum theory and the AFDD tail rotor weight estimation model [23]. The most demanding torque and yaw control requirements were identified during vertical climb and descent segments, where rotor power and torque demands peak.

10.1.1 Diameter

Certain crosswind directions worsen the risk of LTE. A crosswind from 90° forces the tail rotor into a climbing flight regime, requiring increased collective pitch to maintain thrust [49]. This raises blade loading and increases the risk of blade stall. Conversely, a crosswind from 270° directly opposes the tail rotor inflow, potentially inducing VRS and leading to LTE [50]. Figure 10.1 shows how the radius of the tail rotor varies due to crosswind from 270° azimuth. They are inversely proportional that as the required wind velocity from 270° increases, the radius decreases. Thus, a smaller rotor diameter is desired to avoid VRS. However, a smaller rotor radius requires more power consumption and higher blade loading. The crosswind condition and optimization of power consumption and blade loading are explained in more detail in the later section. The selected radius is 0.9 m (2.95 ft), providing a 10% margin of the maximum cross wind speed.

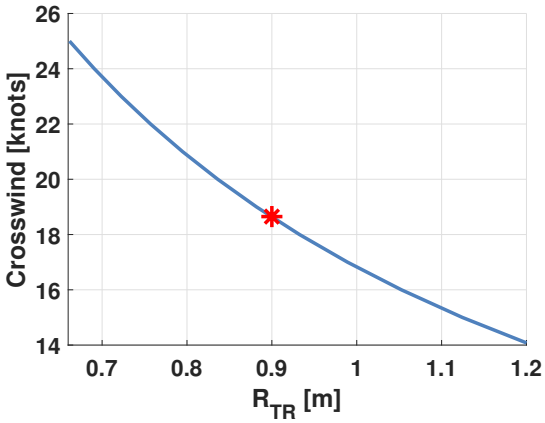

Figure 10.1: Tail rotor radius requirement with crosswind

10.1.2 Number of Blades and Solidity

Figure 10.2 illustrates the impact of tail rotor solidity on blade loading and rotor weight. An interesting observation is that, for a given solidity, tail rotor weight generally increases with the number of blades, except in the case of the 2-bladed rotor, which is the lightest configuration. This exception arises because

the two-bladed rotor uses a teetering hub, whereas configurations with three or more blades use articulated hubs. A key factor influencing the rotor weight in this context is the flapping frequency, which is directly proportional to the weight in the AFDD weight model. The teetering rotor exhibits a (cyclic) flapping frequency of 1/rev, significantly lower than that of articulated rotors, leading to a reduced structural requirement and, consequently, lower weight. Since minimizing weight is a primary design objective, the 2-bladed teetering rotor with a solidity of 0.1 is selected. This configuration provides adequate stall margin and ensures sufficient yaw control authority while maintaining the lightest possible rotor system.

10.1.3 Tip Speed

The tail rotor rotational speed is governed by the main rotor rotational speed, as both are mechanically linked through the drivetrain. A lower tail rotor tip speed helps minimize aerodynamic noise and compressibility effects, which are particularly important in urban or noise-sensitive operations. However, operating at a lower tip speed increases the torque demand on the tail rotor, necessitating a heavier and more robust tail gearbox to handle the added mechanical loads [51]. The design target is to reduce the weight as much as possible. Thus, tip speed is set equal to the tip speed of the main rotor for mechanical simplicity, which minimizes the weight. In hover, 182 m/s (597 ft/s) tail rotor tip speed corresponds to the RPM of 1931. This is comparable to the driveshaft RPM of 2436. Consequently, only minimal gearbox reduction (1.27:1) is required, thereby reducing the overall weight needed to achieve the proper tail rotor speed.

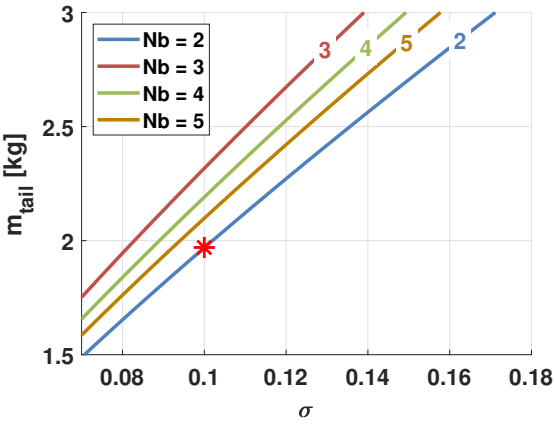

Figure 10.2: Tail rotor mass versus solidity

10.2 Tail Rotor Aerodynamic Optimization

The design optimization of the tail rotor follows a similar methodology as that of the main rotor blade, but with fewer design variables. There are two design variables for the tail rotor, making the optimization process simpler. A linear twist and airfoil selection along the span are two design variables. A constrained optimization was done using genetic algorithms to maximize FM at hover. A baseline tail rotor is designed with a linear twist of $-8°$ with NACA23012 along the span with an aspect ratio of 5, and C_T/σ of 0.1. The comparison of the performance of the baseline and optimized rotor is presented in Table 10.1. Figure 10.3 shows the improvement of the FM of the tail rotor with generations. The optimized tail rotor parameters are presented in Table 10.2. The planform of the tail rotor is presented in Figure 10.4.

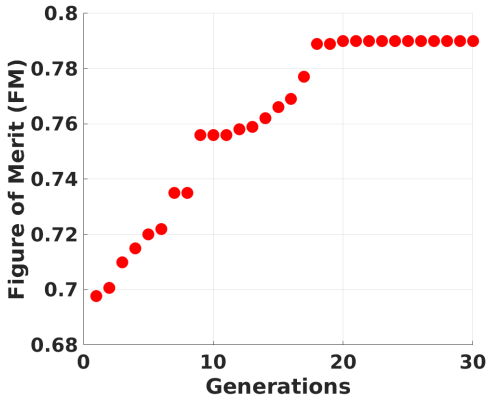

Figure 10.3: Tail rotor FM across generations

Table 10.1: Baseline vs. optimized tail rotors

Metric	Baseline	Optimized
Figure of Merit (FM)	0.74	0.79
PL (N/kW)(lb/hp)	49 (8.14)	54 (8.97)
Power (kW)(hp)	40 (54)	25 (34)

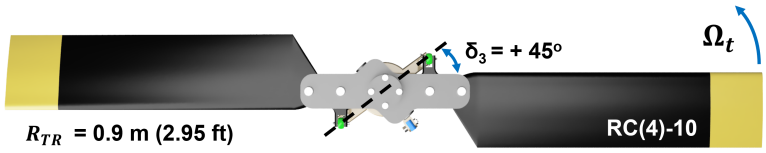

Figure 10.4: Tail rotor planform

Table 10.2: Tail rotor parameters

Parameter	Value
Diameter	0.9 m (2.95 ft)
Number of Blades	2
Solidity	0.1
Aspect Ratio	5
Moment Arm, l_t	6 m (19.7 ft)
Tip Velocity	182 m/s (597 ft/s)
Airfoil	RC(4)-10
Twist	$-8°$

10.3 Tail Rotor Mounting

With the special requirement of dimension limit, the tail rotor is mounted where it gives enough clearance between the main rotor and the dimension limit so that it gives the maximum anti-torque with the lowest possible power consumption. Thus, it gives 6 m (19.7 ft) of moment arm. Two mounting positions for the tail rotor were considered: (1) on the vertical stabilizer, (2) on the tail boom. Mounting the tail rotor on the vertical stabilizer offers the advantage of increased ground clearance, enhancing safety for the ground crew. Additionally, this placement reduces the trimmed body roll angle from -2.21° to -1.62°, where the tail rotor lies in the same plane as the main rotor. However, this configuration requires a more complex transmission system and a structurally reinforced vertical stabilizer, leading to an increase in overall weight.

In contrast, mounting the tail rotor on the tail boom reduces system weight by allowing a simpler transmission layout and eliminating the need for significant structural reinforcement of the vertical stabilizer. While this option results in a slightly higher trimmed body roll angle, it remains within acceptable limits for the intended flight envelope, as the aircraft is not designed for extreme operational conditions. To further minimize aerodynamic blockage from the tail boom, a root cutout is implemented. Given that minimizing weight is a primary design objective, the tail rotor is mounted on the tail boom.

A pusher-type tail rotor is selected, where the rotor wake is directed away from the vertical stabilizer. Experimental results have shown that pusher configurations require less power to produce the same thrust compared to tractor configurations [52]. The rotor is configured to rotate in an forward-at-the-top direction. This is selected due to the mechanical simplicity of the tail rotor transmission to minimize the weight.

10.4 Tail Rotor Hub Design

Wyvern employs a two-bladed teetering tail rotor, utilizing composite materials for the blades and aluminum 7075 for the hub yoke to minimize structural weight. The teetering configuration was selected for its mechanical simplicity, high technology readiness level, proven by its widespread use in existing helicopters, and inherently low weight. The tail rotor design, shown in Figure 10.5, draws inspiration from the established Robinson R22 teetering hub design [53]. Each blade is mounted between the upper and lower yoke plates via two radially spaced spherical bearings at the root. Pitch horns are built into the composite blades and enable pitch articulation about these bearings, providing a ±11° range.

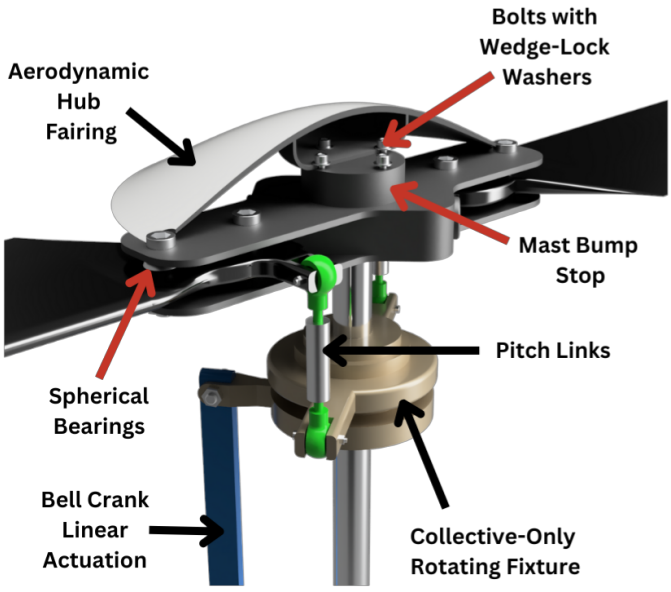

Figure 10.5: Tail rotor hub components

Pitch control is achieved through pitch links connected to a collective-only rotating fixture. A streamlined hub fairing reduces tail rotor drag in forward flight. The hub yoke is fastened to the tail rotor shaft using bolts and wedge-lock washers. To prevent potential damage from mast bumping, the interior of the hub yoke is lined with rubber.

A built-in δ_3 angle of 45° provides stabilizing pitch-flap coupling and reduces flapping in absence of a swashplate. When blades flap upward, their pitch decreases, increasing effective flap stiffness and helping limit excessive flapping that could lead to mast bumping or blade-fuselage contact [54]. This coupling also reduces loads on the blades and pitch links.

11 Airframe Design

Wyvern's internal structure and components were designed to withstand flight loads of +3.5g/-1.0g [55]. The effects of heavy-weight components on CG position, connections between all of the hydrogen propulsion system components, as well as ease of access to them for refueling and maintenance, were major design considerations. The landing gear was designed to aid passengers in seating in the cockpit, while maintaining a low drag profile, weight, and providing good ground stability.

11.1 Internal Layout

The internal layout of *Wyvern* is the result of decisions intended to achieve optimal vehicle CG position throughout the mission, minimizing the length of associated fuel and coolant pipelines and electrical connections. The low-weight transmission and powertrain are arranged to allow for swashplate actuation, tail transmission structural support. The fuselage mid-section houses the hydrogen propulsion components and serves as a mounting point for the box wings. The placement of the hydrogen propulsion system components was done with the heaviest components being placed closest to the main rotor shaft. Stacking the propulsion components vertically allowed the lowest vehicle footprint. The 1.88 m^2 (20 ft^2) cockpit features large windows for ease of observation during the mission as well as a nose payload bay for light cargo. The fuselage bulkheads and longerons were then built around these components, adding reinforcements where needed. The internal layout is detailed on the next page.

11.2 Fuselage Structure

The airframe is a semi-monocoque structure made up of 9 bulkheads connected by longerons, for load distribution, with two keel beams from the nose to the tail. The bulkheads ahead of the rotor support part of the gearbox, H_2 tanks, PEMFC stack as well as the cockpit, payload, and major electrical components. The bulkheads aft of the main rotor provide the other support for the gearbox, hydrogen tanks, PEMFC stack, as well as the radiators and tail boom.

11.2.1 Load Paths

Rotor loads are transmitted to the airframe through the lift rods. The lift rods are connected between the top of the main rotor standpipe and the bulkheads immediately forward and aft of the main rotor via machined brackets installed on the bulkheads. The primary rotor load paths are highlighted in Figure 11.1. The red arrows represent the directions of diffusion of main rotor loads and wing loads into the airframe. Wing loads are passed to the airframe via a set of machined brackets located on the same bulkheads that are connected to the lift rods. The wing, hydrogen tanks and PEMFC contribute significant loads during flight, and their load paths are shown in Figure 11.2, with green showing wing load paths, yellow showing

Wyvern Cutaway

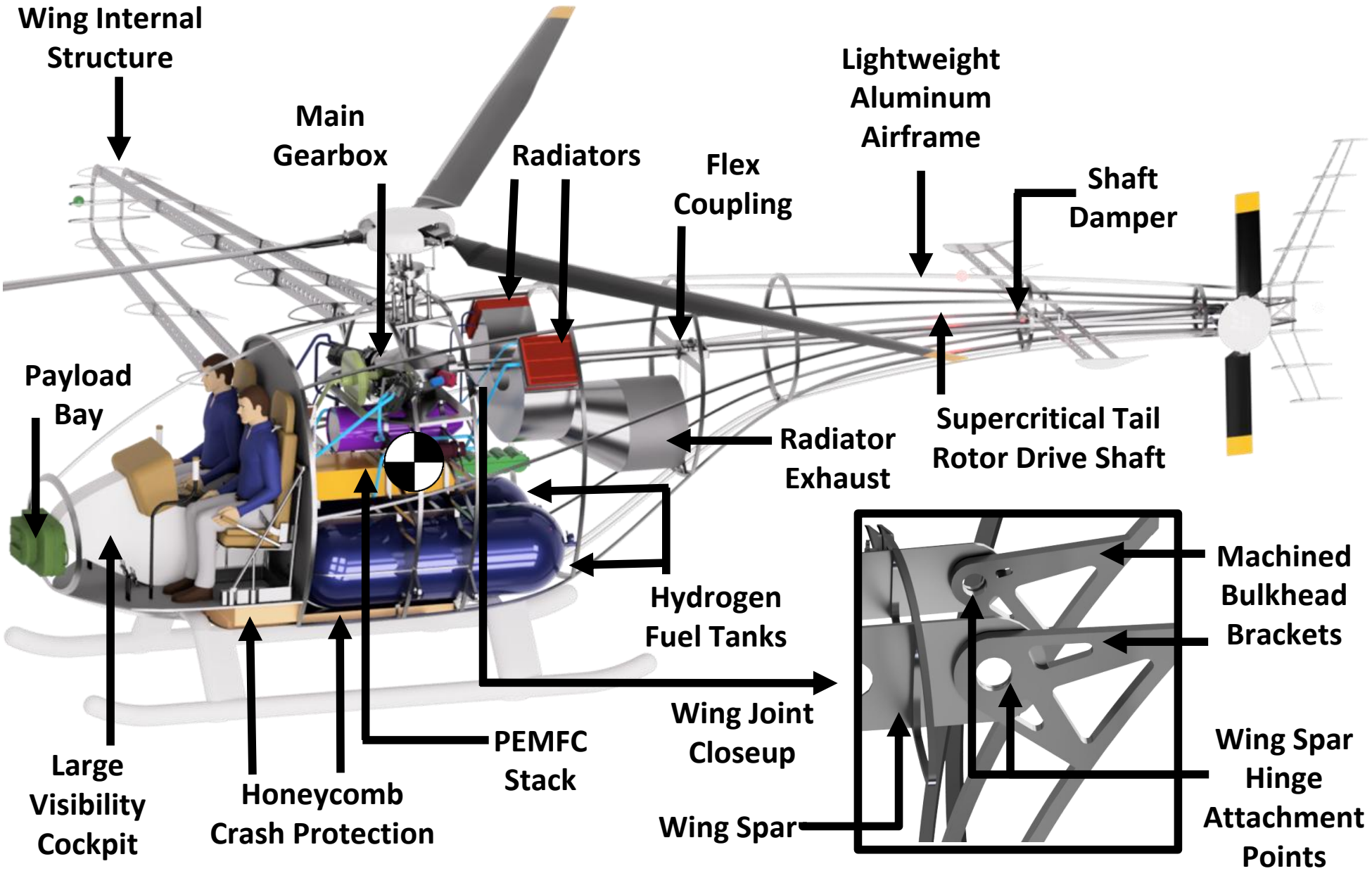

tank load paths and red showing stack load paths. During landing and taking off, the ground reaction loads are transmitted through the bulkhead separating the cockpit from the rest of the airframe and through the bulkhead immediately before the tail boom, which have been sized to sustain 2.2 g ground reaction loads.

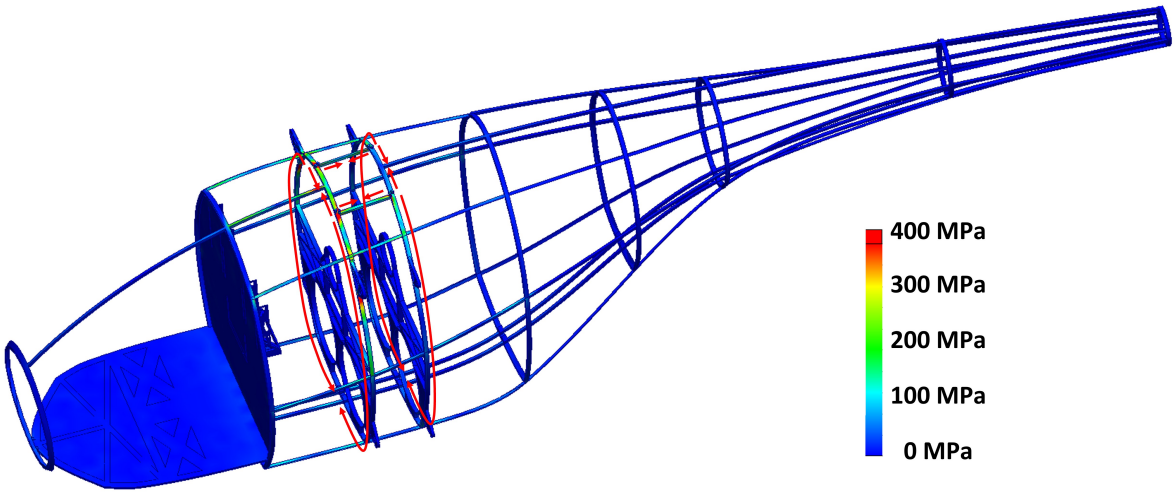

Figure 11.1: Airframe stress under 3.5 g loading with rotor load paths

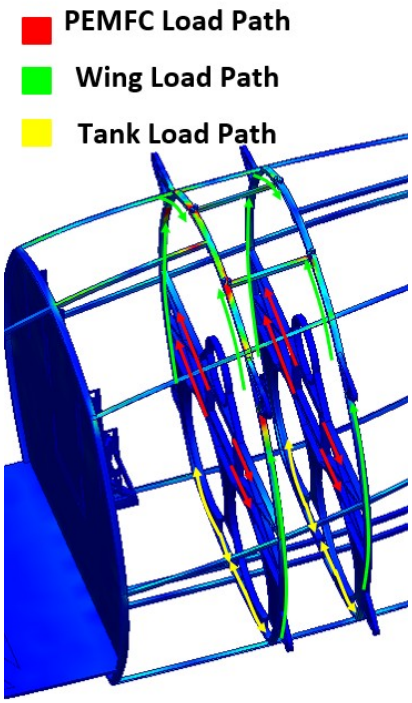

Figure 11.2: Wing, hydrogen tank, and PEMFC load paths

11.2.2 Airframe Material Selection

Wyvern bulkheads, longerons, landing gear, as well as internal component support structures, are made of 7075 Aluminum. A prepreg carbon-fiber reinforced polymer (CFRP) skin, composed of three plies of ±45° IM7 carbon fiber with a HexPly 8552 matrix, is bonded to the airframe structure [56].

11.3 Lift Rod Design

The lift rods serve the function of load transfer from the main rotor shaft to the bulkheads. The rods were sized to handle rotor loads at the maximum loading condition of 3.5g with a factor of safety of 2. A hollow cross-section of inner and outer diameters 10 mm (0.39 in) and 15 mm (0.59 in), respectively, was selected over a solid rod to save weight without any effect on load-bearing capabilities. AISI 1045 steel was chosen as the lift rod material for its high tensile yield strength and high stiffness.

11.4 Empennage Design

The empennage is essential for maintaining stability and control, so its design was guided by both static and dynamic stability considerations. The horizontal and vertical stabilizers were optimized using flight dynamics simulations to ensure effective overall stability. Three empennage configurations were evaluated: T-tail, V-tail, and conventional. The T-tail offers the advantage of positioning the horizontal stabilizer away from the rotor wake, preventing additional hover download factor in both hover and forward flight. However, this design requires a structurally heavy vertical stabilizer to support the horizontal tail, which adds undesirable weight to the vehicle. The V-tail was also considered but was found to reduce stability, especially during low speeds, making it less suitable for the required low-speed loitering performance. These trade-offs, the conventional empennage was selected. This configuration provides a balanced solution, offering reliable stability and control without the structural penalties or low-speed drawbacks associated with the other options. The overall view is shown in Figure 11.3.

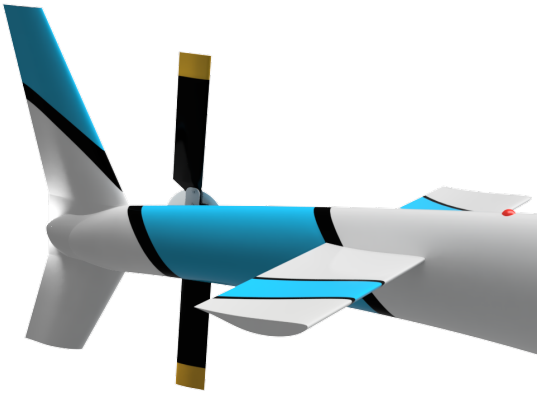

Figure 11.3: *Wyvern* empennage

11.4.1 Horizontal Stabilizer

In a conventional single main rotor (SMR) helicopters, the horizontal stabilizer primarily counters the fuselage moment. For lift-compound configuration like *Wyvern*, the horizontal stabilizer is also required to balance the pitching moment generated by the main box wing and to ensure static longitudinal stability. Due to storage dimension constraints specified in the RFP, installing the asymmetric stabilizer at the end of the tail boom where it would benefit from a maximum moment arm, was not feasible. As a result, the stabilizer was positioned inboard on the tail boom. This location was carefully chosen to avoid interaction with the main rotor wake during hover, preventing additional hover download penalties.

The DAE-11 airfoil was selected for its high lift-to-drag ratio and low pitching moment based on Figures 9.3. The stabilizer area was sized using a tail volume coefficient of 0.67, which falls within typical values for stable aircraft and ensures adequate longitudinal stability. The stabilizer is installed inverted with a 2° angle of attack to provide the necessary downward force for trim and stability. The horizontal stabilizer structure is the same as the wing, with two aluminum spars located at the quarter chord and 60% chord and three ribs on each stabilizer half. A ±45° weave composite skin is bonded to the spars and ribs. The horizontal stabilizer spars pass through the tail boom and are fixed to the tail boom via brackets machined on the tail boom bulkheads. A summary of the Horizontal and

Table 11.1: Horizontal tail properties

Parameter	Value
Area	1.30 m^2 (14 ft^2)
Span	2.5 m (8 ft)
Chord	0.5 m (1.7 ft)
Moment arm	4.2 m (14 ft)
Aspect ratio	5
Airfoil	DAE-11
Incidence angle	2°

Vertical stabilizers is provided in Table 11.1.

11.4.2 Vertical Stabilizer

Maximizing loiter time is a key mission requirement for *Wyvern*, necessitating minimal power consumption during the loiter segment. The vertical stabilizer was thus designed to offload the tail rotor by generating sufficient anti-torque force during loiter, reducing tail rotor power demands. Thus, it needed a cambered airfoil, unlike a conventional symmetric vertical stabilizer. The DAE-11 airfoil was selected for its favorable aerodynamic characteristics. To further enhance efficiency by minimizing the blockage of the tail rotor, the vertical stabilizer is mounted through the tail boom. A summary of the Horizontal and Vertical stabilizers is provided in Table 11.2.

Table 11.2: Vertical tail properties

Parameter	**Value**
Area	1.20 m^2 (13 ft^2)
Span	1.5 m (5 ft)
Chord	0.53 m (1.7 ft)
Moment arm	6 m (20 ft)
Aspect ratio	2.5
Airfoil	DAE-11
Incidence angle	2 °

11.5 Landing Gear

The landing-gear design began with a trade study comparing alternative layouts, materials, and cross-sections, then progressed to static-load analysis, always prioritizing the lightest viable structural solution and an aerodynamically efficient design.

11.5.1 Configuration Trade Study

Three landing gear configurations were considered. Each was studied using the AFDD Weight model [23] and calculated flat plate area. The study showed that the retractable skid and wheels weighed 42 kg (93 lbs) and 99 kg (217 lbs), respectively, whereas a fixed skid weighed only 32 kg (70.5 lbs). The drag area was calculated to be 0.11 m^2 (1.2 ft^2). Both the retractable systems were too heavy, and the benefit from reduced drag didn't outweigh the empty weight penalty. The fixed skid landing gear configuration offered the lightest, simplest, and most robust solution for rotorcraft, making it ideal for endurance-focused missions. With no retractable mechanisms, it reduces system complexity, weight, and maintenance requirements, while providing a wide, stable base ideal for uneven or rugged terrain. Its fixed design also minimizes the risk of failure during critical landing phases, enhancing operational safety and reliability. The overall skid landing gear design process focused on optimizing four key parameters: material selection, strut cross-section geometry, strut shape, connection design, and load distribution between the front and rear struts.

11.5.2 Landing Gear geometry

A skid-type landing gear with four attachment points was selected to minimize weight and aerodynamic drag relative to both fixed skid and retractable wheel configurations. The design prioritized low mass while ensuring ground stability and structural integrity under impact loads. Skid geometry was defined by allowable pitch and roll angles relative to the aircraft's center of mass, establishing the required skid footprint for stability. Standard conventions dictate that the tip over angles exceed 30°and the smaller (rear) pitch angle exceed 23° [57]. *Wyvern's* landing gear angles exceed both of these conventions with 40°of tip over angle and 32°of pitch angle. With the skid dimensions fixed, supporting struts were designed to meet structural requirements under CS-27.725 drop test conditions (0.33 m), using the equivalent static load method from Chernoff [58]. Al 7075 was selected as the structural material due to its favorable

strength-to-weight ratio, resulting in a 10 kg (22 lbf) weight reduction compared to a steel alternative, while only marginally increasing the flat plate drag area. An elliptical cross section was adopted for the struts to provide a compromise between the low aerodynamic drag of an airfoil profile and the structural efficiency of a circular cross section. The strut shape was defined as a straight member with rounded corners to minimize stress concentrations at both the strut-bulkhead interface and along the strut itself. Finally, a longitudinal load distribution of 80% rear/20% front was implemented, which further reduced system mass by approximately 1 kg (2.2 lbs) relative to a symmetric 50/50 load configuration.

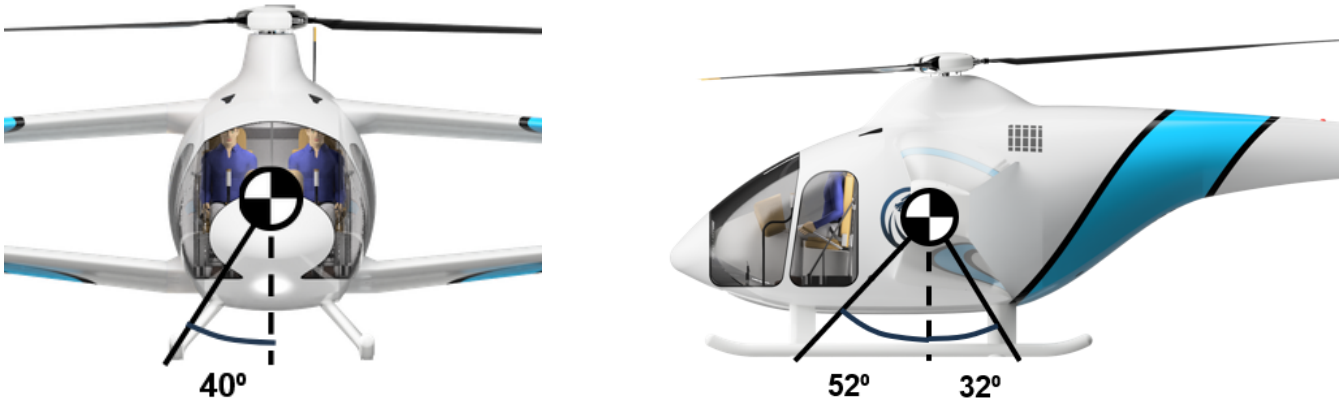

(a) Tip over angles (b) Pitch angles

Figure 11.4: Landing gear stability angles

11.5.3 Landing Gear Static Structural Analysis

A finite element analysis (FEA) study was conducted in SolidWorks to evaluate the resulting stress distribution within the structure. The loading condition of the simulation was for a drop from 0.33m (1.08 ft) as per CS-27.725 regulations. The analysis confirmed a minimum safety factor of 1.75 under these loading conditions, as shown in Figure 11.5.

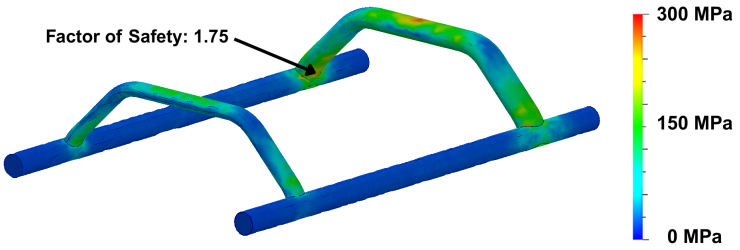

Figure 11.5: Landing gear FEA

11.6 Vehicle Crashworthiness

In the event of a hard landing or crash, energy attenuation mechanisms are essential to absorb the kinetic energy of the aircraft and minimize the risk of injury. A portion of this energy is dissipated through large plastic deformations in the landing gear, which is specifically designed to deform under high loads. For this purpose, Aluminium 7075 was selected due to its high energy absorption and good strength-to-weight ratio. However, since the mission profile occurs mainly over water, the landing gear would provide no energy dissipation benefits over such a surface in the event of a crash [57]. As a result, the design of the seats is crucial for passenger safety. Thus, *Wyvern* is equipped with inversion tube Variable-Load Energy Absorbers (VLEAs), enabling tunable energy absorption performance across various loading conditions. Special attention was given to the fuel tanks' crash survivability. With their placement

Figure 11.6: Inversion absorbers

within the vehicle, it is imperative that during a crash, their movement is limited to prevent them from piercing into the cockpit or piercing other critical components such as the PEMFC stack. As a result, a dual approach was taken: utilizing both honeycomb structures and a metallic cage.

The honeycomb mesh was designed around the geometric constraints of the vehicle as well as under the following condition: a vertical crash impulse with a velocity change of 13 m/sec (42 ft/sec) and peak acceleration of 48 g. The honeycomb is made out of a Kevlar/Nomex composite due to its very light weight, excellent compressive strength, and self-extinguishing properties. Figure 11.7(a) shows the minimum required thickness of the mesh, with *Wyvern* implementing a high safety margin. The cage is installed for retention of the tanks in the longitudinal direction while also facilitating ease of access and installation.

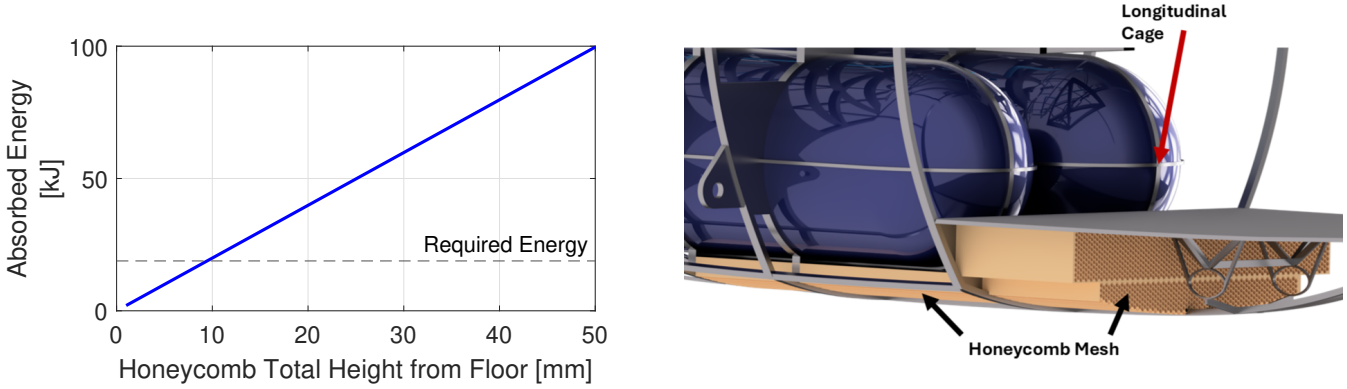

(a) Honeycomb height required for different absorbed energy in vertical crash

(b) *Wyvern*'s honeycomb mesh installed below the fuel tanks

Figure 11.7: *Wyvern*'s key tank survivability features

Finally, with *Wyvern* being a hydrogen-powered aircraft, additional safety measures were required to ensure minimum hazards related to the hydrogen fuel tanks. Pressure Relief Valves (PRV) with crash triggers were therefore installed that would open and vent the gas in the unlikely event of a crash.

12 Propulsion

Wyvern propulsion system consists of a hydrogen PEMFC and a flight battery arranged in parallel. The PEMFC is the primary power source, while the battery assists with peak power. Power sharing is achieved via dual DC/DC converters that transform the source voltage to a steady 795 volts. The architecture is based on in-house research published earlier [59, 60]. The system was designed to output a maximum continuous combined power of 277 kW (371 hp), with the PEMFC providing 210 kW (286 hp) (76% of total power). The PEMFC and balance of plant are custom designs for *Wyvern*. Hydrogen is stored in two 700 bar, 350 L (92 gallons) tanks at ambient temperature, holding a maximum of 24.8 kg (55 lbs) of fuel. The flight battery uses state-of-the-art cell technology in the form of silicon-anode Lithium-Ion cells with high energy and power density. An option for plug-in charging of the battery is provided to achieve a complete energy state before take-off.

Key Challenges

1. **Low specific power of hydrogen fuel cells**

   Although the PEMFC manufacturers may have a nominal specific power over 2 kW/kg (1.2 hp/lb),

this is dramatically reduced when accounting for packaging, air intake, humidifier, and other balance of plant components. The final PEMFC specific power can be well under 1 kWe/kg (0.6 hp/lb), where "e" stands for net electrical power. The solution is to incorporate a battery with high specific power (2-3 kW/kg) (1.2-1.8 hp/lb) to share the load during high power flight profiles. Batteries are energy limited but can provide high specific power for short durations.

2. **Determining the PEMFC operating point**

   The PEMFC operating point has a significant impact on the size of the stack required to produce a given power. Large stacks have high thermal efficiency but weigh more. Small stacks have poor thermal efficiency, thus requiring large cooling systems. The solution is to strike a balance between stack size, thermal efficiency, and fuel efficiency that minimizes the propulsion system weight for a given power required, while maximizing the loiter.

3. **System complexity**

   The balance of plant equipment around a PEM stack could consist of many active, moving components that contribute to system complexity and reduce reliability. These include air compressors (and associated intercooler), humidification systems, radiators, fans (and their driving system), and hydrogen valves. The solution is to use passive components under low stress wherever possible. Eliminate the need for an air compressor by operating the stack at atmospheric pressure. Simplify the humidification system by using a passive humidifier that works via osmosis. Reduce control system requirements by allowing mechanical regulators to maintain the proper hydrogen pressure at the anode.

12.1 Survey of Hydrogen Fuel Cells

To assess the state-of-the-art, a survey of more than ten commercially available PEMFC stacks was conducted. These were all ground-based stacks. Compiling a complete dataset proved challenging due to limited and inconsistent supplier information. It is often unclear what the reported stack efficiency is referenced to: either the Gibbs free energy voltage or the Nernst voltage. Weight reporting is also inconsistent, with some manufacturers omitting key components like casings to inflate specific power figures. Despite these limitations, a specific power trend was derived from available data, supplemented by in-house testing of four stacks rated at 0.3, 0.8, 1.2, and 4 kW (0.4, 1, 1.6, and 5.4 hp). The results, shown in Figure 12.1, yield the following relation between PEMFC mass and power:

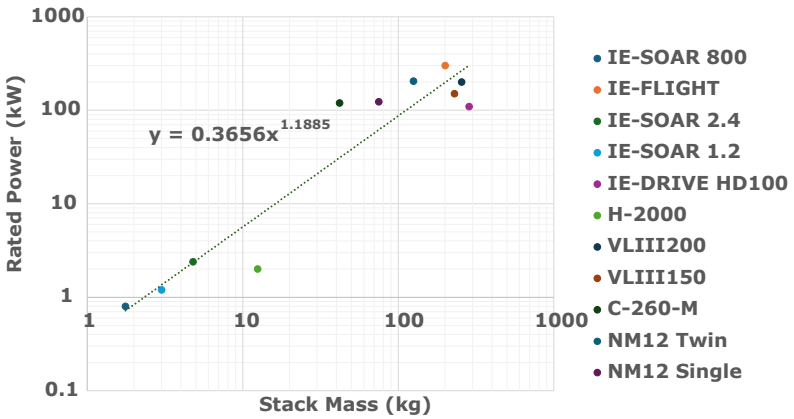

Figure 12.1: Survey of PEMFC specific power

$$M = 2.735(P)^{0.814}$$

where P is in kW, and M is in kg. This gives a specific power of approximately only 0.366 kW/kg (0.22 hp/lbs) when considering the full system with balance of plant. Two PEMFCs from this analysis will now be discussed below.

12.1.1 Horizon Fuel Cell - VLIII200

The VLIII200 is a 200 kW (268 hp) fuel cell developed for heavy-duty automotive applications such as trucks and buses. It served as a valuable reference system due to the vendor's willingness to share detailed documentation down to the component level. The VLIII200 integrates key balance of plant (BOP) components, including high- and low-temperature cooling loops and a 25 kg (55.1 lbs) compressor, which is roughly 10% of the total system mass. This highlights the compressor as a major design driver. It was determined that the trade between better cell performance but more balance of plant mass was a net loss for low altitude flight. *Wyvern* opts to eliminate the compressor to reduce both weight and system complexity.

12.1.2 Intelligent Energy - FLIGHT

The IE FLIGHT PEMFC is merely a concept, though a promising one. Designed to replace turboprop engines in fixed-wing aircraft, it operates above 120°C (248°F) and uses a compressor for high-pressure air supply. Both humidification and cooling are achieved through direct water injection, removing the need for dedicated cooling channels in the bipolar plates. After passing through the cathode, the air is cooled and dehumidified via a condenser, which also handles heat rejection, eliminating the need for a traditional radiator and fan. This evaporative cooling approach offers a compelling direction for future high-temperature PEMFC systems. Thus, none of them were directly applicable or available now. It was necessary to design a new system.

12.2 Power Sharing Strategy

A major challenge in integrating hydrogen PEMFCs into vertical lift vehicles lies in meeting the high power demands of hover and axial flight. Due to their typically low specific power, PEMFCs alone are not ideal for such applications. However, when paired with a high-power battery, they can be effectively leveraged in a hybrid architecture. Although the specific energy of hydrogen including storage, is lower than that of conventional fuels like gasoline or kerosene (see Table 12.6), it still far exceeds that of batteries by an order of magnitude, offering significantly extended endurance and range than batteries alone.

12.2.1 Regulated Power Share

Wyvern employs a dual-source propulsion strategy that distributes the power demand between a high-power battery and a PEMFC. In this hybrid system, the battery supplies power during peak-demand phases, such as hover, while the PEMFC allows extended endurance throughout the mission. Power sharing is achieved through a parallel configuration, with both sources connected to a common high-voltage bus via DC/DC converters. The bus is regulated at 795 V, aligning with motor and RFP voltage constraints (see Section 12.7 for propulsion architecture details). Due to the RFP-imposed 30 kg (66 lbs) battery mass limit, the battery contributes less than 25% of the power during OGE hover. Nonetheless, this contribution is highly impactful because the battery significantly reduces the required stack size and mitigates cooling demands, as PEMFC thermal load rises exponentially near maximum output. The resulting power distribution between PEMFC and battery over the mission is illustrated in Figure 12.2, with a summary provided in Table 12.9.

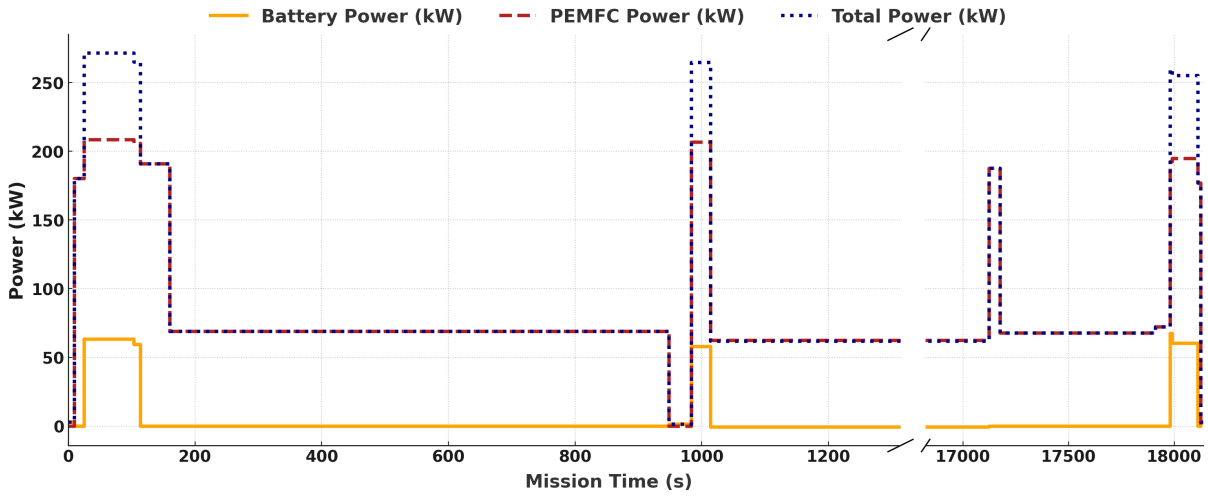

Figure 12.2: PEMFC-Battery power share during the mission

12.2.2 Unregulated Power Share

Unregulated power sharing was explored as a means to eliminate one DC/DC converter, with the concept modeled using the circuit shown in Figure 12.3. The goal was to size the battery and PEMFC to passively achieve a desirable power split across various load conditions. However, in such a configuration, power distribution is highly sensitive to the source voltages, particularly the battery, whose voltage varies with state of charge (SOC). As shown in Figure 12.4, decreasing SOC causes the PEMFC to take on a greater share of the load.

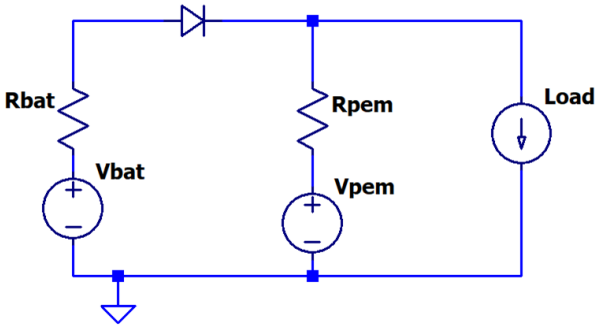

Figure 12.3: Unregulated power share model

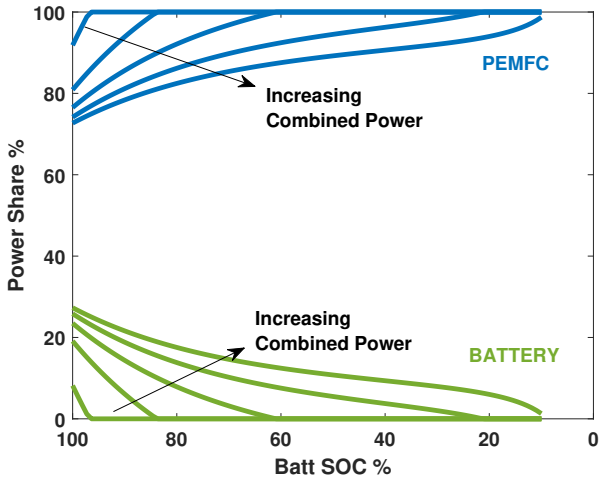

Figure 12.4: Unregulated power share - battery SOC

This dynamic undermines system optimization: if the PEMFC must be sized for high output at low SOC, the resulting stack becomes unnecessarily large, negating the weight savings from omitting a converter. Conversely, at high SOC, the battery may exceed its continuous power rating. Mitigation strategies, such as limiting battery output at low SOC or oversizing the stack and cooling system, were found to increase system weight beyond that of simply retaining dual DC/DC converters. Ultimately, conventional regulated sharing remains the most weight-efficient and robust solution.

12.3 Fuel Cell Design

The basis for fuel cell design was [27]. This provided a good sizing model for obtaining performance estimates early in the design process, as well as a method of modeling a PEM cell i-v curve. However, for detailed design, additional refinements were necessary. These included weight-heat optimization, detailed cooling system design, ϵ-NTU heat analysis, and, detailed design of membrane Electrode assembly and bipolar plates.

12.3.1 Choosing the PEM Cell

The PEM cell forms the core of the PEMFC system, where hydrogen and oxygen react electrochemically to generate electricity. As such, selecting a high-performance cell is critical. Cell performance is influenced by catalyst loading, reactant channel design, and the operating pressure across the membrane. A key metric for evaluating cell performance is the power output per unit active area (W/cm^2). Three candidate cells were evaluated for potential integration into *Wyvern*'s PEMFC system. An 800 W cell was experimentally tested in-house but delivered a low power density of approximately $0.25\,W/cm^2$, rendering it unsuitable. A second option, developed by Swiss manufacturer Axane, demonstrated an impressive specific power of 3.67 kW/kg in their M-240 stack. However, achieving this performance required operation at 2.2 bar absolute pressure. Given *Wyvern*'s compressor-free architecture, this cell was excluded. Notably, this same cell was investigated by the U.S. Department of Energy (DOE) and found to offer performance comparable to that of the Toyota Mirai fuel cell stack [61]. The final selection was a modern cell of similar type described in [27, 62]. This was deemed a conservative cell that provided adequate performance. It delivers a power density of approximately 0.8 W/cm^2 at 1 atm. Moreover, the cell is well-characterized, with detailed parameterization across a range of stack pressures, enabling reliable modeling and integration into the propulsion system.

12.3.2 Cell Operating Point

The cell operating point was chosen using MDO (Section 4.2.5) to maximize the loiter, accounting for the weight minimization of the propulsion system. The cell polarization curve at 1 atm with the design operating point is shown in Figure 12.5 at $1.33\,A/cm^2$. At this current density, the power density is 0.78 W/cm^2 and the cell voltage is 0.544 V. Designing the PEMFC stack with a high cell count is advantageous for the overall power system, as it reduces the required current for a given power output. Lower current translates to reduced conductor sizing, minimized resistive (I^2R) losses, and improved overall system efficiency. For *Wyvern*, the stack was configured to operate below a maximum voltage of 840 V, conforming with the RFP, while maximizing the number of series-connected cells. However, high cell counts introduce certain design challenges, such as ensuring membrane hydrataion and mechanical integrity. In large stacks, internal cells are more susceptible to vibration-induced misalignment and bowing. To address these issues, the stack was divided into two electrically connected substacks. This modular configuration simplifies thermal and hydration management, enhances mechanical robustness, and eases assembly and maintenance.

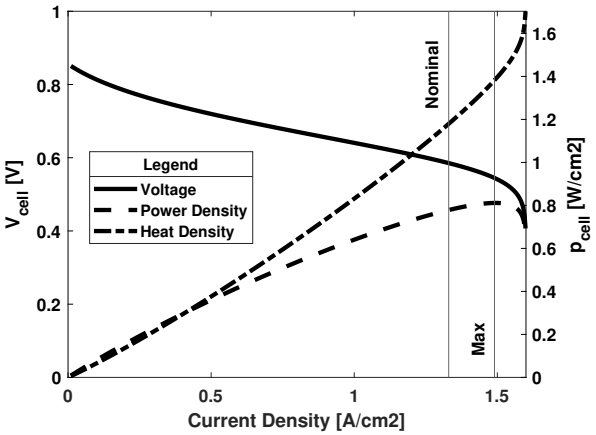

Figure 12.5: Modern cell i-v at 1 atm

12.3.3 Cell Construction

A PEM fuel cell consists of a stack of cells connected in series. The heart of a PEM cell is the proton exchange membrane, which is usually a Nafion^{TM} layer. This layer is sandwiched between a thin catalyst, a gas diffusion layer (GDL), a gasket, and a bipolar plate. The catalyst is usually a very thin coating of Platinum. The gas diffusion layer allows the reactants to react more completely. The gasket creates a seal for the gaseous hydrogen and air on each side of the PEM. Finally, bipolar plates create the boundary of each cell. The bipolar plates contain channels for the reactants and cooling. The cell design for *Wyvern* is shown in Figure 12.6. The densities and thicknesses for each layer are given in Table 12.1.

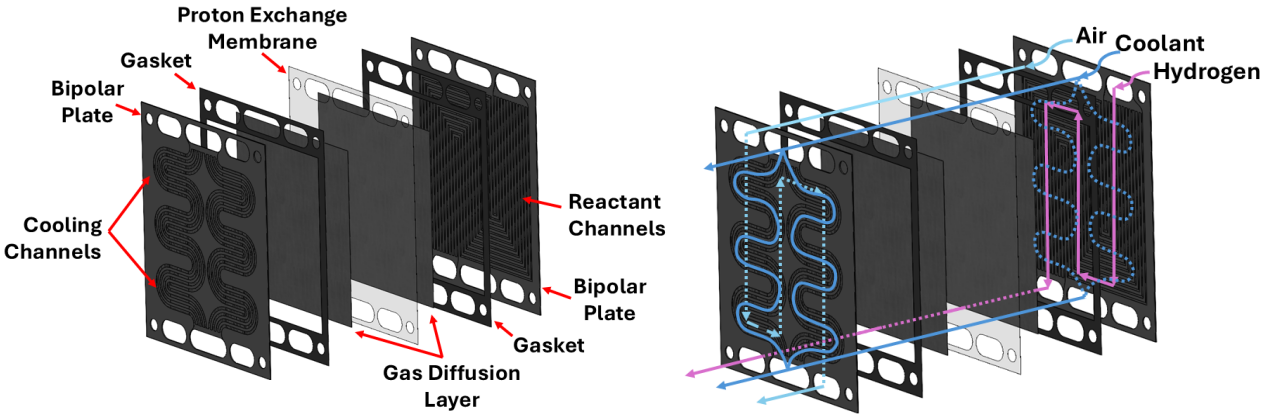

(a) Cell layers (b) Fluid flow

Figure 12.6: *Wyvern* PEMFC cell - exploded view

Table 12.1: Cell layer properties

Cell Layer	Material	Density $\frac{kg}{m^3}$ ($\frac{slug}{ft^3}$)	Thickness mm (mil)	Quantity	Mass SubTotal g (oz)
PEM	Nafion^{TM}	1000 (1.94)	0.05 (1.97)	1	2.15 (0.076)
Catalyst	Platinum dusting	0.5 (0.001)	0.00002 (0.0008)	2	6.53×10^{-7} (2.3×10^{-8})
GDL	Carbon Paper + PTFE	440 (0.85)	0.2 (7.87)	2	5.76 (0.2)
Gasket	Rubber	1000 (1.94)	0.2 (7.87)	2	4.06 (0.14)
Bipolar Plates	Graphite	1296 (2.51)	1.12 (44.1)	2	99.84 (3.52)
				Total:	118 (4.16)

29% of the bipolar plate material is removed to create the reactant channels, coolant channels, and tie rod holes. The bipolar plates have an area 48% greater than the cell active area. Finally, the gasket has an area 68% less than the cell active area.

12.3.4 Stack Construction

Table 12.2: PEMFC basic design parameters

Number of Cells	824
Cell Active Area	327 cm^2
Cathode Pressure	1 atm
Nominal Power	210 kW (282 hp)
Maximum Power	219 kW (294 hp)

The core of the PEMFC are the PEM cells. The cells are divided into two sub-stacks to shorten the length of the fuel cell. A current collector plate made of copper caps the end of each sub-stack. An insulator layer provides electric insulation from the sub-stack to the end plate. A stiff aluminum end plate provides ports for input and output. Eight tie rods, four per sub-stack, squeeze the sub-stacks together. This promotes air-

tight seals between the cells and provides structural integrity to the stack. The stack has a casing made of aluminum and a frame made of solid nylon. This protects the stack and insulates the high-voltage components of the stack. A small chamber is contained between the stack and its casing where the hydrogen is connected. Here, the hydrogen warms up via heat from the stack. The stack inside its casing is shown in Figures 12.18 and 12.7(c). The stack designed for *Wyvern* is shown in Figure 12.7(a) without its casing. The front of the PEMFC contains the input and output ports for coolant and reactants, as well as the power output contacts. These are labeled in Figure 12.7(b). The basic design parameters of the PEMFC are given in Table 12.2. Derived parameters for the PEMFC are given in Table 12.3. The full stack polarization curve is shown in Figure 12.8.The power is the gross power. The balance of plant loss is about 5 kW (6.5 hp), the rest is net electrical power of around 205-215 kWe (267-280 hp).

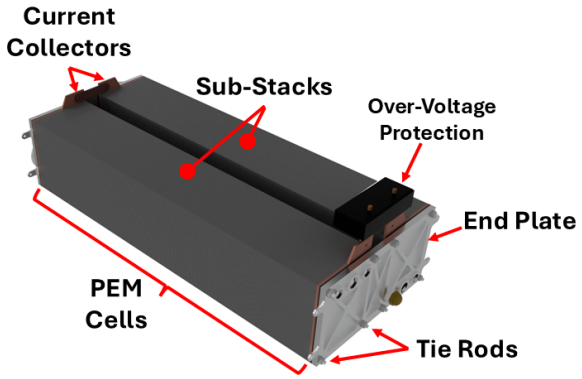

(a) PEMFC without case

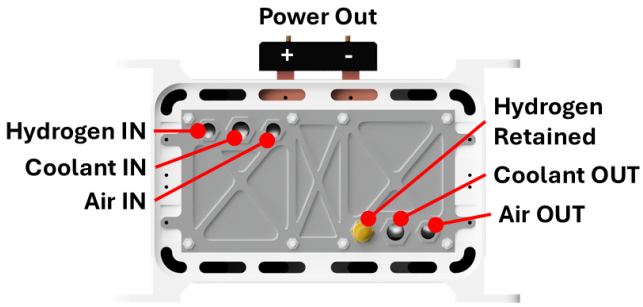

(b) PEMFC front panel

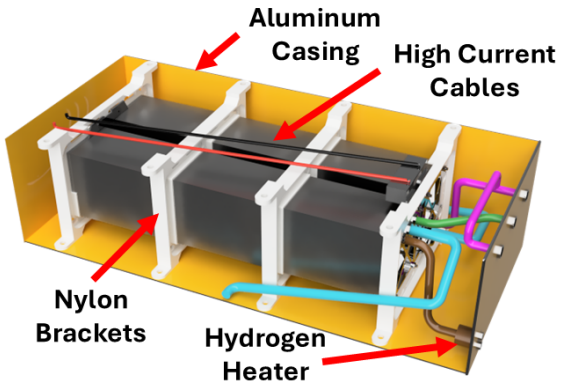

(c) PEMFC with case cutaway

Figure 12.7: PEMFC stack

12.3.5 Hydrogen Fuel Cell Control

The PEMFC delivers current at a rate dictated by the availability of oxygen and hydrogen at the membrane interface. As such, power output is governed by regulating the reactant flow rates. Hydrogen is stored in two 700 bar (10.1 ksi) tanks and mechanically regulated to maintain 1 atm absolute at the anode. A solenoid valve is integrated to shut off hydrogen flow during system shutdowns. On the cathode side, air pressure is maintained by a 0.09 m (0.3 ft) diameter fan, which is controlled to sustain a target pressure of 1 atm. Details of the air intake system are provided in Section 12.4.1. The fan control system incorporates a proportional-integral (PI) controller with collective control input to anticipate power demands. Transient loads are not expected to be an issue for the propulsion system, as time constants for PEMFCs are on the order of 10s of milliseconds [60]. During normal operation, intake air can be preheated using thermal

Table 12.3: PEMFC derived parameters

	PEMFC no Case	**PEMFC with Case**	**PEMFC + BOP**
Length, mm (ft)	1303 (4.28)	1308 (4.29)	N/A
Width, mm (ft)	532 (1.75)	682 (2.24)	N/A
Height, mm (ft)	366 (1.20)	451 (1.48)	N/A
Mass, kg (lbf)	113 (248)	127 (281)	227 (500)
Design factor Active Area (kg/m^2)	4.18	4.72	8.42
Power density (Nominal) (Rect.) (kW/L)	0.828	0.522	N/A
Specific Power (Nominal) kW/kg (hp/lbf)	1.86	1.65	**0.927 (0.564)**

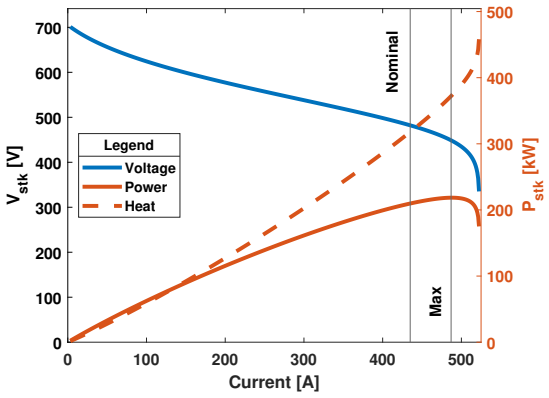

Figure 12.8: Stack I-V

exchange with hot coolant. For cold-start conditions, an electric heating element is embedded within the intake. A schematic of the air intake control system is shown in Figure 12.9.

12.3.6 PEM Cell Health

PEM cell performance can be degraded by erosion of the platinum catalyst layer and inadequate membrane hydration. Erosion of the catalysist layer occurs when the cell is cycled through high cell voltages. Degradation of the platinum catalyst leads to long-term power loss. During the loiter phase, the stack operates at approximately 60 kW (80.5 hp), corresponding to a cell current density of 0.29 A/cm^2 and a voltage of 0.7 V. According to [63], cycling up to 0.76 V preserves power output within 10% of the nominal value over 48,240 cycles. Therefore, the selected PEMFC is expected to exhibit minimal performance degradation over its operational life. For optimum performance throughout the PEMFC lift, regular maintenance should be performed to ensure the cells remain hydrated, especially after prolonged periods of inactivity.

12.4 Balance of Plant

A hydrogen fuel cell system requires several supporting subsystems beyond the stack itself, collectively known as the balance of plant (BoP). Air must be delivered to the cathode at the appropriate pressure using a blower or compressor; if the pressure exceeds 30 kPa, a low-temperature cooling loop is needed to condition the compressed air. High humidity levels are also essential to prevent membrane dehydration. Meanwhile, the heat generated during operation must be removed via a high-temperature cooling system. On the anode side, hydrogen is supplied from high-pressure storage tanks through a regulator. The components and functionality of the BOP are detailed in the following sections. See table 12.10 for a breakdown of BOP weights.

12.4.1 Air Intake

Analysis showed that the performance gains from operating the PEMFC above 1 atm did not justify the added weight and system complexity (see Section 4.2.5). As a result, *Wyvern* employs a blower-based air intake system designed to maintain cathode pressure at 1 atm absolute using a PI controller. See Figure 12.9. Downstream of the a single electric motor, intake air is thermally conditioned. During steady-state operation, air is heated via fins coupled to the stack's coolant outflow, while an electric heater is used for start-up. Air intake internals are shown in Figure 12.10. Blower specifications are provided in Table 12.4.

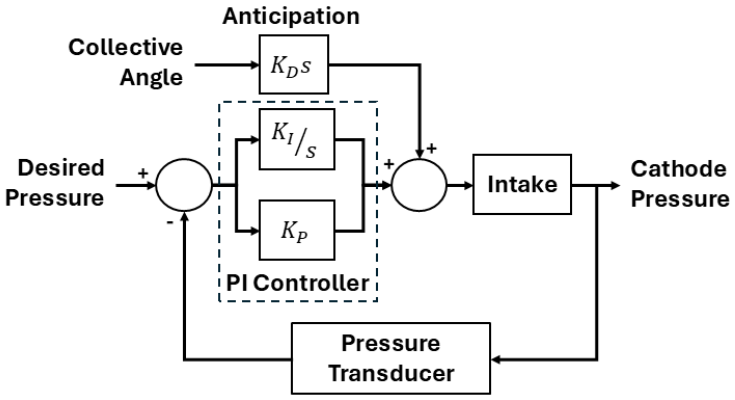

Figure 12.9: Air intake control system

Table 12.4: Air intake design specifications

Specification	Value
Design Air Mass Flow	0.32 kg/s (0.71 lb/s)
Design Air Velocity	3.72 m/s (12.2 ft/s)
Fan Radius	0.15 m (0.49 ft)
Max Power	50 W (0.67 hp)
Max RPM	2000
Mass	8 kg (17.6 lb)

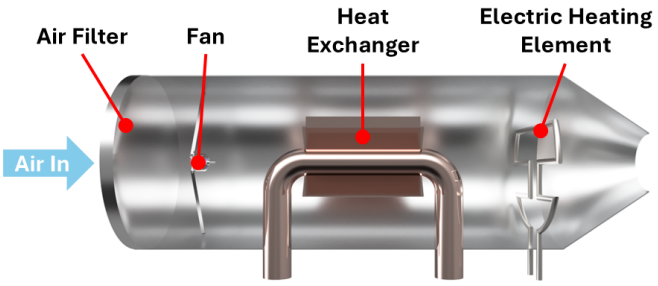

Figure 12.10: Air intake cutaway view

12.4.2 Humidification

PEM cell performance is highly sensitive to membrane hydration. Although water is generated as a byproduct of the electrochemical reaction, it is often removed by the airflow and evaporated by the stack heat. Therefore, continuous humidification of the cathode air stream is essential. One approach involves vaporizing nozzles that inject water droplets into the airflow; however, this method necessitates a dedicated water supply and complex control systems. A more elegant solution uses hydrophilic hollow fiber tubes, which allow water vapor to passively diffuse into the dry incoming air without direct mixing. This passive humidification system relies entirely on reaction byproducts, eliminating the need for external water tanks and reducing system complexity and weight. Hollow fiber tubes have been used extensively in PEMFC automotive applications and have a proven track record [64].

12.4.3 High Temperature Cooling System

Effective thermal management is essential for the *Wyvern* powerplant, given the substantial heat generated by the PEMFC stack and supporting systems. The stack heat output is given by $Q = (E_h - v)\, j\, n\, A_c$, where E_h is the ideal cell voltage, v the operating voltage, j the current density, n the number of cells, and A_c the cell active area. Additional heat arises from motor inefficiencies, battery resistance, and DC/DC converter losses. While up to 12% of this heat is passively dissipated via inlet air and hydrogen preheating, exhaust, and convection, the remainder must be actively rejected. At peak continuous output (277 kW at SL-ISA), this equates to a required net heat rejection of approximately 300 kW, driving the design of a high-performance, high-temperature cooling system.

Thermal Design Requirements *Wyvern* must reject a peak of 300 kW (402 hp) of waste heat, maintaining an operational set-point of 80 °C (176 °F), and a steady-state stack temperature $\leq$ 90 °C (194 °F), being compliant with CS-27.1041. A summary of the HTC is provided in Table 12.5. Because the main rotor

gearbox (MGB) already delivers mechanical power to the rotors, the coolant pump, and the radiator fan are mechanically driven from the MGB and the tail driveshaft (via belt-drive) to avoid additional electric loads and to simplify the architecture.

Table 12.5: Cooling system design during maximum power

Parameter	Symbol / Value	Comment
Peak waste heat	$Q_{\max} = 300\,\text{kW}$	Hover
Stack temp. limit	$T_{\max} = 90\,^{\circ}\text{C}$	RFP
Nominal set-point	$T_{\text{set}} = 80\,^{\circ}\text{C}$	Closed-loop control
Coolant mass flow	$\dot{m}_{\text{H}_2\text{O}} = 173\,\text{L/min}$	Dual channel
System Δp	$\Delta p = 300\,\text{kPa}$	Includes radiators
Coolant inventory	$m_{\text{H}_2\text{O}} = 30\,\text{kg}$	10 s residence

System Architecture The cooling system is split into two identical loops isolated at the component level (Figure 12.11). One loop services the PEMFC Stack, one electric motor, the high-power HV DC/DC converter, and the other loop services the flight battery, the second motor, and the low-power HV DC/DC. providing *N+1* redundancy. The external vents for cooling are shown in Figure 12.12. A rendering of the internal HTC architecture is shown in Figure 12.14.

- **Coolant**: De-ionized water for electrical isolation.
- **Radiator** (each): Aluminum, brazed bar-and-plate core, 355 mm × 355 mm × 75 mm, weight 7.5 kg.
- **Fan**: 610 mm axial fan, 1725 RPM, Power 1.5 kW and $\dot{V}$ = 9300 CFM ($\approx 4.4\ \text{m}^3/\text{s}$).
- **Coolant Pump**: FPR-751 centrifugal pump, 1750 RPM, delivers 173 L/min against 300 kPa, power 2.6 kW.

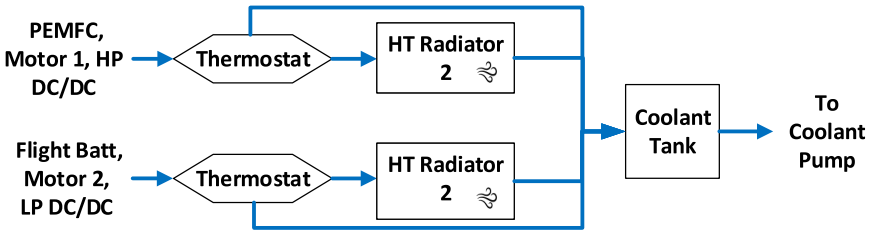

Figure 12.11: *Wyvern* HTC architecture

Single radiator sizing (for 150 kW) To remove 150 kW while the coolant cools from 85°C to 60°C, the water flow must be about 1.44 kg s^{-1} ($\approx 86\ \text{L min}^{-1}$), obtained from $\dot{m} = Q/(c_p \Delta T)$ with a specific heat of 4.18 kJ kg^{-1} K^{-1}. With ambient air entering at 15 °C and leaving near 35 °C at a face velocity of 20 m s^{-1}, the log mean temperature difference (LMTD) ΔT is roughly 48 °C, so the overall conductance requirement is $UA = Q/\Delta T \approx 3.2\ \text{kW K}^{-1}$. An $\epsilon - NTU$ analysis was also performed, which gave a similar ΔT of 47.2°C.

Assuming a brazed aluminum louvre-fin core that gives an overall heat-transfer coefficient of about 250 W m^{-2} K^{-1}, the finned area needed is roughly 12.6 m^2. With a typical fin-to-frontal area ratio of 100:1, this translates to a frontal area near 0.13 m^2. Maintaining the core 75 mm thickness leads to a required length and height of about 355 mm, giving an envelope of 355 mm × 355 mm × 75 mm. The scaled dry mass is roughly 7.5 kg, estimated from the radiator data obtained from the test [65]. This compact core meets the 150 kW target with a small thermal margin while remaining easy to package inside the fuselage with the radiator ducts on two sides of the driveshaft.

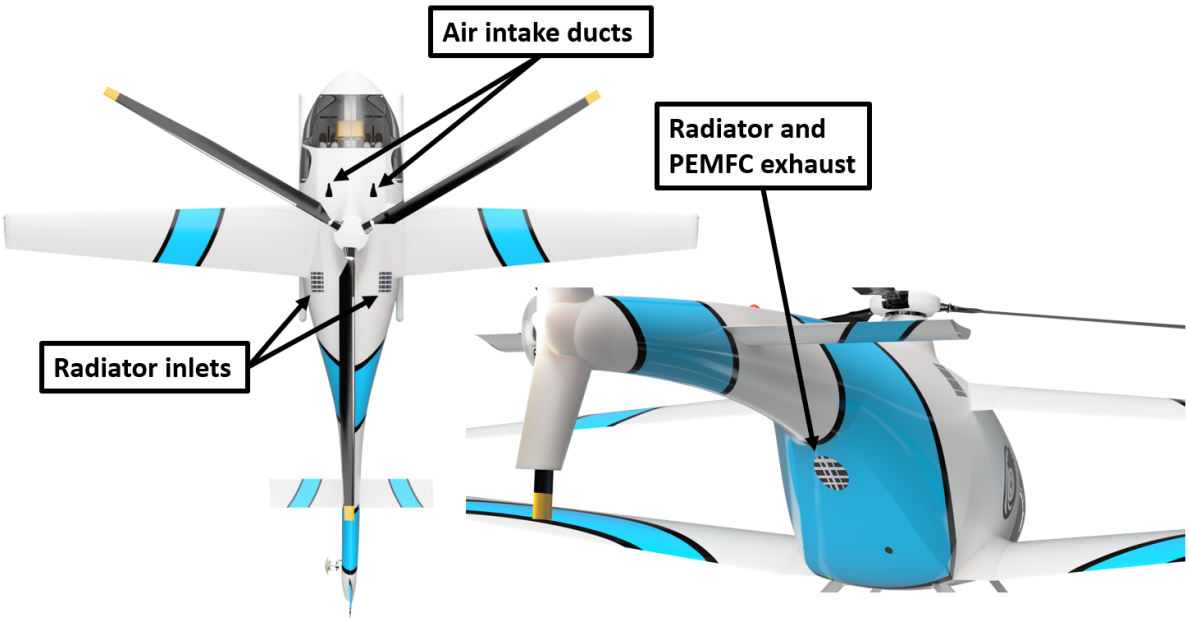

Figure 12.12: PEMFC stack + BOP system intake and exhaust

Coolant Circuit and Pump Selection The FPR-751 pump curve intersects the system head Δp at 1750 RPM almost exactly at the required $173\,\mathrm{L\,min^{-1}}$, consuming 2.6 kW power [66]. Because the pump is mounted on the MGB accessory pad, its speed is proportional to rotor speed ($\sim$1:6.73). A bypass shuttle valve maintains constant differential pressure at low power flight conditions to reduce parasitic pumping losses.

Fan Aerodynamics and Drive The 610 mm axial fan achieves the design volume flow rate $\dot{V} = 263$ $\mathrm{m^3/min}$ (9300 $\mathrm{ft^3/min}$) to maintain the necessary flow-rate of $v_{rad} = 20$ m/s (66 ft/s) over the radiator surfaces in pure cross-flow situation [67]. Shaft power varies with $\dot{V}^3$, allowing fan power to track rotor rpm automatically. V-belt drive from the tail drive shaft provides 1.6 kW continuous during the maximum power condition.

Deionizer A deionizer is essential to maintain low electrical conductivity in the coolant, preventing potential short circuits across the PEM cells, which are all in direct contact with the same cooling loop (Figure 12.6(b)). The deionizer is a passive, power-free component that continuously purifies the coolant. Its placement within the high-temperature cooling system is illustrated in Figure 12.14.

Temperature Control The temperature of the coolant is maintained by a passive, mechanical system of thermostats and bypass circuits. The same type of thermostat used in automotive applications is used. During warm-up, the thermostat blocks coolant flow to the radiator, allowing components to quickly reach their operating temperature. At around $70°C$, the wax element within the thermostat begins to expand, allowing coolant to enter the radiator. If the temperature decreases, the thermostat will begin to close. In this way, the temperature of all major systems on *Wyvern* is managed simply and reliably. Figure 12.13 shows the evolution of stack

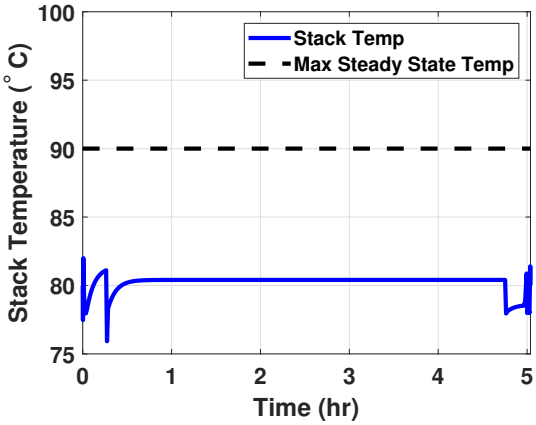

Figure 12.13: *Wyvern* stack temperature control

temperature throughout the mission, ensuring effective temperature control around 80°C.

Redundancy and Safety All propulsion components must operate at their correct operating temperatures. If coolant were to leak or stop flowing from a component such as the PEMFC or DC/DC converter, that component could overheat. To mitigate this issue, the cooling system of *Wyvern* uses two parallel cooling circuits, as shown in Figure 12.11. Flight-critical components are divided between the two circuits: PEMFC, motor 1, and the high-power DC/DC converter are on one circuit, while the flight battery, motor 2, and the low-power DC/DC converter are on another. With this system, a clogging or failure of one circuit will not result in the overheating of the entire propulsion system. Instead, only a partial power failure would occur, allowing the pilot to make a run-on landing with power on.

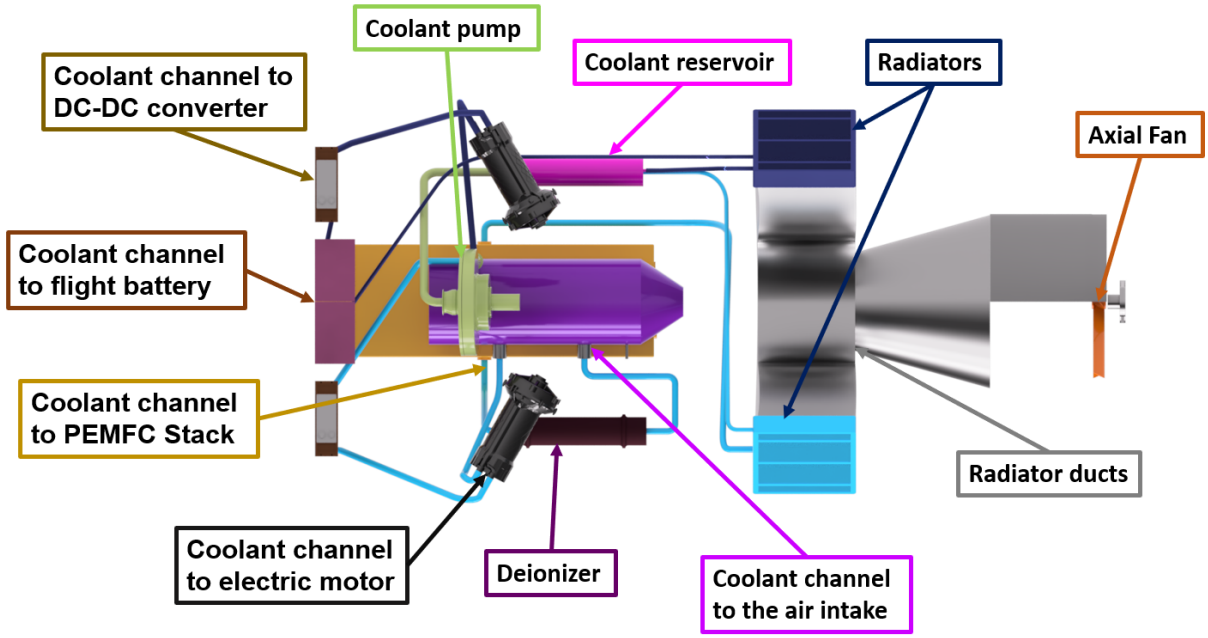

Figure 12.14: *Wyvern* high temperature cooling system

12.4.4 Hydrogen Storage

Hydrogen storage plays a critical role in determining the endurance of a PEMFC-powered aircraft. As specified by the RFP, only gaseous hydrogen is considered. While hydrogen has a higher heating value (HHV) of 39.4 kWh/kg [27], current storage technologies limit its practical specific energy. The best Type IV tanks achieve a hydrogen weight fraction of only $\sim 8.0\%$ ($wt\%_{H2} = M_{H2}/(M_{H2} + M_{tank})$), resulting in an effective specific energy of just 3.16 kWh/kg. This is significantly lower than gasoline or kerosene which exceed 10 kWh/kg due to much higher fuel-to-tank mass ratios. Gaseous hydrogen also has poor volumetric energy density, even at high pressures. A comparison of storage methods is shown in Table 12.6. Hydrogen tanks are classified into five types based on liner and pressure vessel materials, as summarized in Table 12.7. Only Type III and IV tanks are mature and practical enough for aerospace use. *Wyvern*'s hydrogen storage system is CS-27.1185 compliant, featuring a firewall between the tanks and cockpit, pressure relief valves to prevent tank rupture, and onboard hydrogen sensors to detect leaks and alert the pilot.

Hydrogen tank selection for *Wyvern* prioritized a high hydrogen weight fraction and minimal volume, the latter being inversely related to gas density. A survey of commercially available Type III and IV tanks at 350 and 700 bar was conducted, with results summarized in Figure 12.15. Figure 12.15(a) highlights the volumetric advantage of 700 bar storage, offering 66% higher volumetric efficiency than 350 bar tanks. Figure 12.15(b) shows that Type IV tanks provide, on average, a 49% higher hydrogen weight ratio than

Table 12.6: Effectiveness of gaseous hydrogen storage compared to gasoline and kerosene

	Hydrogen 350 bar, 15°C	**Hydrogen 700 bar, 15°C**	**Gasoline**	**Kerosene**
Density (kg/m^3)	23.99	40.13	722.13	840
Mass Specific Energy (kWh/kg)	39.44	39.44	12.22	11.94
Volume Specific Energy (kWh/L)	0.95	1.58	8.83	10.03
Best Fuel to Tank + Fuel Weight Ratio	8.00%	6.50%	90.0%	90.0%
Combined Fuel + Tank Mass Specific Energy (kWh/kg)	3.16	2.56	11.0	10.8

Table 12.7: Hydrogen tank types

Type-I	**Type-II**	**Type-III**	**Type-IV**	**Type-V**
All-metal steel or aluminum	Steel or aluminum liner Composite hoop wrap	Steel or aluminum liner Composite full wrap	Plastic liner Composite full wrap	No liner All-composite

Type III. Interestingly, Figure 12.15(c) reveals that within Type IV tanks, 350 bar models offer a 21% higher gravimetric efficiency than their 700 bar counterparts. Finally, Figure 12.15(d) demonstrates that the hydrogen weight ratio improves with tank volume due to favorable surface area-to-volume scaling.

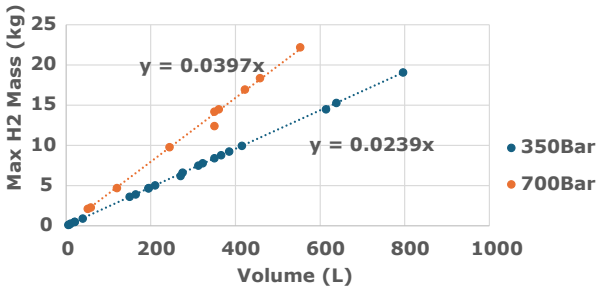

(a) H_2 mass vs. volume of type III & IV tanks

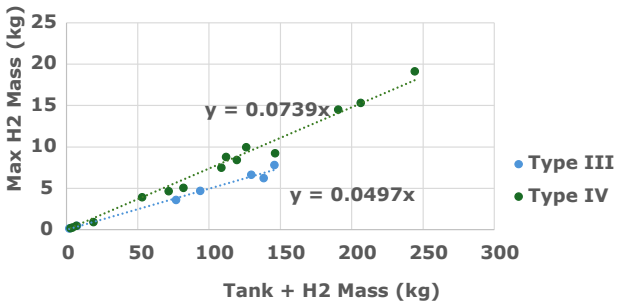

(b) H_2 mass vs. total tank mass at 350 bar

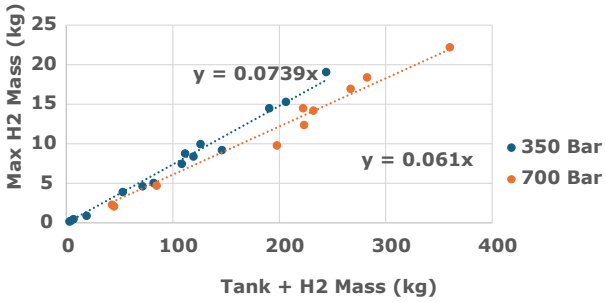

(c) H_2 mass vs. total mass of type IV tanks

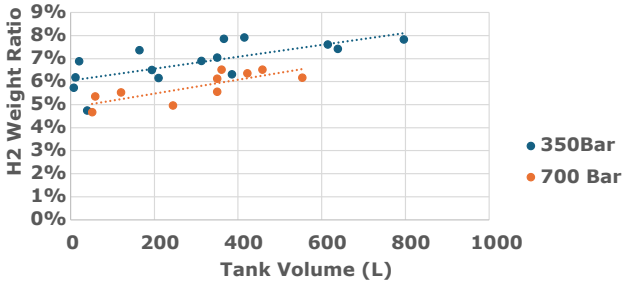

(d) H_2 weight ratio vs. tank volume of type IV tanks

Figure 12.15: Summary of hydrogen storage characteristics under varying tank pressure and tank types.

These results underscore a trade-off: 700 bar tanks need less volume but less efficient by weight whereas 350 bar tanks need more volume but may be more efficient by weight. *Wyvern* adopts two NPROXX AH620-70 Type IV tanks at 700 bar, each with a 5.5% hydrogen weight fraction, to meet volumetric constraints of accommodating all balance-of-plant components within the fuselage, within acceptable CG travel.

12.5 Battery Design

The battery is a critical component of *Wyvern*'s propulsion architecture, primarily due to its superior power density compared to PEM fuel cells. This is an essential attribute for meeting the high power demands of vertical lift during hover and ascent. While PEMFC stacks offer nominal power densities between 1–3 kW/kg, depending on pressure and operating conditions, their system-level efficiency is typically below 50%. As a result, substantial cooling, humidification, and BOP systems are required, reducing effective power density to $< 1kW/kg$. In contrast, Li-Ion batteries maintain power densities of 2–4 kW/kg at the cell level, making them more weight-efficient for peak power support. Following this logic, Wyvern incorporates the maximum battery mass permitted by RFP constraints of 30 kg. Lithium-Polymer batteries offer high power density ($> 10kW/kg$) but suffer from low specific energy. Silicon-anode Li-Ion cells provide a more balanced solution. Ampirus's SA80 cell offers 400 Wh/kg and 4 kW/kg, making it well-suited to *Wyvern*'s requirements. Due to expansion during operation, these cells require compression packaging. Accounting for structural and packaging mass, only 16.9 kg is allocated to active cell material, yielding a packing factor of 1.78. Each SA80 cell weighs 86 g, allowing 196 cells in the pack (Figure 12.16).

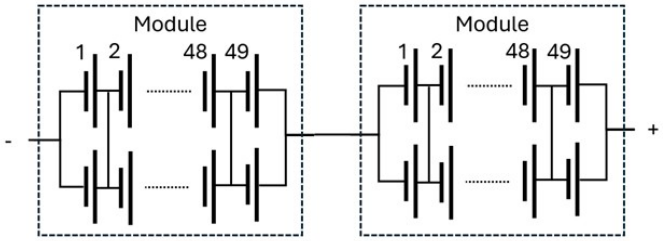

Figure 12.16: Battery pack design.

For redundancy and manufacturability, a 98S2P configuration is adopted, split into two 49S2P modules. Each module is enclosed in a sealed, CS-27.1353-compliant casing to prevent hazardous gas leakage. Battery specifications are summarized in Table 12.8.

The battery is recharged during low-power loiter to ensure sufficient capacity for the final hover segment. It delivers 13.92 Ah during the mission. Since the pack is 20 Ah, it would be able to complete the mission without the in-flight recharging. This leaves the battery at 64% SOC with in-flight recharging and 30.4% SOC without it. Operating parameters are detailed in Table 12.9.

Table 12.8: Battery specifications: cell, module, and pack

(a) SA80 Cell

Capacity	10 Ah
Voltage (Nominal)	3.42 V
Voltage (max)	4.25 V
Voltage (min)	2.50 V
Discharge Current	10 C
Resistance	7 mΩ
Mass	86 g
Cathode	NMC
Volume	40 mL
Energy Density	400 Wh/kg
Power Density	4 kW/kg

(b) Module

Cells/Group	2
Groups/Series	49
Cells/Module	98
Max Voltage	208 V
Nom. Voltage	168 V
Min Voltage	123 V
Mass	15 kg
Resistance	171 mΩ
Capacity	20 Ah
Energy	3.35 Wh

(c) Pack

Modules Series	2
Modules Parallel	1
Total Modules	2
Total Cells	196
Max Voltage	417 V
Nom. Voltage	335 V
Min Voltage	245 V
Mass	30 kg
Resistance	342 mΩ
Capacity	20 Ah
Energy	6.7 kWh
Power (max)	67 kW
Energy Density	223 Wh/kg
Power Density	2.23 kW/kg

12.5.1 Battery Management System

A Battery Management System (BMS) is essential for the safe and reliable operation of large-format battery packs. The BMS continuously monitors individual cell voltages and performs cell balancing to ensure uniform discharge and prevent over-discharge of any single cell. It also tracks temperature at multiple locations within the pack to detect early signs of thermal runaway. This thermal monitoring ensures compliance with CS-27.1353 over-temperature protection requirements, mandating automatic shutdown if critical thresholds are exceeded. In addition, the BMS safeguards the pack by enforcing over-current, over-voltage, and under-voltage protections, ensuring both operational safety and long-term battery health.

12.5.2 Battery Charge Controller

The battery charge controller ensures safe and efficient charging of the flight battery. A complete charge cycle follows a two-stage process: an initial constant-current phase until the pack reaches its maximum voltage, followed by a constant-voltage phase until current draw tapers to near zero. The pack supports rapid charging to 80% SOC in under 10 minutes at a 5C rate (100 A), though slower rates are preferred to reduce thermal stress and fire risk. Charging can occur either in flight, when surplus power is available from the PEMFC, or via an external ground port, both managed by the charge controller. To maximize loiter endurance, battery charging during flight is minimized, ensuring all energy is utilized by mission end. However, limited charging is performed during the loiter phase to ensure sufficient backup capacity in case of PEMFC failure. The battery is capable of completing all power-sharing segments without mid-mission recharging.

12.6 Powerplant Health Monitoring System

The powerplant health monitoring system continuously tracks key operational parameters of both the PEMFC and flight battery to assess system status and ensure safe operation. For the PEMFC, monitored metrics include: stack temperature, cathode and anode pressures, coolant inlet/outlet temperatures, coolant pressure, output voltage, and current. For the battery system, the monitoring suite includes: cell and pack temperatures, coolant temperature and pressure, output voltage, and current draw. These data streams are fed into the avionics computer via a dedicated health monitoring interface, enabling real-time status reporting and fault detection. The system supports pilot situational awareness by displaying state-of-health (SOH) indicators, thermal warnings, pressure anomalies, and power delivery trends for both power sources.

12.7 Powerplant Architecture

The propulsion architecture for *Wyvern* is shaped by the complementary characteristics of its energy sources and constraints imposed by the customer. While hydrogen PEMFCs offer high specific energy, they lack sufficient specific power for demanding phases such as hover. As a result, the integration of a high-power battery was identified early as essential (Section 12.5).

Multiple hybridization strategies exist for combining a battery with a fuel-based power source. In a full hybrid configuration, the battery and fuel cell are connected in parallel; both can supply power to the load, and the fuel cell can charge the battery, though external charging is not used. In contrast, a range extender places the power sources in series: the drivetrain is powered solely by the battery, which is recharged by the fuel cell. This approach requires the battery to support the full power demand and precludes external charging. Lastly, the plug-in hybrid—similar to the full hybrid—features a parallel architecture, but allows the battery to be charged independently via an external port. Wyvern adopts a plug-in hybrid configuration

to ensure both the PEMFC and battery are fully charged before flight. This architecture accommodates the 30 kg battery constraint, which is insufficient alone to sustain hover, while also providing redundancy: either power source can supply limited emergency propulsion in the event of a failure.

The full propulsion architecture is shown in Figure 12.17. The high-temperature cooling system (Figure 12.11) features two radiators, with critical components distributed between them to ensure fault tolerance, ensuring continued operation in the event of a single-point failure.

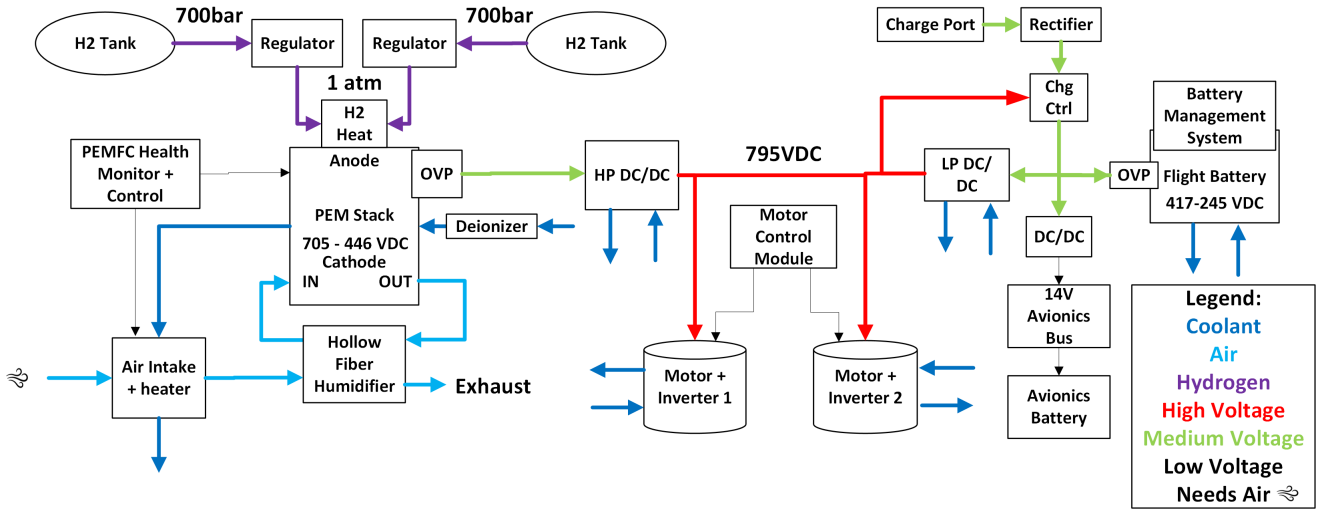

Figure 12.17: *Wyvern* powerplant schematic

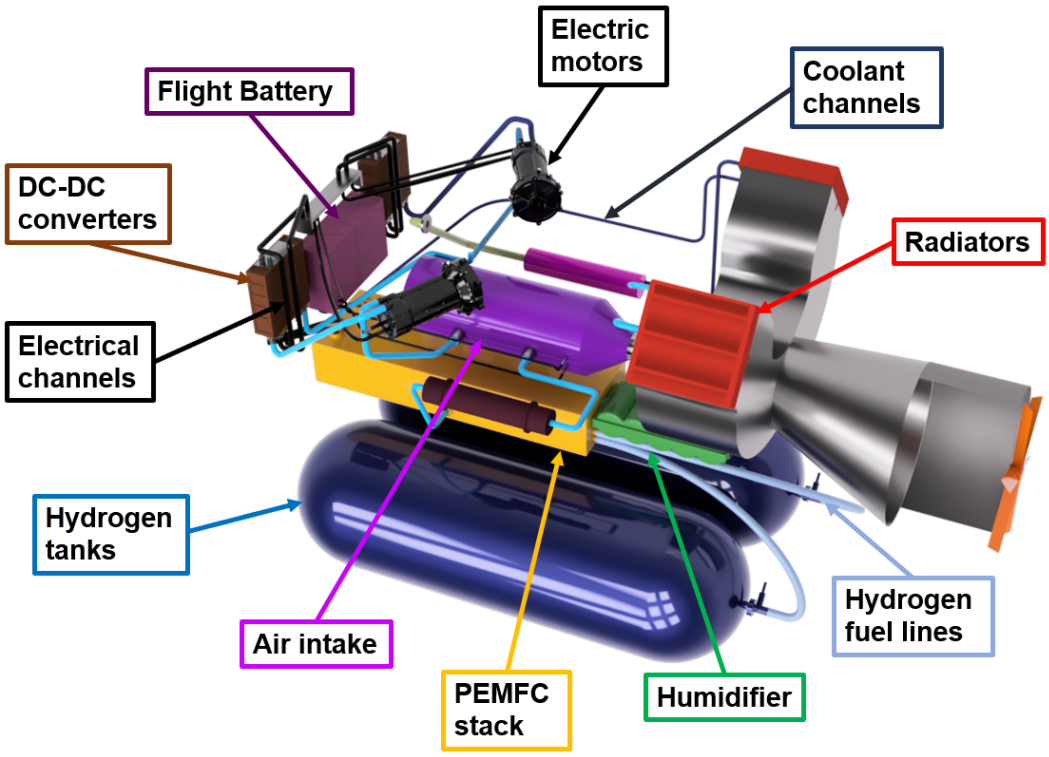

Figure 12.18: *Wyvern* powerplant layout

Table 12.9: Propulsion system operating parameters

Mission Segment	Time (s)	Power Required kW (hp)	Battery Power kW (hp)	PEMFC Power kW (hp)	Battery Pwr Share (%)	PEMFC Pwr Share (%)	Battery SOC (%) at seg. end	PEMFC SFC $\frac{kg}{kWh}$ ($\frac{lb}{hphr}$)
1	10	3 (4.03)	3 (4.03)	0 (0)	100	0	100	-
2	15	180 (242)	0 (0)	180 (242)	0	100	100	0.068 (0.112)
3	79	272 (365)	63.1 (84.8)	208 (280)	23	77	78	0.0713 (0.117)
4	10	265 (356)	59.3 (79.6)	206 (276)	22	78	75	0.0707 (0.116)
5	47	191 (256)	0 (0)	191 (256)	0	100	75	0.0689 (0.113)
6	788	69 (92.3)	0 (0)	68.8 (92.3)	0	100	75	0.0722 (0.119)
7	36	1.5 (2.01)	1.5 (2.01)	0 (0)	100	0	75	-
8	30	265 (355)	57.9 (77.8)	207 (277)	22	78	67	0.0709 (0.117)
9	16110	62 (83.4)	-0.559 (-0.75)	62.7 (84.2)	-1	101	100	0.0739 (0.121)
10	53	188 (252)	0 (0)	188 (252)	0	100	100	0.0686 (0.113)
11	736	68 (90.9)	0 (0)	67.7 (90.9)	0	100	100	0.0725 (0.119)
12	69	72 (96.8)	0 (0)	72.1 (96.8)	0	100	100	0.0715 (0.117)
13	10	260 (349)	67.5 (90.6)	192 (258)	26	74	97	0.0690 (0.113)
14	120	255 (342)	60.4 (81.1)	195 (261)	24	76	64	0.0693 (0.114)
15	15	177 (237)	0 (0)	177 (237)	0	100	64	0.0678 (0.111)
16	10	3 (4.03)	3 (4.03)	0 (0)	100	0	64	-

12.8 Motor Selection

Motor selection for *Wyvern* was driven by two primary criteria: the ability to deliver at least 136 kW of continuous power per motor and a high specific power to minimize system weight. Three candidates were evaluated: the EMRAXX-268, H3X HPDM-140, and H3X HPDM-180R. The EMRAXX-268 offers a high power output of 210 kW but at a mass of 22 kg, resulting in a specific power of 9.5 kW/kg. Although suitable for direct-drive fixed-wing applications, its oversized capacity would lead to unnecessary mass in *Wyvern*'s dual-motor configuration. The H3X HPDM-140 delivers 140 kW at just 11 kg, achieving an impressive 12.7 kW/kg specific power. This is enabled by ultra-high operating speeds, up to 20,000 RPM, which reduce torque and allow for lightweight internal components. However, such high rotational speeds are incompatible with *Wyvern*'s low-speed, high-torque rotor system, necessitating a large and heavy external reduction drive. The H3X HPDM-180R addresses this limitation by integrating a high-ratio planetary gearbox directly into the motor casing. While its specific power is slightly lower at 11.25 kW/kg, the integrated reduction stage provides high output torque suitable for rotorcraft applications without the added complexity and mass of a separate gearbox. Moreover, motor selection in rotorcraft is fundamentally constrained by specific torque, not specific power. Based on these trade-offs, the H3X HPDM-180R was selected for *Wyvern* as the optimal solution balancing power, torque delivery, integration simplicity, and weight efficiency.

12.9 Weight Breakdown

The weights of each component in the propulsion system are broken down in Table 12.10.

Table 12.10: Propulsion subsystem weight breakdown

PEMFC	**Mass, kg (lbf)**	**BOP**	**Mass, kg (lbf)**
Bus Bar	0.18 (0.39)	Humidifier	10 (22.1)
Casing	14.5 (32.0)	Air Intake + Tubing	8.5 (18.7)
End Plates	6.0 (13.3)	HTC	62.1 (137)
Insulating Plates	1.0 (2.28)	PEM Health Monitor	0.5 (1.10)
Correct Collector Plates	10.2 (22.4)	Power Cables	6.3 (13.8)
H_2 Plug	0.22 (0.48)	High Power DC/DC	11 (24.3)
Over-Voltage Protection	0.2 (0.46)	H_2 Heating Chamber	1 (2.21)
Cells	92.1 (203)	**Total:**	**99.4 (219)**
Tie Rods	1.98 (4.38)	**Battery**	**Mass, kg (lbf)**
Tie Rod Insulation	0.29 (0.64)	Battery Pack	30 (66.2)
Tubing	0.42 (0.93)	Low Power DC/DC	11 (24.3)
Hardware	0.023 (0.05)	Battery Management System	0.2 (0.44)
Total:	**127 (281)**	Charge Controller	1 (2.21)
HTC	**Mass, kg (lbf)**	Plug-In Charge Port	0.3 (0.66)
Coolant	30 (66.2)	**Total:**	**42.5 (93.7)**
Water Tubing	4 (8.82)	**Hydrogen Storage**	**Mass, kg (lbf)**
Water Pump	1.92 (4.23)	Tanks	422 (931)
Water Tank	2 (4.41)	Regulators	2 (4.41)
Radiator Ducting	6 (13.3)	H_2 Tubing	1 (2.21)
Radiators	15 (33.1)	**Total:**	**425 (937)**
Radiator Fan	1 (2.21)		
Thermostats	0.2 (0.44)		
Deionizer	2 (4.41)		
Total:	**62.1 (137)**		

13 Transmission Design

The main rotor is powered by a pair of electric drive motors through a multi-stage mechanical gearbox. Due to the inherently high rotational speed of the motors, a substantial speed reduction is required to match the operational speed of the rotor. This is achieved through two stages of reduction. The first stage consists of a built-in planetary gearbox within each motor, which reduces the motor shaft speed from 15,700 RPM to 2,432 RPM (during hover). Following this, the output from each motor is transmitted to the main gearbox, where their power is combined, and the speed is further reduced with a 6.73:1 reduction ratio bevel gear. This final stage brings the shaft speed down to the 348 RPM required for rotor operation. All components of the transmission system are designed to handle a total power output of 277 kW at their respective rotational speeds.

13.1 Drive System Configuration

For the second stage of the reduction, both spur gears and bevel gears were evaluated. Epicyclic (planetary) gear systems were excluded from consideration, as their primary advantage, achieving large reduction ratios in a compact package, comes at the expense of added weight, which was not acceptable given the *Wyvern*'s

mission priorities. To minimize the number of reduction stages, both spur and bevel gears were designed beyond their typical reduction ratio limits (usually below 5:1). While this non-standard approach resulted in a slight decrease in transmission efficiency from 99% to 98%, the trade-off was considered acceptable to avoid the additional weight that would be introduced by either a second reduction stage or the inclusion of an epicyclic gearbox. For this application, the marginal efficiency loss was deemed preferable to the weight penalty.

13.2 Drive System Weight Minimization

Table 13.1: Alternate gearbox architectures

Architecture	Mass
2-Stage Bevel	31.6 kg (69.7 lbs)
Single Stage Spur	11.5 kg (25.4 lbs)
Single Stage Bevel	12.9 kg (28.4 lbs)

Table 13.1 presents various candidate gearbox architectures. The weight of the main drive system is primarily determined by its physical size, which in turn is driven by the torque loads acting on the gear teeth. To minimize these torque loads, the design maintains separate torque paths for each motor until the final reduction stage, effectively reducing the forces transmitted through individual gear meshes. Several alternative gearbox configurations were evaluated to achieve the required 6.73:1 reduction ratio. These included: a two-stage bevel gear arrangement, a single-stage spur gear, and a single-stage bevel gear. The two-stage bevel gear architecture added 18 kg to the mass compared to the other configurations. The single-stage spur gear and bevel gear had very similar masses (less than 1 kg difference).

13.3 Configuration Choice

A single-stage bevel gearbox was selected as the final configuration due to its low weight and the design flexibility it offers for internal component placement. Specifically, the use of bevel gears allows the motors to be positioned higher within the airframe, creating valuable space below for critical systems such as hydrogen tanks, the air intake system for the PEMFC stack, and the stack itself. While the single-stage bevel gearbox is marginally heavier than the single-stage spur gear in isolation, this comparison does not account for the additional bevel gear required to redirect power to the tail rotor drive shaft in the spur gear configuration. When the mass of this additional bevel gear is included, the overall weight of both configurations becomes effectively identical. Given the superior packaging flexibility of the bevel gear arrangement, without compromising on weight, the single-stage bevel gearbox was selected as the optimal solution for the main drive system.

13.4 Design Methodology

The gear design process focuses primarily on the stresses experienced by the gear teeth, which must withstand two critical types of loading: tooth bending stress, resulting from the forces exerted as teeth mesh and contact stress. The contact stress arises from the localized pressure as gear teeth come into physical contact during operation. Both stress types are carefully considered in the design of the gearbox, ensuring structural integrity under operational loads. All gears are sized and validated according to AGMA standards, with appropriate safety factors applied to both bending and contact stress limits to ensure reliability and durability in service.

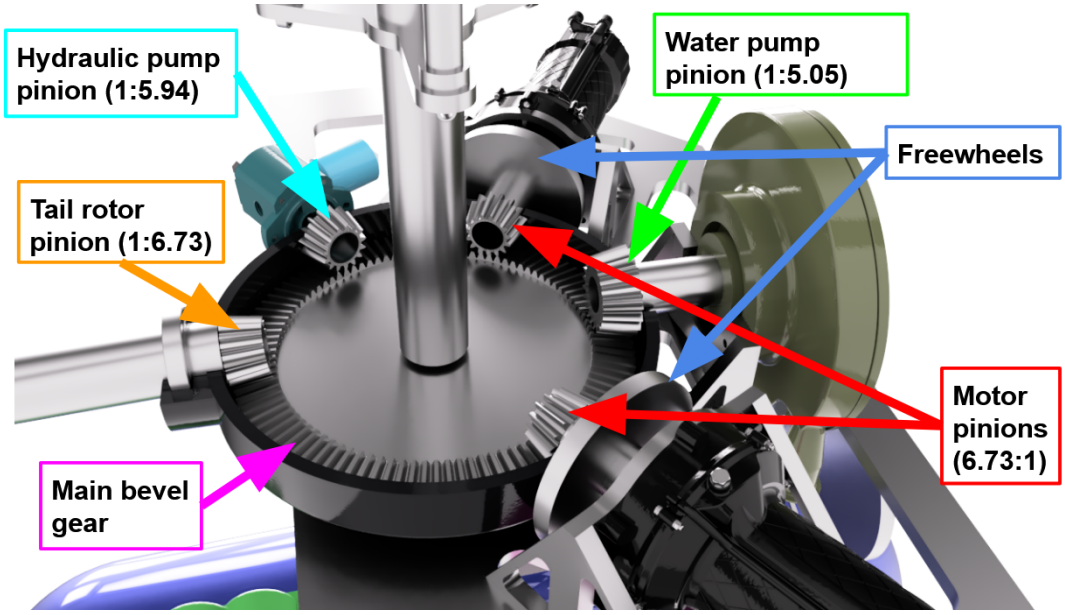

Figure 13.1: *Wyvern* main gear box

13.5 Main Rotor Transmission

13.5.1 Main Rotor Gearbox

Following the initial internal speed reduction, both motors feed into a single-stage bevel gear reduction with a 6.73:1 ratio. This bevel gear not only reduces speed but also redirects the shaft angle by 86.5°to align with the 3.5°tilt of the main rotor shaft, accommodating the horizontally mounted motors within the airframe. The main bevel gear also incorporates three additional pinion outputs: one driving the water pump for the high temperature cooling system, one supplying power to the tail rotor drive shaft, and one driving the hydraulic pump. To ensure safety, the drivetrain includes sprag clutches between each motor and the main gearbox (Figure 13.1). These clutches allow the system to disengage a failed motor, enabling the remaining motor to continue driving the rotor system independently. The main rotor shaft is supported by the stand pipe and lift rods at two bearing locations (Figure 13.2). A lower bearing carries vertical (axial) loads, while an upper bearing restricts lateral movement, effectively transferring bending moments from the rotor shaft into the airframe [68]. This ensures the main gearbox only experiences the driving torque necessary for rotor rotation.

13.5.2 Material Choice and Hunting Ratios

The material chosen for the gears is M50 steel. It exhibits excellent fatigue and high temperature performance, which makes it an ideal choice inside a gearbox. M50 is experimentally shown to have an endurance strength of 1550 MPa (225 ksi)with a 1% failure rate. Therefore, a factor of safety of 4 was applied to the 1% experimental failure rate. CS-27.923 regulations specify a 30-minute OEI test (or one motor inoperative). In OEI conditions, the operating pinion will carry 180 kW (241 hp) instead of the 137.5 kW (184 hp) that the pinion is designed for. With a safety factor of 4, the pinion can withstand this increased power for the 30-minute OEI requirement [69]. Aluminum was chosen as the gearbox housing material due to its light weight and ease of manufacturing.

Tooth numbers on all gears are chosen to be hunting ratios, so that the greatest common factor between the pinion and gear is always 1. These ratios mean that each tooth on the pinion meshes with the same tooth on the gear as little as possible, leading to more evenly distributed wear throughout the gearbox.

Table 13.2: Design parameters for main gearbox bevel gear

Quantity	Gear	Pinion
Number of teeth	15	101
Module (m)	4.5 mm	4.5 mm
Diametral Pitch (P_d)	5.6 in	5.6 in
Face width (F)	49.5 mm (1.95 in)	49.5 mm (1.95 in)
Pressure Angle	20°	20°
Input Torque (T)	537.46 N m (396.4 ft lb)	537.46 N m (396.4 ft lb)
Quality Number	12	12
Size factor for pitting resistance (Z_x)	0.61	0.61
Size factor for bending (Y_X)	0.51	0.51
Crowning factor for pitting (C_{xc})	1.5	1.5
Stress cycle factor for pitting resistance (C_L)	1.01	1.14
Stress cycle factor for bending strength (K_L)	0.94	0.97
Allowable contact stress number (S_c)	1700 MPa (247 ksi)	1700 MPa (247 ksi)
Allowable bending stress number (S_t)	390 MPa (57 ksi)	390 MPa (57 ksi)
Maximum contact stress (σ_c)	1116 MPa (162 ksi)	1116 MPa (162 ksi)
Maximum bending stress (σ_b)	387 MPa (56 ksi)	387 MPa (56 ksi)
Wear Factor of Safety (S_H)	1.52	1.52
Bending Factor of Safety (S_F)	4	4
Weight	9.78 kg (21.56 lbf)	1.56 kg (3.44 lbf)

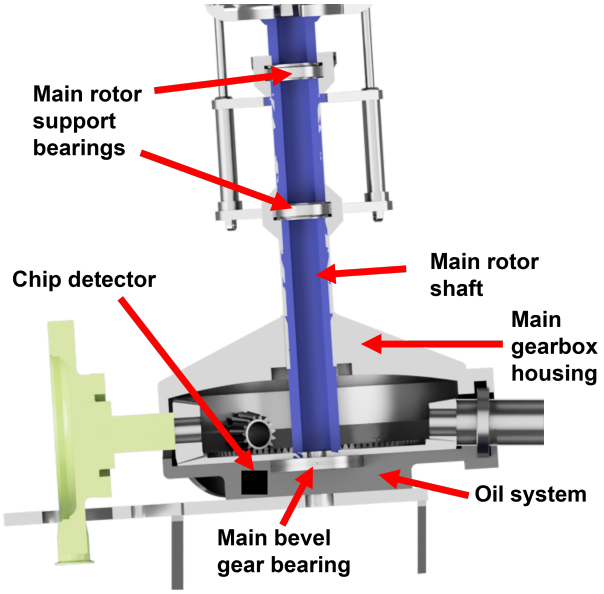

Figure 13.2: Gearbox cutaway

13.5.3 Tail Rotor Transmission

To minimize the weight of the tail rotor drive system, the tail rotor drive shaft operates at the same speed as the motor outputs (maximum 2,437 RPM in hover). Consequently, only a small reduction of 1.27:1 is required at the tail rotor itself. This reduction is accomplished using a single-stage bevel gear, which also redirects the shaft rotation by 90°to match the tail rotor drive plane orientation.

Table 13.3: Design parameters for tail rotor gearbox

Quantity	**Gear**	**Pinion**
Number of teeth	15	19
Module (m)	3 mm	3 mm
Diametral Pitch (P_d)	8.5 in	8.5 in
Face width (F)	36 mm (1.42 in)	36 mm (1.42 in)
Pressure Angle	20°	20°
Input Torque (T)	92.3 N m (67.9 ft lb)	92.3 N m (67.9 ft lb)
Quality Number	12	12
Size factor for pitting resistance (Z_x)	0.62	0.62
Size factor for bending (Y_X)	0.51	0.51
Crowning factor for pitting (C_{xc})	1.5	1.5
Stress cycle factor for pitting resistance (C_L)	1.01	1.03
Stress cycle factor for bending strength (K_L)	0.94	0.95
Allowable contact stress number (S_c)	1700 MPa (247 ksi)	1700 MPa (247 ksi)
Allowable bending stress number (S_t)	390 MPa (57 ksi)	390 MPa (57 ksi)
Maximum contact stress (σ_c)	1015 MPa (148 ksi)	1015 MPa (148 ksi)
Maximum bending stress (σ_b)	175 MPa (25.4 ksi)	175 MPa (25.4 ksi)
Wear Factor of Safety (S_H)	1.67	1.67
Bending Factor of Safety (S_F)	9	9
Weight	0.14 kg (0.31 lbf)	0.15 kg (0.33 lbf)

13.6 Shaft and Belt sizing

The tail rotor drive shaft is segmented into three distinct sections, optimized for both power transmission efficiency and weight reduction. Starting from the main gearbox, the configuration is as follows: the first section is a 1.95 m (6.4 ft) long subcritical shaft, designed to remain below its first critical speed, providing a lightweight and structurally simple solution. Then, a short 0.1 m (0.32 ft) shaft that integrates the belt drive for the radiator fan, facilitating cooling system integration with minimal added mass. Lastly, a 3.95 m long (13 ft) supercritical shaft, chosen specifically to eliminate the need for midspan bearings, thereby reducing overall system weight. All sections of the drive shaft have an outer diameter of 75 mm (2.9 in) and a thickness of 1 mm (0.04 in). These sizes come from the required torque of the tail rotor, the driveshaft is safe for static stress, static strain (twist), and fatigue. The frequencies were then tuned by varying the lengths and adding bearings where necessary. The supercritical driveshaft is designed to operate within the frequency range bounded by its first and second bending mode natural frequencies. The operational speed range extends from 1219 RPM (50% of nominal hover speed) to 2681 RPM (110% of nominal hover speed). To ensure adequate separation from critical speeds, a 15% safety margin is applied to this range, resulting in operational frequency bounds of 17.27 Hz and 51.39 Hz. The natural frequencies of the shaft are determined based on its geometric and material properties. For an aluminum shaft with a diameter of 75 mm (2.9 in), a wall thickness of 1 mm (0.04 in), and a length of 3.95 m (13 ft), the first and second bending mode natural frequencies are calculated to be 13.41 Hz and 53.65 Hz, respectively. As such, the shaft operates entirely within the supercritical regime, between its first and second natural frequencies, throughout all phases of flight. Although a midspan damper is required to manage vibrations as the shaft passes through its first critical speed, this damper adds only 0.25 kg (0.55 lbs) of mass, significantly less than the mass penalty of a conventional midspan bearing, which would add 1 kg of mass if placed in the same location. The total driveshaft now only has 3.7 kg (8.1 lbf) of mass. With dampers and bearings included, the tail rotor drive shaft adds 7.9 kg (17.4 lbf) of mass to the aircraft.

The HTC system radiator fan requires a relatively low 2 kW of power and is conveniently positioned directly beneath the tail rotor drive shaft. Given this favorable placement, a belt drive system was selected as the

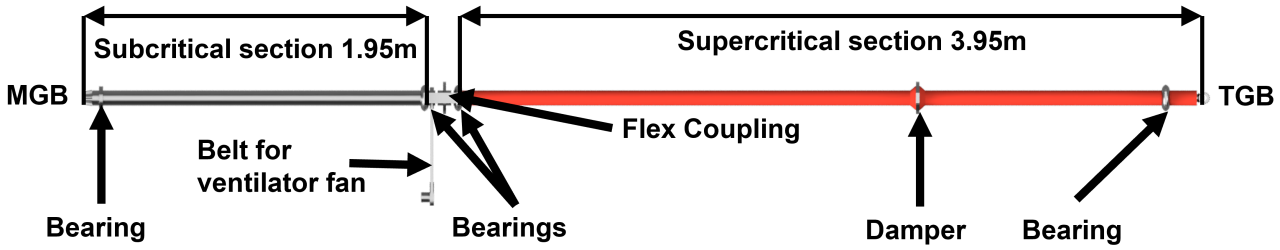

Figure 13.3: Driveshaft diagram

most efficient and lightweight method of power transmission. Specifically, an Optibelt SPZ V-belt, chosen from the Optibelt product catalog, was selected for its suitability. This belt provides a 1.42:1 reduction ratio, aligning with the fan's operational requirements. The system requires a tension force of 118 N and contributes a minimal 0.1 kg (0.22 lbf) of additional mass.

13.7 Oil System

All gear interfaces, including the main motor pinions, the tail rotor pinion, the water pump pinion, and the hydraulic pump pinion, are equipped with dedicated oil spray nozzles to ensure continuous lubrication. Lubricant accumulates in the sump at the base of the gearbox housing, from which it is routed through a magnetic chip detector, oil cooler, and filtration unit. Following this cycle, dual oil pumps recirculate the oil back to the spray nozzles to maintain system performance. The gear components are manufactured from M50 steel, selected for its high fatigue strength. It also has very good high-temperature performance, with an operational limit of up to 425°C (800°F). This material specification supports compliance with CS-27.923 regulations by enabling up to 30 minutes of dry-running operation without critical damage [70].

14 Avionics System

Wyvern is equipped with a modern glass cockpit that prioritizes situational awareness and pilot usability. Operations are conducted under Visual Flight Rules (VFR) and the avionics suite is streamlined accordingly. The overall layout of the avionics is shown in Figure 14.1. A key subsystem within the avionics architecture is the Engine Monitoring System (EMS), custom-developed for *Wyvern* to support the unique requirements of its PEMFC propulsion system. The entire cockpit design reflects a balance between human factors engineering and mission-specific functionality for reduced pilot workload.

Figure 14.1: *Wyvern* avionics panel

14.1 Cockpit Layout

The primary mission specified in the RFP is to loiter above the Alligator River, NC, to observe alligators. Accordingly, the cockpit is designed to maximize the passenger viewing experience by minimizing visual obstructions, while also ensuring the pilot has an optimal field of view (FOV) for both situational awareness and mission performance. Human factors considerations play a critical role in the design of the cockpit layout and seat positioning to support comfort, accessibility, and visibility.

All avionics are centrally located in a compact instrument positioned in the middle of the cockpit, as summarized in Table 14.1. The cockpit is configured around the design eye point, and the pilot seats are adjustable to accommodate a range of body sizes, from the 5th percentile female to the 95th percentile male, in accordance with ergonomic design standards [71]. The overall view of the cockpit is shown in Figure 14.2.

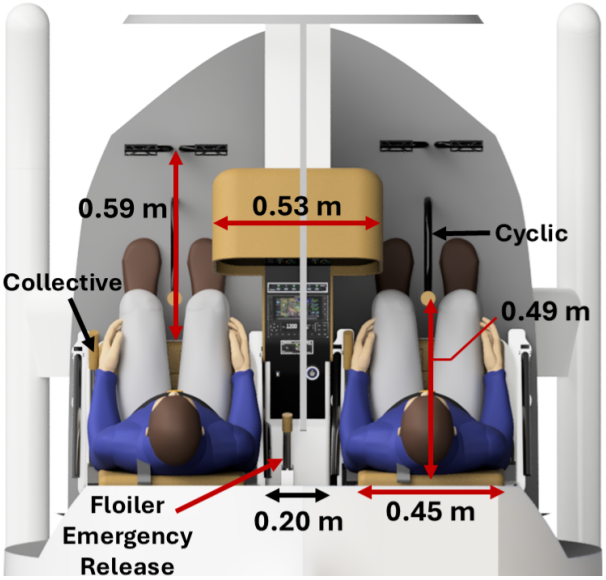

Figure 14.2: *Wyvern* cockpit layout

14.2 Engine Monitoring System

Since no existing EMS is tailored for PEMFC-powered eVTOL aircraft, a custom system was developed for *Wyvern* as shown in Figure 14.3.

The adoption of a PEMFC introduces new parameters to monitor, such as stack temperature, hydrogen pressure, and fuel cell voltage stability. To prevent information overload and reduce pilot workload, the EMS was designed to prioritize and clearly present only the most critical information, enhancing situational awareness during flight. To support this, a First Limitation Indicator (FLI), which is a system commonly used in conventional turbine-powered helicopters, was adapted for *Wyvern*. FLI simplifies decision-making by displaying only the most limiting engine parameter in real time, meaning the parameter that is closest to reaching its operational limit. For *Wyvern*, the FLI now highlights the most limiting PEMFC and electric engine related parameter in real time, such as power and temperature for motors 1 and 2, and PEMFC pressure, instead of the traditional turbine metrics. Functionally, *Wyvern*'s FLI operates in the same way as conventional systems. However, when PEMFC pressure becomes the limiting factor, both needles move together since a single fuel cell stack powers both motors.

In addition to the FLI, PEMFC, and Battery states are also shown. For each propulsion unit, the output power, remaining H2, battery State of Charge (SoC), and corresponding temperatures are presented. Other states for PEMFC and battery are rather shown as a warning light instead of there actual state as a number. Thus, the warning lights **FC Cooling** and **Batt Cooling** on the top right indicate failure of the PEMFC and battery coolant system. **Air Fan** indicates an air intake fan for the PEMFC cathode failure. **H2** indicates the leakage of hydrogen from either of the two hydrogen tanks. Lastly, the usual indicators (rotor speed, rotor power, remaining flight time) are present as well.

14.3 Stability Augmentation System

To reduce pilot workload and enhance handling qualities, a Stability Augmentation System (SAS) is integrated into the aircraft. Despite the added weight and power consumption, the system provides significant

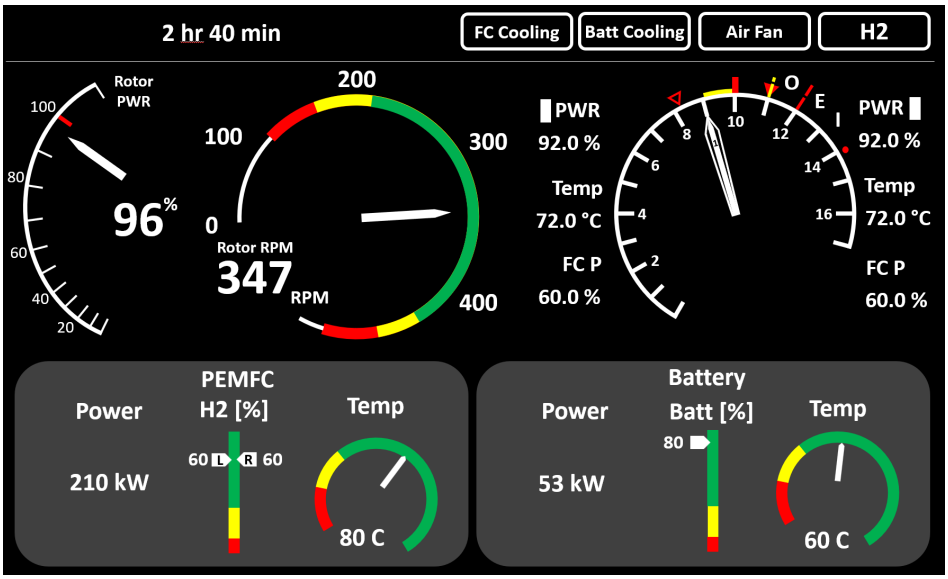

Figure 14.3: *Wyvern* Engine monitoring system (EMS)

benefits to pilot performance and overall flight safety, making it a worthwhile inclusion. SAS control interfaces are located both on the cyclic stick and the avionics panel, allowing for intuitive and accessible operation. The detailed control architecture and SAS integration strategy are discussed in Section 16.4.

14.4 Power Distribution

The avionics are powered by a 14 V bus, including the radios, cockpit displays, and flight computers. The avionics bus takes power from the flight battery via a small DC/DC converter. Another DC/DC converter boosts the bus voltage to 28V to power the SAS actuators. In the event of a flight battery failure, a separate avionics battery can power critical flight instruments for up to 30 minutes.

14.5 Avionics Summary

Table 14.1 provides a detailed list of avionic systems for *Wyvern* with the specific model, weight, power, and cost. The selected components have a total weight of 13.62 kg (30 lb) and a maximum power usage of 1.2 kW. Most of the power is required by SAS, but it includes the power for the electronic servo.

Table 14.1: Avionics list

Component	Model	Qty	Weight (kg)	Maximum Power (W)	Cost (USD)
SAS	HeliSAS	1	5.44	1000	40,989
PFD/MFD	G500H Txi	2	4.04	140	–
COM/NAV/GPS	GTN 650Xi	1	2.48	37.8	13,995
Transponder / Encoder	GTX 335 / GAE 12	1	1.32	15	3,538
Intercom	PM1000II	1	0.342	3.5	537
Total	–	**6**	**13.6**	**1,196**	**59,059**

14.6 Health and Usage Monitoring System

The onboard Health and Usage Monitoring System (HUMS) is a vital component for ensuring the reliability, safety, and maintainability of *Wyvern*. While HUMS is traditionally found on larger aircraft, this

system has been specifically adapted to balance essential monitoring capabilities with the weight and cost constraints of a smaller platform. The flowchart is shown in Figure 14.4.

Key helicopter components are equipped with sensors such as accelerometers and temperature sensors, strategically positioned to capture critical data on structural and mechanical loads. The HUMS supports both real-time (online) and post-flight (offline) monitoring. The online system continuously tracks parameters such as rotor shaft torque, PEMFC and motor temperatures, battery voltages, and power consumption of auxiliary systems. Any anomalies are flagged instantly, enabling prompt intervention. The offline system stores long-term usage data, including component fatigue cycles and strain histories, which is used for trend analysis and to forecast future maintenance needs, such as scheduling overhauls. If a potential fault or maintenance need is detected, the system immediately alerts the pilot. Additionally, all data can be checked post-flight for in-depth analysis by maintenance crews.

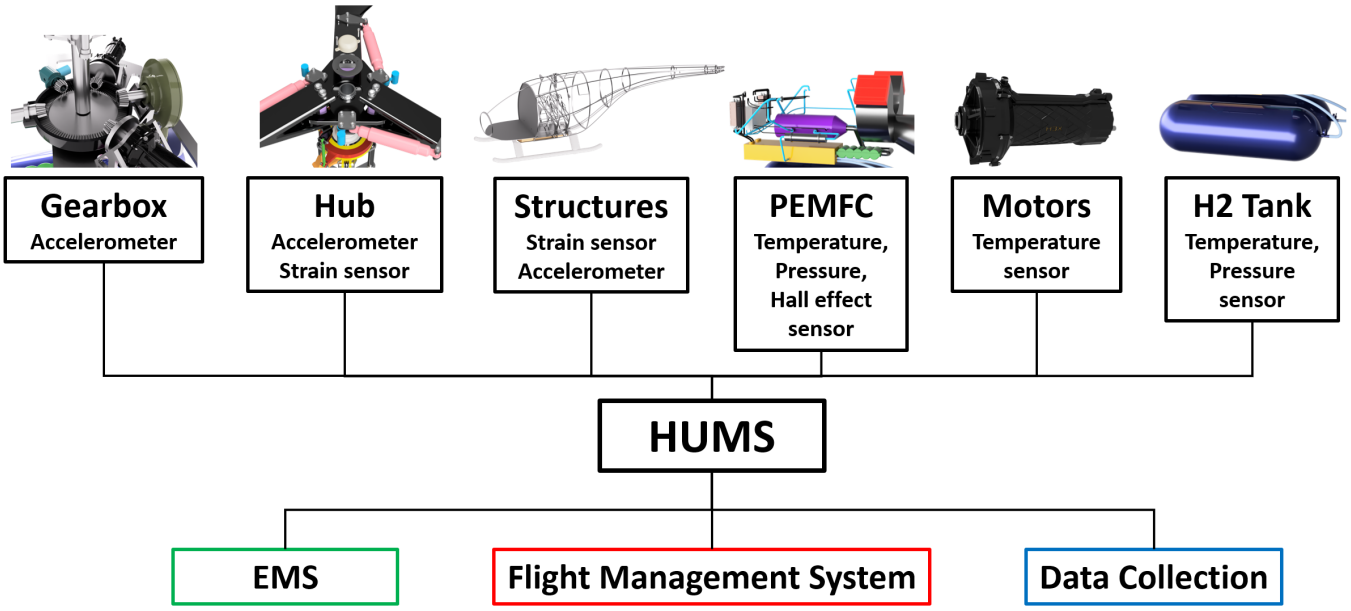

Figure 14.4: Health and usage monitoring system flowchart

15 Weight and Balance

Component group weights were initially sized using the Tischenko and AFDD [23] models to inform initial analysis. These estimates were refined with CAD-based calculations, which also provided accurate estimates of the *Wyvern* center of gravity. A component-level weight breakdown is discussed in Table 15.1.

The hydrogen propulsion system provides a unique benefit versus similarly sized helicopters with conventional propulsion systems in that the fuel mass fraction is significantly lower. Combined with the hydrogen tanks' center of gravity being positioned very close to the vehicle's overall center of gravity at gross takeoff weight results in minimal longitudinal and lateral CG shift. Figure 15.1 illustrates the longitudinal, lateral, and vertical CG displacement due to weight changes throughout the mission. The displacement is observed primarily in the vertical and longitudinal directions and remains within 5 mm. Since the CG of the hydrogen tanks is located behind and below the initial CG, the overall CG moves forward and upward relative to its initial position as hydrogen is consumed during the mission.

Table 15.1: Vehicle weight breakdown

Component	Weight, kg (lb)
Fuselage	**347.0 (765)**
Airframe	272.0 (600)
Honeycomb	5.0 (11)
Skin	45.0 (99.2)
Landing Gear	25.0 (55.1)
Propulsion System	**711.5 (1568)**
PEMFC	127.5 (281.1)
PEMFC Air Intake	8.00 (17.6)
Air Intake Duct	0.5 (1.1)
Humidifier	10.0 (22.0)
DC/DC Converters	22.0 (48.5)
Flight Battery	31.5 (69.4)
Electrical Wires	25.1 (55.3)
Coolant	30.0 (66.1)
Coolant Tank	2.0 (4.4)
Coolant Pump	1.92 (4.2)
Coolant Tubing	4.0 (8.8)
Deionizer	2.0 (4.4)
Radiators	15.0 (33.1)
Radiator Fan	1.0 (2.2)
Radiator Ducting	6.0 (13.2)
Hydrogen Tanks	424.0 (934.8)
Hydrogen Tubing	1.0 (2.2)
Main Rotor	**166 (366)**
Articulated Hub	40 (88.2)
Main Rotor Blades	60 (132.2)
Hydraulic Actuators	5.0 (11)
Rotor Structure	61.0 (134)
Tail Rotor	**20.0 (44.1)**
Teetering Hub	5.5 (12)
Tail Rotor Blades	5.0 (11)
Horizontal Stabilizer	**5.85 (12.9)**
Frame	3.79 (8.35)
Skin	2.06 (4.54)
Vertical Stabilizer	**9.6 (21.2)**
Frame	5.20 (11.5)
Skin	4.4 (9.7)
Transmission	**58.5 (129)**
Gears and Bearings	22.5 (49.6)
Shafts	4.00 (8.82)
HPDM-180 Motors	32.0 (70.5)
Wing	**120 (264.6)**
Spars and Ribs	65.0 (143)
Aileron Ribs	3.00 (6.61)
Aileron Mechanism	22.0 (48.5)
Skin	30.0 (66.1)
Total Empty Weight	**1438 (3170)**
Payload	**185 (407.9)**
Pilot	80.0 (176)
Passenger	80.0 (176)
Cargo	25.0 (55.1)
Fuel	**24.8 (54.6)**
GTOW	**1648 (3633)**

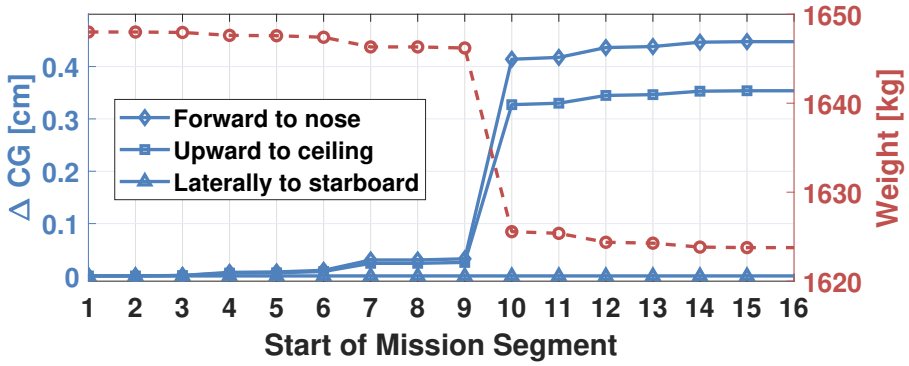

Figure 15.1: CG evolution during the mission

16 Flight Dynamics and Controls

The lift-compound configuration of *Wyvern*, optimized for long-endurance missions, incorporates a large fixed wing to offload a significant portion of lift during forward flight—up to 60% during cruise. As a result, the vehicle exhibits characteristics of both fixed-wing aircraft and rotorcraft. Despite this hybrid

nature, *Wyvern* retains a streamlined control architecture centered on the primary rotorcraft effectors: main rotor collective, longitudinal and lateral cyclic, and tail rotor collective. The design intentionally avoids redundant or non-essential control surfaces to minimize weight, complexity, and cost. Instead, it relies on the core rotorcraft controls, sufficient for full-envelope maneuverability and stability, even in the presence of fixed-wing aerodynamic interactions.

16.1 Flight Dynamics Simulation Model

The flight dynamics simulation model is based on an in-house code developed and implemented in MATLAB, containing a 6-DoF rigid-body dynamic model of the fuselage, nonlinear aerodynamic lookup tables for the rotor blades, wing, and empennage, rigid flap rotor blade dynamics, and a three-state Pitt-Peters inflow model [72] for the main rotor. The rotorcraft flight dynamics are formulated as a nonlinear time-invariant system:

$$\dot{\boldsymbol{x}} = \boldsymbol{f}(\boldsymbol{x}, \boldsymbol{u}) \tag{7a}$$

$$\boldsymbol{y} = \boldsymbol{g}(\boldsymbol{x}, \boldsymbol{u}) \tag{7b}$$

where $\boldsymbol{x}$ is a state vector, $\boldsymbol{u}$ is a control vector, and $\boldsymbol{y}$ is an output vector. The state vector contains the usual 9 rigid body states $[u\ v\ w\ p\ q\ r\ \phi\ \theta\ \psi]$, 3 position states $[x\ y\ z]$, 4 flapping states and 4 lagging states in multiblade coordinates and their derivatives $[\boldsymbol{\beta}\ \boldsymbol{\zeta}\ \dot{\boldsymbol{\beta}}\ \dot{\boldsymbol{\zeta}}]$, and 3 dynamic inflow state for the main rotor $[\lambda_0\ \lambda_{1c}\ \lambda_{1s}]$ and one uniform inflow state for the tail rotor $[\lambda_{0_t}]$. The control inputs are:

$$\boldsymbol{u}^T = [\delta_{\text{lat}}\ \delta_{\text{lon}}\ \delta_{\text{col}}\ \delta_{\text{ped}}]$$

where δ_{lat} and δ_{lon} are the lateral and longitudinal cyclic inputs, δ_{col} is the collective input, and δ_{ped} is the pedal input.

The model is then linearized by trimming the rotorcraft flight dynamics at a required flight condition by mission using perturbation methods [73].

For longitudinal trim in the long-endurance loiter segment, it was deemed desirable to reduce the β_{1c} to decrease the rotor and mast fatigue. Placing the rotor pivot behind the CG tends to reduce the required β_{1c} angle for longitudinal trim, because the rotor thrust line creates a nose-down pitching moment, which can be balanced with a smaller rotor flapping angle. However, this tends to increase the aircraft pitch down angle α_s, increasing the flat plate area of the vehicle. This can be mitigated by already having a rotor pre-shaft tilt (α_{ss}). However, the requirement of a manned mission as well as detrimental rotor cruise efficiency restricted the α_{ss} for *Wyvern*, and a balance was to be made for α_s and β_{1c} at V_{be} to prioritize both aerodynamic efficiency, fatigue, structural constraints, and realism. Hence, the rotor pre-shaft tilt was set to be at 3.5°. This tilt facilitated the *Wyvern* architecture to minimize the forward flight longitudinal flapping. β_{1c} varies over the varying distance between the vehicle CG and the main rotor shaft pivot point in loiter at V_{be} for a fixed α_{ss}. Theoretically, the β_{1c} can be reach to zero, but due to the structural constraint, the rotor pivot point is installed 0.03 m behind the vehicle CG.

Figure 16.1 shows the required control inputs across all flight segments. Since the only depleting vehicle fuel is gaseous hydrogen, occupying only 1.6% of the GTOW, the vehicle's weight remains relatively constant throughout the mission, resulting in minimal variation in collective pitch at the end of the mission compared to the beginning of the mission. Notably, the loiter and cruise segments require significantly less tail rotor collective input, primarily due to the vertical stabilizer off-loading the tail rotor. Especially in loiter, the vehicle is loitering with 5 °roll angle in 2 km x 2 km constraint. Additionally, during steady descent, where the vehicle operates at its highest speed, the tail rotor collective is at its lowest, reflecting reduced anti-torque demands.

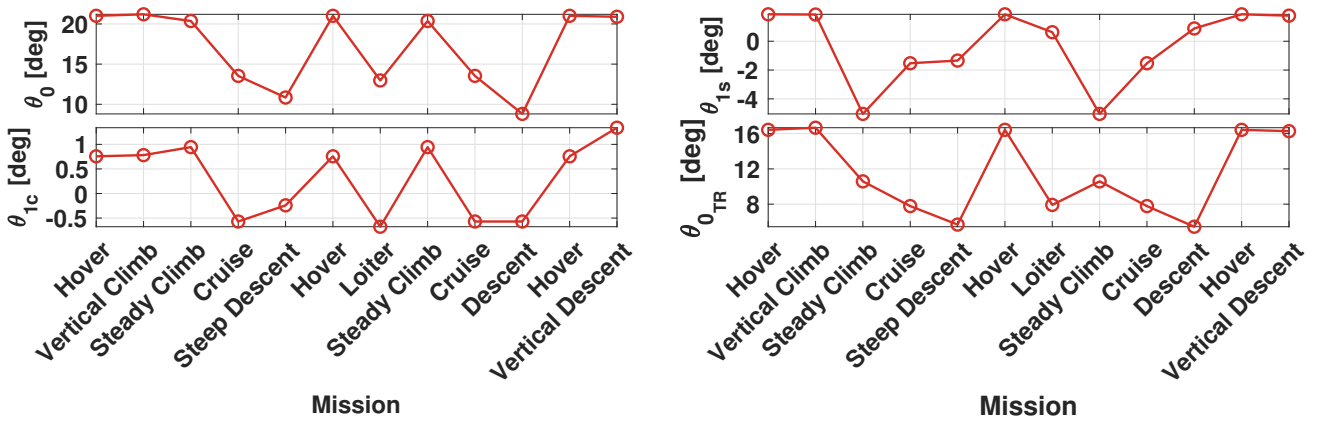

Figure 16.1: Control inputs for the mission segments

16.2 Static Stability

The flight envelope of *Wyvern*, as specified by the RFP, includes several steady flight conditions: hover, steady climb and descent, cruise, and loiter. Thus, the vehicle must return to a trim condition after a velocity of angular rate perturbation. Since *Wyvern* is a lift-compound helicopter, the adjustment of stability surfaces and the main wing was the key design feature to ensure the static stability.

16.2.1 Longitudinal Static Stability

The static longitudinal stability of *Wyvern* is governed by the combined contributions of the main wing, the horizontal stabilizer, and the rotor. In conventional single-main-rotor (SMR) designs, the horizontal stabilizer is primarily needed to counteract the destabilizing moment from the fuselage. However, in *Wyvern*, the moment contribution from the main wing exceeds that of the fuselage. As a result, the horizontal stabilizer plays a more significant role in restoring stability. Moreover, because the rotor pivot point is located aft of the center of gravity (CG), its destabilizing moment must also be considered. To ensure adequate longitudinal static stability, the horizontal stabilizer was sized with an area of 1.30 m^2 and set at a 2-degree incidence angle using the selected airfoil. The rotorcraft longitudinal static stability is also reflected at M_u and M_w, which represent longitudinal static stability with speed and angle of attack, respectively. $M_u > 0$ in hover shows that the main rotor contributes to the longitudinal static stability. $M_w \approx 0$ shows that no pitching moment is induced in hover with gust perturbation in the vertical speed.

16.2.2 Lateral Static Stability

Lateral static stability is primarily influenced by the vertical stabilizer. Another important factor is the wing dihedral effect. *Wyvern* features a unique configuration that has a box wing with a 6-degree dihedral angle on the lower wing and a 4-degree anhedral angle on the upper wing. Although the dihedral angle is larger, the CG is located closer to the aerodynamic center of the dihedral (lower) wing, resulting in a shorter moment arm. In contrast, the anhedral (upper) wing has a longer moment arm, making its destabilizing effect more dominant. Consequently, the overall lateral static stability is slightly reduced due to the anhedral effect. This reduction was evident in the roll subsidence mode, where the mode's damping decreased, causing it to slow by approximately 0.4 rad/s. For the rotorcraft longitudinal static stability, L_v reflects that the main rotor produces a moment in the opposite direction of the disturbance in hover. In Table 16.1, L_v is negative, which means statically stable in the lateral direction.

16.3 Dynamic Stability

With trimmed and linearized conditions established in hover and loiter segments, dynamic stability was analyzed using the eigenvalues of the state matrix. To gain physical insight, the order of the linear model is reduced by residualization [74], and then the system was approximated to decouple into longitudinal and lateral modes, isolating the natural motion characteristics.

A unique aspect of *Wyvern* is its large lifting surfaces and low main rotor rotational speed, which contribute significantly to overall stability. Placement of the wing played a crucial role. By locating it aft of the center of gravity (CG), the wing generates a stabilizing pitch-down moment in response to disturbances such as upward gusts, enhancing dynamic stability. Table 16.1 presents the corresponding stability derivatives for both hover and loiter conditions.

Figure 16.2 shows the decoupled eigenvalues in hover and loiter. In hover, *Wyvern* exhibits typical rotorcraft behavior, with an unstable phugoid mode and a marginally stable Dutch roll mode, indicating the need for active pilot regulation. The coupled eigenvalues in Figure 16.3 reveal pitch and roll subsidence coupling, which results from a higher longitudinal moment of inertia (I_{xx}) compared to the lateral moment of inertia (I_{yy}).

In loiter, the impact of reduced rotor rotational speed and lift sharing becomes apparent. The pitch short period mode is slower than that of traditional helicopters due to reduced rotor control authority, as the rotor is the only control surface. However, the large lifting surfaces produce a faster roll subsidence mode, dominated by the stability derivative L_p, unlike conventional rotorcraft. Additionally, the yaw subsidence mode transitions into a spiral subsidence mode, further highlighting the aerodynamic influence of the fixed wings during forward flight.

Table 16.1: Key stability derivatives of *Wyvern* in Hover and Loiter

Derivatives	Hover	Loiter	Units	Derivatives	Hover	Loiter	Units
X_u	-0.0109	-0.0504	1/sec	L_p	-0.5065	-4.7758	1/sec
M_u	0.0033	0.0433	rad/sec-m	Z_q	0.0402	28.8032	m/rad-sec
X_w	0.0138	0.0287	1/sec	L_r	0.0163	1.6843	1/sec
M_w	-0.0042	-0.2693	rad/sec-m	Y_v	-0.0275	-0.2471	1/sec
X_q	0.5776	2.4865	m/rad-sec	N_v	0.0248	0.0168	rad/sec-m
M_q	-0.6839	-1.0620	1/sec	Y_p	-0.5709	-2.6054	m/rad-sec
Z_u	-0.0076	-0.4850	1/sec	N_p	-0.0296	-0.1385	1/sec
L_v	-0.0052	-0.0275	rad/sec-m	Y_r	0.0679	-28.8488	m/rad-sec
Z_w	-0.2073	-1.9113	1/sec	N_r	-0.1828	-0.1930	1/sec

16.4 Flight Controls

Wyvern is a hydrogen-powered rotorcraft designed with safety as a top priority. While modern trends favor fly-by-wire (FBW) control systems for their flexibility and advanced functionality, they also introduce risks associated with system malfunctions. Incorporating redundant flight computers can mitigate these risks, but adds significant weight, an important constraint for a long-endurance, hydrogen-powered platform. To balance reliability and weight, *Wyvern* employs a traditional mechanical control system, ensuring direct pilot authority and minimizing potential points of failure. However, during extended loitering operations within a constrained 2 km x 2 km area, pilot workload can become substantial. To alleviate this, a stability augmentation system (SAS) is integrated into the control architecture, providing active assistance with attitude stabilization, thereby reducing pilot workload and enhancing handling precision during critical mission phases.

The stability augmentation system (SAS) integrated into *Wyvern* is a four-axis control augmentation

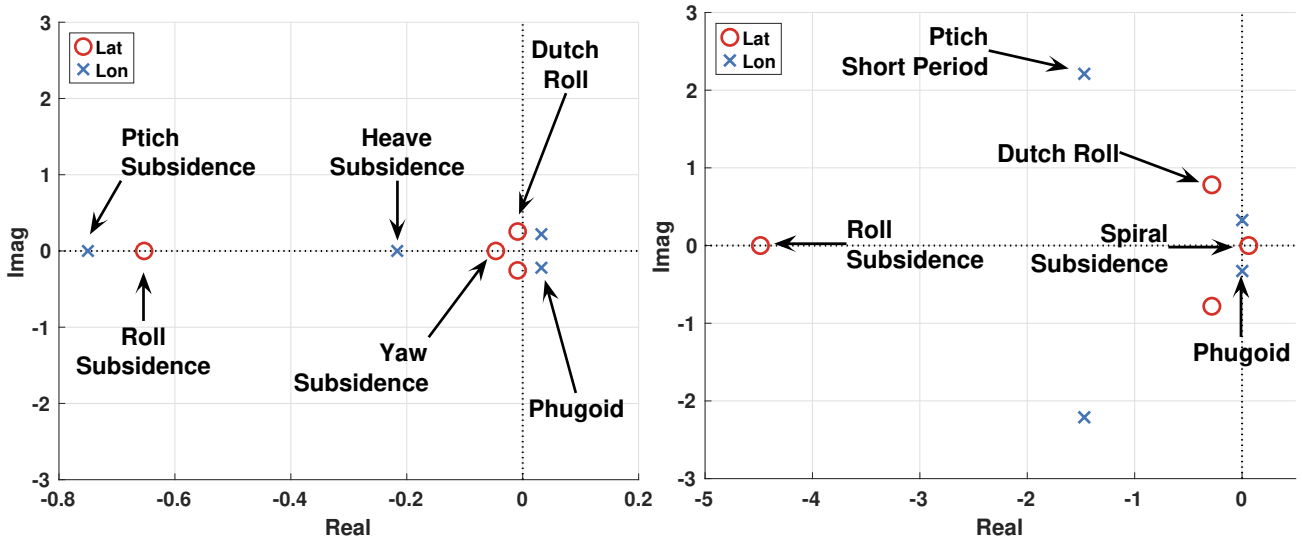

(a) Hover (b) Loiter

Figure 16.2: Decoupled stability roots for *Wyvern* in hover and loiter

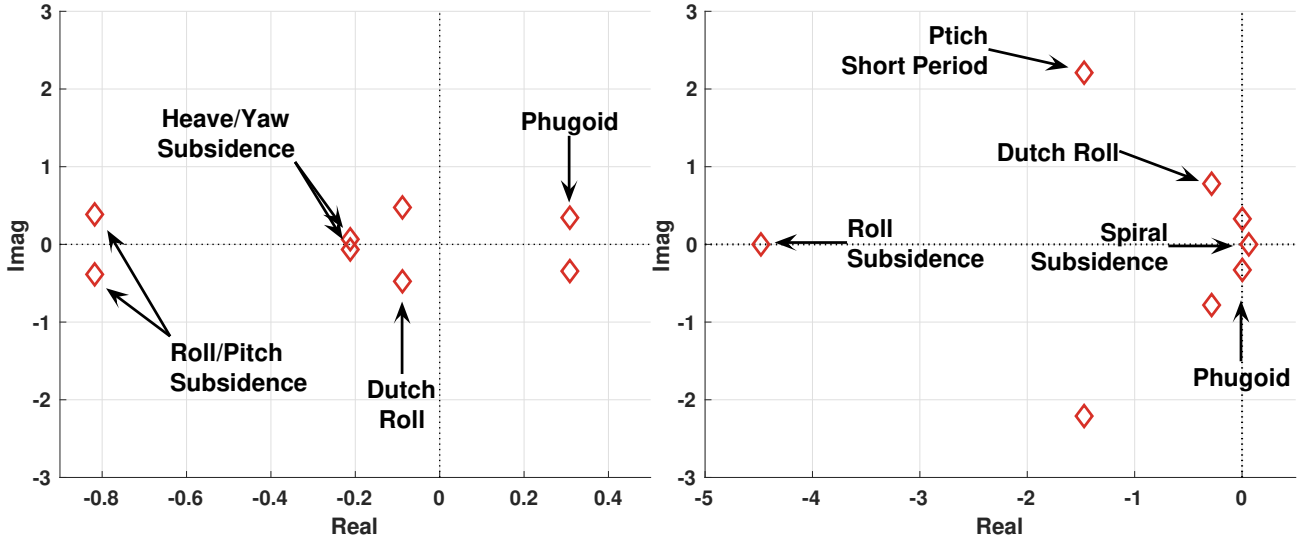

(a) Hover (b) Loiter

Figure 16.3: Coupled stability roots for *Wyvern* in Hover and Loiter

system designed to enhance pitch, roll, yaw, and collective control. It features multiple selectable modes tailored to different phases of flight, including attitude hold, vertical speed hold, altitude hold, heading hold, and navigation tracking. The SAS actuators are installed in parallel with the mechanical control rods, preserving direct pilot authority and enabling manual override at any time in the event of a malfunction or when manual control is preferred.

To support these functionalities, *Wyvern* employs a layered control architecture. The inner loop uses Attitude Command Attitude Hold (ACAH) for pitch and roll, and Rate Command Direction Hold (RCDH) for yaw, providing stable and intuitive handling. The outer loop incorporates Translational Rate Command (TRC) for longitudinal and lateral axes, allowing the pilot to command translational velocity directly rather than attitude, which greatly simplifies control during prolonged loiter operations. This integrated SAS architecture significantly reduces pilot workload in long-endurance loiter, enhances precision during mission-critical phases, and improves overall handling qualities across the flight envelope.

17 Vehicle Performance

Excellent loiter efficiency without compromising hover was the principal goal for *Wyvern*.

17.1 Component wise Drag Estimation

Wyvern's total drag comprises parasitic and wing-induced components. Flat plate areas of individual elements were estimated using both Prouty's method [75] and CFD simulations via the in-house HAMSTR [44] and ANSYS-FLUENT solvers. To validate the estimation approach, Prouty's method was first applied to the R44 helicopter, with results summarized in Table 17.1 and compared to known flat plate area data [76]. Following Prouty's guidance, a 20% increment was added to the parasitic drag area for conservatism, along with a 10% miscellaneous drag factor accounting for antennas, pitot probes, and small structures.

Table 17.1: Flat plate area breakdown for R44

Component	**Loiter Flat Plate Area**			
	Drag Estimation [75]		**Flight Test [76]**	
	m^2	**ft^2**	**m^2**	**ft^2**
Fuselage	0.132	1.421		
Main Rotor Hub	0.109	1.171		
Tail Rotor Hub	0.0141	0.151		
Landing Gears	0.955	1.028		
Horizontal Stabilizer	0.00382	0.0411		
Vertical Stabilizer	0.00551	0.0593		
Miscellaneous (10%)	0.0360	0.387		
Interference (20%)	0.0491	0.852		
Total	**0.475**	**5.112**	**0.441**	**4.75**

From Table 17.1, Prouty's method estimates the R44 flat plate area within 8% error. Subsequently, drag estimations and CFD simulations were performed for *Wyvern* during loiter at 30 m (98.4 ft) MSL and $V_{be} = 29.3$ m/s (57 knots). Table 17.2 presents the component-wise results. The estimated parasitic drag area for *Wyvern* was calculated as 0.58 m^2 (6.24 ft^2).

Table 17.2: Flat plate area breakdown for *Wyvern* at loiter.

Component	**Flat Plate Area at loiter**			
	Estimation		**CFD**	
	m^2	**ft^2**	**m^2**	**ft^2**
Fuselage	0.160	1.717	0.136	1.464
Main Rotor Hub	0.131	1.415	0.117	1.259
Tail Rotor Hub	0.0189	0.204		
Landing Gear	0.112	1.206	0.0980	1.055
Horizontal Stabilizer	0.0118	0.127		
Vertical Stabilizer	0.00821	0.0884		
Miscellaneous (10%)	0.0452	0.486		
Interference (20%)	0.0994	1.070		
Box Wing (profile only)	0.0586	0.631	0.0456	0.498
Box Wing Interference (20%)	0.0117	0.126		
Total w/o wing	**0.58**	**6.24**		
Total w/ wing	**0.65**	**7.04**		

17.1.1 Aerodynamics of Fuselage

Wyvern's fuselage underwent an iterative aerodynamic optimization process. The baseline design exhibited flow separation, swirl, a sharp nose, and a discontinuous cabin-to-tail transition, as shown in the pressure coefficient distributions in Figure 17.1(a).

A second iteration (Figure 17.1(b)) introduced three key improvements: (1) a rounded nose to reduce stagnation and pressure drag, (2) a smoother cabin-to-tail transition to minimize separation, and (3) a sharper tail boom termination for improved flow attachment. These changes significantly reduced drag and fuselage-induced download. Specifically, the drag coefficient decreased from 0.063 in Model 1 to 0.037 in Model 2 (exhaust off), and the lift coefficient increased (became less negative) from –0.15 to –0.083.

To further enhance fidelity, an additional case included radiator exhaust flow at the fuselage contraction. As shown in Figure 17.2, the exhaust reduces swirl and improves flow alignment aft of the fuselage. This modification yielded further improvements: the drag coefficient dropped to 0.033 and the lift coefficient improved to –0.064, underscoring the aerodynamic benefit of incorporating exhaust effects.

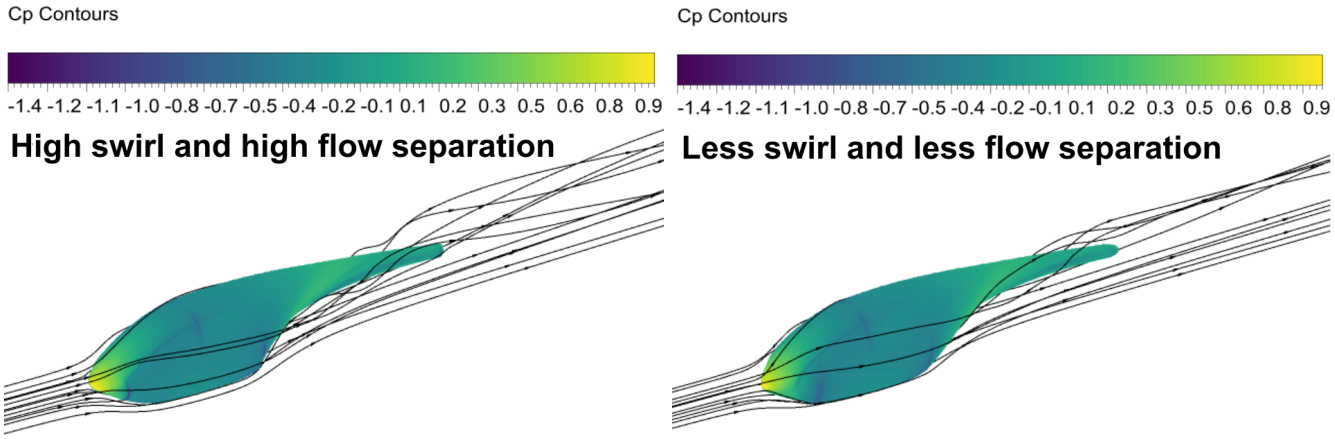

(a) Initial fuselage model.

(b) Optimized fuselage model.

Figure 17.1: Flow streamlines (including pressure coefficient) for two fuselage models at V_{be} at zero pitch.

17.1.2 Aerodynamics of Hub Fairing

The rotor hubs are a significant contributor to the overall drag of the rotorcraft. To mitigate this major drag, the rotor hub is enclosed in a fairing designed to smooth the airflow around it. CFD simulations, as shown in Figure 17.4(a), were performed to estimate its drag. The resulting flat plate area, Table 17.2, indicates an efficient aerodynamic design.

17.1.3 Wing and Empennage

The drag of the wing and empennage was estimated using their wetted surface areas along with detailed aerodynamic data for the selected airfoils (Figure 9.3). The FX 63-120 airfoil was chosen for the box wing configuration, while the DAE11 airfoil was used for both the horizontal and vertical stabilizers. To account for three-dimensional aerodynamic effects, corrections based on the Oswald efficiency factor and aspect ratio were applied. The flat plate area values captured the aerodynamic efficiency of the wing and empennage configurations.

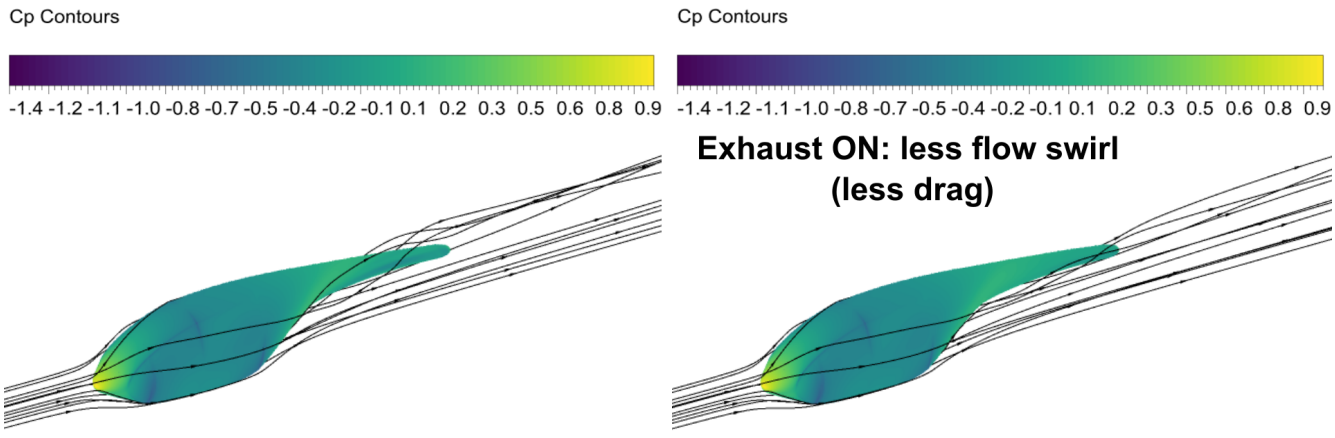

(a) Exhaust OFF.

(b) Exhaust ON.

Figure 17.2: Flow streamlines (including pressure coefficient) for final fuselage model at V_{be} at zero pitch w/o and w/ exhaust being used.

17.1.4 Aerodynamics of the Landing Gear

For *Wyvern*, a skid-type landing gear was selected. Two cross-tube geometries were evaluated: an elliptical profile and a symmetric airfoil shape. Dimensions were determined via finite element analysis (FEA) to ensure structural adequacy. Figure 17.3 compares velocity contours around both configurations, showing that the airfoil-shaped bracket significantly reduces flow separation relative to the elliptical design. CFD drag comparisons confirmed this benefit: the flat plate area of the elliptical cross-tube (Model 1) was 0.202 m^2 (2.178 ft^2), whereas the airfoil-shaped cross-tube (Model 2) reduced the flat plate area to 0.112 m^2 (1.206 ft^2), nearly halving the aerodynamic drag footprint.

To balance structural and aerodynamic requirements, *Wyvern* retains the elliptical cross-tube for structural consistency, enhanced with an external symmetric airfoil fairing. Structural analysis of the elliptical tube will be discussed in a later section. Figure 17.4(b) shows pressure contours and streamlines at V_{be}, zero pitch, indicating low flow separation and streamlined flow around the landing gear.

17.2 Hover Download

Rotor downwash is a significant factor in hover, particularly in lift-compound configurations where both the fuselage and wings are subjected to rotor-induced downwash. This effect is even for performance detrimental to PEMFC propulsion, requiring a much heavier stack. To maintain sufficient lift in hover, the rotor must not only support the gross takeoff weight but also compensate for the additional download caused by this downwash. These effects were quantified by integrating the local drag coefficient over the sectional area of the affected surfaces. The estimated download was approximately 6% of the gross takeoff weight for a single main rotor setup and 10% for the lift-compound box-wing configuration. In the current box wing design, floilers are deflected downward during hover to further reduce the effective wing download, lowering it from 10% to approximately 8.5% of the gross takeoff weight.

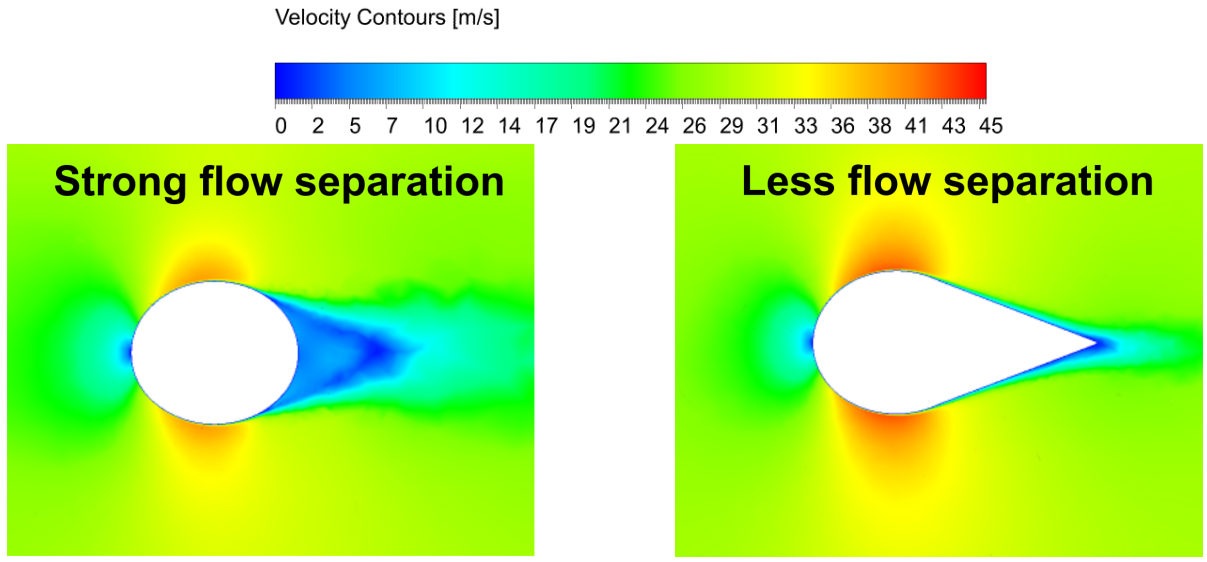

(a) Ellipse cross-tube (b) Airfoil cross-tube

Figure 17.3: Velocity contours for different cross-tubes at (V_{be}) at zero pitch.

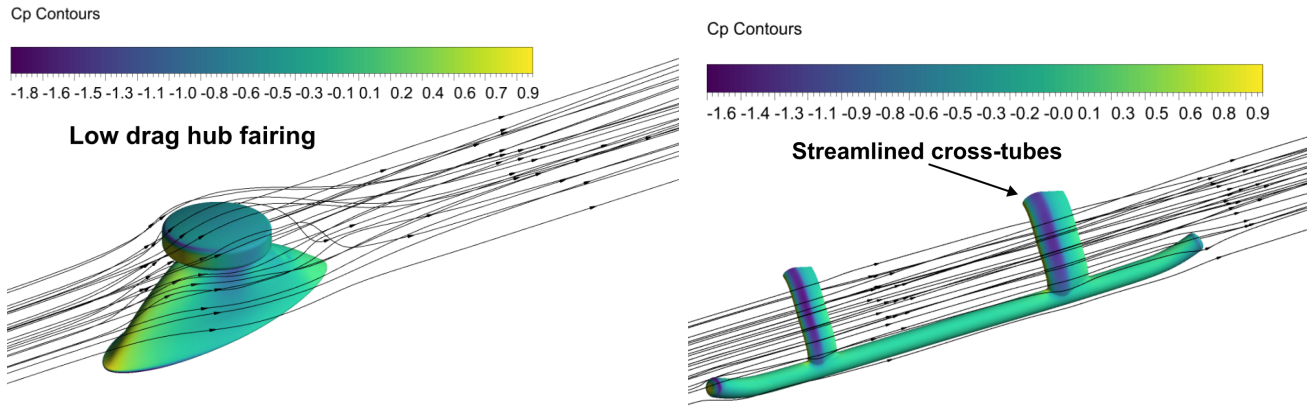

(a) Main rotor hub fairing (b) Landing gear

Figure 17.4: Flow streamlines (including pressure coefficient) for main rotor hub and landing gear at V_{be} at zero pitch.

17.3 Airframe Aerodynamic Metrics

The airframe equivalent areas and volumes at V_{be} are presented in Table 17.3, encompassing only fuselage, landing gear, and rotor hubs as specified in the RFP. All the results are provided at zero pitch and zero yaw angle. The lift area is negative due to the non-lifting nature of the fuselage, landing gear, and rotor hubs (around 1% of GTOW). The airframe drag area and pitching moment volume are within the expected range [75].

Table 17.3: Airframe aerodynamic metrics at V_{be} with 0°pitch and yaw

Metrics	m^2	ft^2
Lift area (L/q)	-0.287	-3.094
Drag area (D/q)	0.422	4.541
L/D	-0.686	
	m^3	ft^3
Pitching moment volume (M/q)	-2.514	-88.794

17.4 Hover Performance

Wyvern is optimized for long-endurance cruise rather than sustained hover; accordingly, the PEMFC propulsion system is sized to the maximum continuous power

(MCP) of the mission-outlined vertical climb leg. The installed stack delivers a gross power of 210 kW (282 hp) MCP at SL /ISA, supplemented by a 67 kW (90 hp) Li-ion buffer battery that supports peak power requirements. The MCP was set based on the High Temperature Cooling (HTC) system capabilities at the SL/ISA condition. However, the stack is enabled to deliver a maximum power of 218 kW (292 hp), and the battery can also handle short transients (maximum 100 kW (134 hp) in 30 s to 60 s) such as take-off, landing, maneuvers, and gust rejection. Figure 17.5 plots the Weight-Altitude-Temperature (WAT) chart at SL /ISA and ISA +20 as a function of gross weight. At the design gross take-off weight (DGW) of 1648 kg (3633 lbs), *Wyvern* can sustain HOGE to approximately 1390 m (4560 ft) under SL /ISA conditions before MCP is exhausted. The maximum power from the stack drops with altitude as the operating stack pressure drops. However, the HTC system gets more efficient as the outside air temperature (OAT) drops with altitude. At GTOW, the ceiling falls to 0 m under ISA +20 condition, as the OAT increases by 20°C (68°F), the HTC capability limits the HOGE performance. Hover capacity improves markedly with minimal weight off-load: at 95 % design GTOW at the SL / ISA, ceiling exceeds 3620 m (11877 ft) (before rotor stalls), providing adequate margin for confined-area landings at moderate altitudes.

17.5 Forward Flight Performance

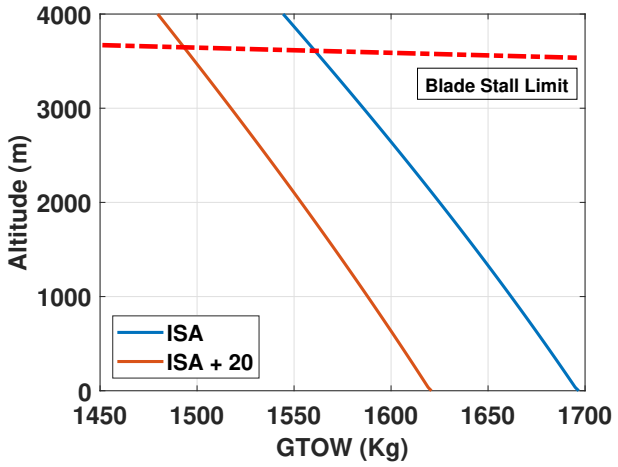

Figure 17.5: HOGE ceiling at SL/ISA, and ISA+20

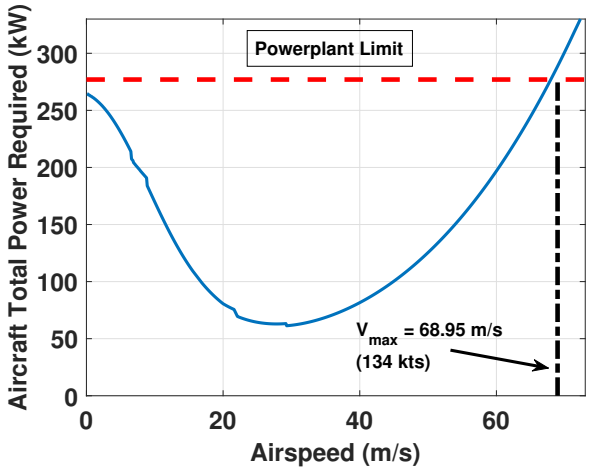

Figure 17.6: Aircraft power at SL/ISA highlighting maximum level flight speed

Cruise efficiency is a primary design driver for *Wyvern*, whose mission includes a 4.5 hours outbound loiter leg over the Alligator River wildlife zone. To achieve this, *Wyvern*'s rotor, box wing, fuselage, and skid landing gear were all aerodynamically streamlined to minimize parasitic drag while maintaining stability and structural integrity during long-endurance flight. Forward flight performance was evaluated at the design gross takeoff weight of 1648 kg (3633 lbs) at SL/ISA condition.

Figure 17.6 shows the total aircraft required power from hover to the maximum flight speed at SL, ISA at GTOW, where the RPM and blade loading variation with advance ratio have been taken into account to find the optimal trim at each flight condition. As the maximum continuous power from the propulsion system is limited to 277 kW (371 hp), the maximum flight speed is restricted to 68.95 m/s (134 knots). The powerplant limitation appeared before the motor power and torque limitations.

Figure 17.7 presents the variation of the main rotor total shaft power required with forward speed up to the maximum flight speed. It also shows the required power breakdown as induced, profile, and the propulsive power. The best endurance speed (V_{be}) occurs at approximately 29.3 m/s (57 knots), where *Wyvern* operates during loiter to maximize the endurance. The best range speed (V_{br}) is observed near

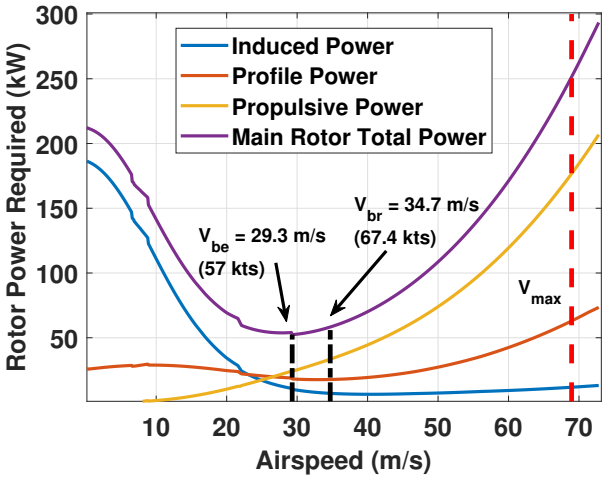

Figure 17.7: Rotor power at SL/ISA

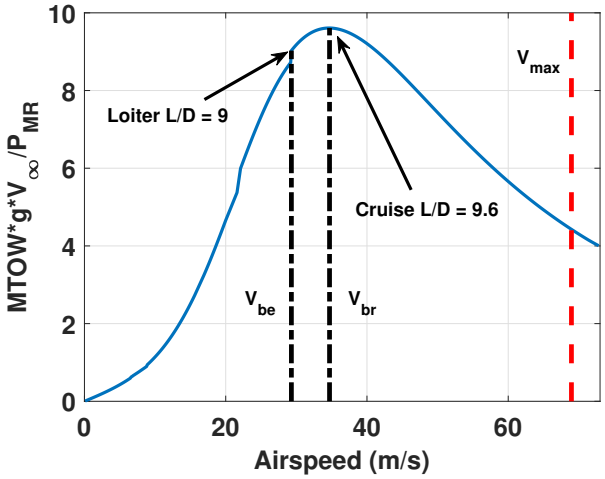

Figure 17.8: Rotor L/D at SL/ISA

34.7 m/s (67.4 knots), used during the outbound and return cruise segments to optimize energy efficiency within the mission. As shown in Figure 17.8, the peak lift-to-drag (= 9.61) ratio occurs near V_{br}, where both the rotor and wing contribute efficiently to lift with minimal fuselage drag. *Wyvern* is designed to operate at V_{be} for the loiter segment, where the $(L/D)_e = (GTOW \cdot g \cdot V/P_{MR})$ achieved is 9.03. At this condition, the full aircraft L/D is given by $(L/D)_{AC} = (GTOW \cdot g \cdot V/P_{Total}) = 7.5$. At higher speeds, the wing lift share increases (55% during loiter, 60% during cruise), causing the fuselage to pitch forward and operate at less favorable angles of attack, thereby increasing flat plate drag and reducing L/D. The electric drive unloads the rotor substantially during cruise, reducing profile power and allowing the rotor to operate at lower angles of attack. This improves L/D and keeps the PEMFC power draw low.

17.6 Payload and Endurance

Payload–endurance curve for *Wyvern* illustrates the tradeoff between mission duration or distance and onboard payload capacity, governed by the energy available from the gaseous hydrogen fuel and the total allowable takeoff weight. As shown in Figure 17.9, Wyvern achieves a maximum loiter endurance of 4.5 hours at SL, ISA while carrying a full mission payload of 185 kg (408 lbs). This endurance is achieved by operating near the PEMFC's optimal efficiency point and flying at the velocity for best endurance (V_{be}), with minimal parasitic drag due to its lift-compound aerodynamic layout. The limits extend from 551 kg (1214 lbs) for no loiter to 6.9 hours loiter at no payload, keeping the rest of the mission profile intact.

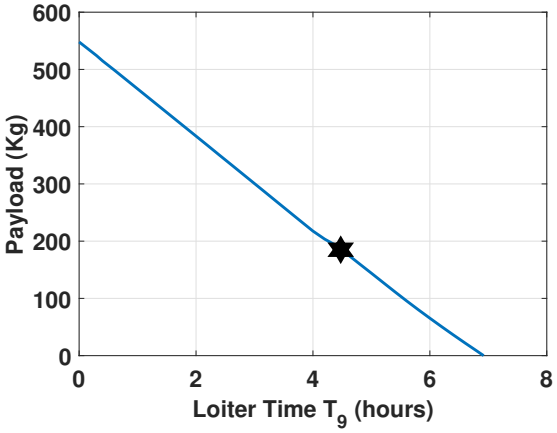

Figure 17.9: Payload Endurance Performance

17.7 Autorotation Performance

All helicopters must demonstrate autorotation capability as a fundamental safety requirement for certification. Despite being a lift-compounded rotorcraft with large wings, *Wyvern* fully meets this requirement and

retains the ability to perform safe, controlled autorotation in the event of complete power loss. The unique floilers mechanism is designed to destroy the wing lift during the autorotation, facilitating the vehicle to perform a typical helicopter autorotation. The vehicle's rotor system is specifically designed to ensure sufficient stored kinetic energy, enabling stable descent and flare during emergency landings. Figure 17.10 shows *Wyvern* demonstrates a competitive Autorotation Index [AI] of 18.5 (here Sikorsky AI index is indicated), confirming its robust autorotational performance comparable to conventional helicopters.

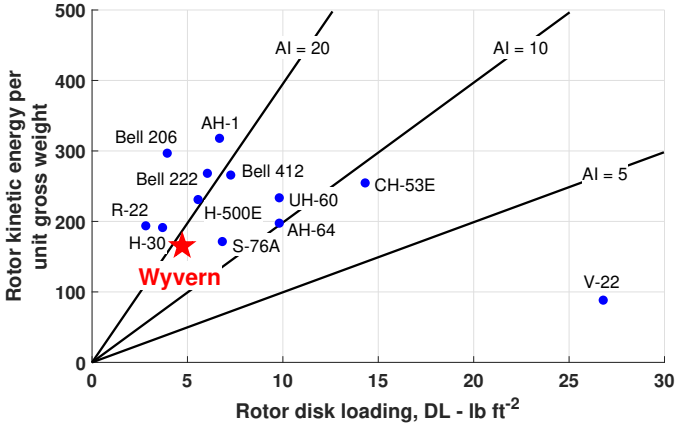

Figure 17.10: Autorotation performance of *Wyvern*

17.8 Mission-specific Performance

Table 17.4 shows the mission-specific performance for *Wyvern*. The segment-wise aerodynamic power is provided, which includes the main rotor and the tail rotor power. Next, the total power is provided, which includes the transmission efficiency losses (including motor and drivetrain efficiency), along with the avionics (1.2 kW) (1.6 hp) and other accessories' power (3%). Each motor RPM, along with the motor torque, is shown, indicating the variation of the speeds in different segments. The motor efficiencies are accordingly calculated from the efficiency chart of the HPDM-180R [77]. The drivetrain efficiency remained consistent at 98%. The maximum power required during the mission from the propulsion system is 271.61 kW (363 hp), which leaves a 2% margin from the maximum continuous power available of 277 kW (371 hp) and 17.3% from the maximum power available of 318.5 kW (426 hp). Table 17.5 shows the PEMFC performance data for each segment. The PEMFC provided power is shown, indicating the fuel cell efficiency ($\eta = v/E_r$). It can be noted that the PEMFC operated at its highest efficiency during the loiter and the cruise segments compared to the other segments, ensuring the least thermal output. The H_2 SFC, consumption rate, and the net consumption are shown accordingly. The mission time in segment 9 indicated the unprecedented endurance performance for *Wyvern*, having a 4.48 hours of loiter, with only 24.8 kg (55 lbs) of gaseous H_2, considering 98% utilization.

18 Failure Mode Analysis

While preventative measures such as scheduled inspections, predictive maintenance, and robust component monitoring are the most effective means of ensuring system reliability and protecting both aircraft and crew, unforeseen failures can still occur. To systematically assess the risks and guide mitigation strategies, a comprehensive Failure Modes, Effects, and Criticality Analysis (FMECA) was conducted for *Wyvern*. Table 18.1 summarizes the degree of impact on mission or safety (rated I to V) for each identified failure mode. Tables 18.2 through 18.4 detail each failure mode in the corresponding subsystem, along with consequences and mitigation strategies associated with each failure. The failure modes were subdivided into the Propulsion system (Table 18.2), the High Temperature Cooling system (Table 18.3), the Flight Control system (Table 18.4), and the Transmission system (Table 18.5).

This failure pertains to a single-point failure in the fuel cell power distribution, which could result in reduced power availability. However, this has been mitigated by battery redundancy capable of supporting safe flight and landing for a predefined emergency duration. In addition, all Level-II or Level-III risks were either redundantly designed, monitored through onboard diagnostics, or rendered non-critical through

Table 17.4: Mission-specific vehicle performance data

Segment	Aerodynamic Power kW (hp)	Total Power kW (hp)	Motor RPM	Motor Torque Nm (lbf-ft)	Transmission Efficiency
1	–	3 (4)	–	–	–
2	161 (215)	180 (242)	2342	364 (269)	0.924
3	237 (317)	272 (364)	2342	551 (406)	0.900
4	231 (310)	265 (355)	2342	537 (396)	0.902
5	168 (226)	191 (256)	2032	445 (328)	0.913
6	61 (81)	69 (92)	1521	211 (156)	0.927
7	–	1.5 (2)	–	–	–
8	231 (309)	265 (355)	2342	536 (396)	0.901
9	54 (73)	62 (83)	1582	184 (136)	0.928
10	165 (222)	188 (252)	2032	438 (323)	0.913
11	60 (80)	68 (91)	1521	208 (153)	0.927
12	63 (85)	72 (97)	2342	144 (106)	0.921
13	227 (305)	260 (349)	2342	527 (389)	0.903
14	223 (299)	255 (342)	2342	517 (382)	0.904
15	158 (211)	177 (237)	2342	357 (264)	0.924
16	–	3 (4)	–	–	–

Table 17.5: Mission-specific PEMFC performance data

Mission Segment	Mission Time (min)	PEMFC Power kW (hp)	PEMFC Efficiency (%)	H_2 Flow Rate kg/hr (lb/hr)	H_2 Consumption kg (lb)	
1	0.17	—	—	—	—	—
2	0.25	180 (242)	0.43	12 (27)	0.05 (0.11)	
3	1.32	208 (280)	0.40	15 (33)	0.33 (0.72)	
4	0.17	206 (276)	0.40	15 (32)	0.041 (0.09)	
5	0.78	191 (256)	0.42	13 (29)	0.17 (0.38)	
6	13.13	69 (92)	0.51	5 (11)	1.09 (2.4)	
7	0.59	—	—	—	—	—
8	0.5	207 (277)	0.4	15 (32)	0.12 (0.27)	
9	269	62 (84)	0.51	5 (10)	21 (46)	
10	0.87	188 (252)	0.42	13 (28)	0.19 (0.41)	
11	12.27	68 (91)	0.51	5 (11)	1 (2)	
12	1.16	72 (97)	0.51	5 (11)	0.1 (0.2)	
13	0.17	192 (258)	0.42	13 (29)	0.44 (0.97)	
14	2	195 (261)	0.42	13 (30)	0.057 (0.13)	
15	0.25	177 (237)	0.43	12 (26)	—	
16	0.17	—	—	—	—	—

mission planning constraints (e.g., avoiding hover segments late in the mission if recharge is unavailable). Overall, the FMECA confirms that *Wyvern*'s system architecture meets an acceptable safety threshold. The integrated hybrid-electric propulsion, modular power system design, and composite damage-tolerant structures contribute to high mission reliability, even in the event of isolated subsystem failures.

Table 18.1: Impact level classification

Level of Impact	**Description**
I	Catastrophic - loss of life possible
II	Major concern - vehicle unrecoverable
III	Moderate concern - failure to complete mission
IV	Low concern - modified mission segment
V	No concern - Mission completed as planned

Table 18.2: FMECA for PEMFC + Battery + H2 tank system

Failure Mode	**Impact**	**Consequence**	**Mitigation**
Hydrogen Fuel Cell Failure	II	Not possible to fly below V_{be}	The flight battery can provide enough power to fly at V_{be} for ∼6.7 minutes. Land as soon as possible, run-on landing only.
Flight Battery Failure	III	Not possible to hover OGE	The fuel cell can provide enough power to fly above 25kts. Land as soon as practical, run-on landing only.
Air Intake Fan Failure	II	Failure of the fuel cell is imminent. Not possible to fly below V_{be}.	The flight battery will provide the power. Land as soon as possible, run-on landing only.
High Voltage DC/DC Converter Failure	III	Reduction of maximum torque from the motor by a factor of two. Unable to hover.	Emergency bypass shorts the fuel cell and battery to the motors. Land as soon as practical. Run-on landing only.
Single H_2 Regulator Blocked	III	Unable to use all the fuel.	Land before the fuel in the other tank runs out.

Table 18.3: FMECA for high temperature cooling system

Failure Mode	**Impact**	**Consequence**	**Mitigation**
One Radiator clogged	III	One motor and one power source will overheat imminently.	Flight-critical components are on separate cooling circuits. Land as soon as possible.
Dual Radiator clogged	I	All power sources and motors are in danger of overheating	Land as soon as possible. Be prepared to autorotate. Autorotation is shown to be possible in Wyvern by destroying the wing lift through flaps.
Single Thermostat Blocks the radiator	III	One motor and one power source will overheat imminently.	Flight-critical components are on separate cooling circuits. Land as soon as possible.
Coolant Pump Failure	I	All power sources and motors are in danger of overheating	Land as soon as possible. Be prepared to autorotate.

Table 18.4: FMECA for flight control system

Failure Mode	**Impact**	**Consequence**	**Mitigation**
Hydraulic servo failure (partial or complete)	IV	Not possible to fly at higher flight speeds or hover because of an increase in control loads.	Reach the V_{be} speed, then turn off the hydraulic system. Perform a shallow approach and land, run-on landing only.
SAS failure (servo, flight computer, sensors)	V	Pilot manually control the vehicle and increases the pilot workload	Immediately disengage the SAS, and carefully monitor pilot workload

Table 18.5: FMECA for drivetrain system

Failure Mode	**Impact**	**Consequence**	**Mitigation**
Single Motor Failure	III	Aircraft drive power is limited to 180 kW (241 hp) (70%). Hover is not possible. Cannot fly below ∼25kts.	Dual motor drivetrain. Declutch the failed motor. The single motor will provide enough power to fly above ∼25kts. Land as soon as practical, run-on landing only.
Dual Motor Failure	I	Not possible to maintain flight.	Land as soon as possible. Be prepared to autorotate.
MRGB oil leak	III	Increased friction, overheating, and possible catastrophic failure of the MGB.	Land as soon as possible. The gearbox has 30 minutes of dry-running capabilities.
Hydraulic Pump Failure	IV	Not possible to fly at higher flight speeds or hover because of increased control loads.	Reach the V_{be} speed, then turn off the hydraulic system. Perform a shallow approach and land, run-on landing only.

19 Acoustics

The main objective of the aircraft is to loiter for the longest time but it is also important to keep the noise levels low, especially during loiter. The tip speed of the main rotor is highest at hover and reduces during loiter. Therefore, a conservative approach is used in this analysis where the highest tip speed and blade load distribution of the mission (hover) is used for acoustic analysis. This study determines the maximum noise level of the mission. The main source of noise for this type of aircraft is tonal noise. Tonal noise has contributions from thickness and loading noise.

The aircraft's noise levels are analyzed using Acoustic Code of the University of Maryland (ACUM), which is an in-house developed acoustic code for rotorcraft applications. The tonal noise is calculated based on Farassat's formulation of the Ffowcs Williams-Hawkings equation [78,79]. The sectional aerodynamic data for the main rotor blade are extracted from UMARC-II, and the noise level is computed at 700 different observer locations. These locations are set in a hemisphere below the aircraft of radius 60 m (197 ft) where *Wyvern* hover out of ground effect. The results are presented in Figure 19.1. The analysis revealed that the maximum tonal noise is 70 dB, which is well within acceptable limits for humans.

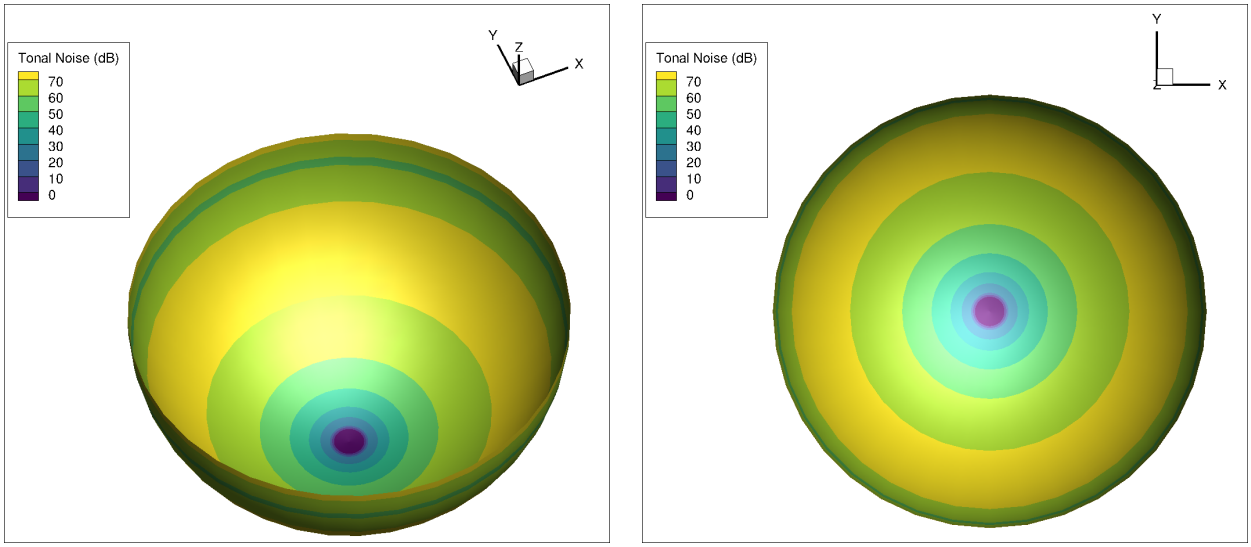

(a) Isometric view of noise levels

(b) Top view of noise levels

Figure 19.1: Overall noise level during hover

20 Life Cycle Cost Analysis

*Wyvern*is an unique aircraft where traditional cost models are likely not accurate. Nevertheless, a baseline can be drawn based on current data. *Wyvern* purchase, maintenance, and operational costs were estimated using the Harris-Scully cost model, as provided in the NDARC manual [23], [80], and [81]. Harris-Scully predicts purchase prices of 96% of 128 rotorcraft within 20%.

The purchase price of the aircraft has been estimated using the Harris-Scully cost model [23]. The model includes adjustments for various factors, including empty weight, engine type, landing gear, and number of main rotors. The calculated price also accounts for the known costs of the specialized avionics and electrical components. The fuel cell system cost is included using the model mentioned in [80]. Using these models, the aircraft purchase price is estimated to be **1,193,000 USD**.

Maintenance costs include labor, parts (airframe, engine, and avionics), engine overhaul, and major periodic maintenance costs. The maintenance cost for average practice is estimated using the Harris model [23] to

be **734 USD per flight hour**, with 1.5 maintenance man-hours per flight hour and a technology factor of 1.

The operational cost is estimated using a statistical relationship with aircraft purchase price [24], as well as the estimated fuel and maintenance costs [82]. The operational cost was calculated assuming two missions are flown per day. With this, the estimated operational cost is **840,000 USD per year**, including estimated crew, insurance, depreciation, and finance costs of 250,000 USD per year.

21 Additional Mission Capabilities

Wyvern is capable of loitering for about 4.5 hours identifying its capability for extremely long flight endurance for its category. For this amazing capability, it can also be used in a number of other applications, including Aerial Survey, Aerial Journalism, and Wildfire Command and Control.

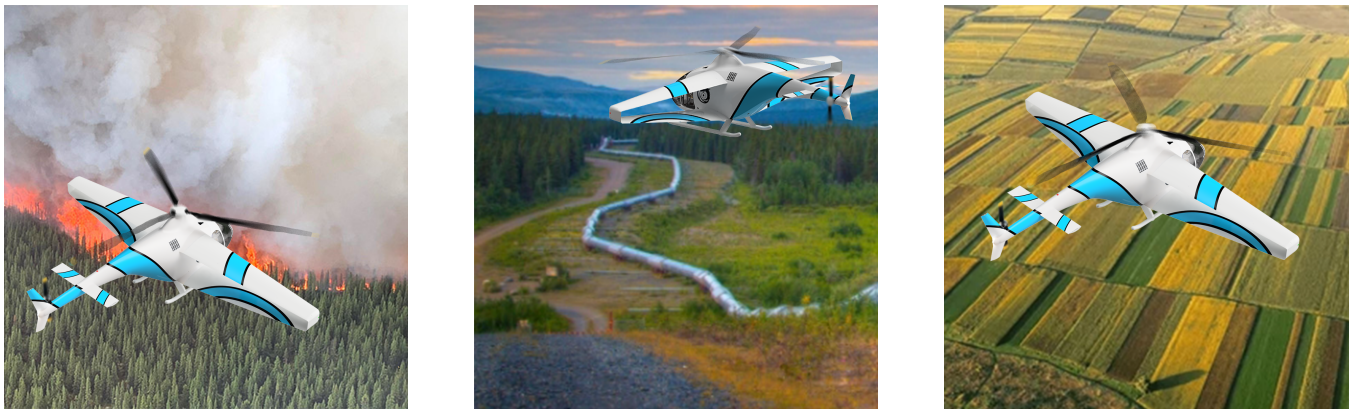

(a) Wildfire Control (b) Aerial Survey (c) Crop-dusting

Figure 21.1: Alternative missions

21.1 Wildfire Command And Control

In addition to its aerial survey and journalism capabilities, *Wyvern* can be adapted for **Wildfire Command And Control**. Every year, tens of thousands of wildfires burn across America, with the US routinely spending more than $1 billion per year to fight them. Along with the warming climate, the wildfire threat continues to increase, with the potenial of causing harm to property, livelihoods, and human health [83]. Due to its ability to remain on station for over four hours, *Wyvern* is ideally suited to serve as an aerial command center for firefighters, controlling the air assets as they attempt to extinguish the blaze.

21.2 Aerial Survey

Wyvern, with its innovative box-wing design and exceptional loitering capability, is ideally suited for **Aerial Survey missions**, offering a stable platform ideal for data collection and real-time surveillance. *Wyvern* can be used to conduct topographical surveys for mapping over large areas of land. Furthermore, the long on-station time of the aircraft is aptly suited for border security missions. Other possible uses include power line, rail, or highway inspection.

21.3 Crop-dusting

Wyvern is also well-suited for **Crop Dusting missions**. Its ability to remain airborne for extended durations enables efficient application of pesticides and other agricultural products. As an added benefit, *Wyvern* doesn't deposit toxic emissions onto food crops. To hold extra fluid, one hydrogen tank could be removed and replaced with a large storage volume.

22 Summary

In response to the 42nd Annual VFS Student Design Competition, the *University of Maryland's Graduate Design Team* presents ***Wyvern***—a cutting-edge, hydrogen-powered electric wing compound rotorcraft engineered to deliver **maximum loiter**, with no emissions but water vapor, and **certifiable reliability** for next-generation VTOL tour and sightseeing missions. *Wyvern* embodies the spirit of innovation through bold and desruptive design.

At its core, *Wyvern* fuses an **electrically driven slowed rotor configuration**—a single 10 m (33 ft) diameter main rotor paired with a high-aspect-ratio **box-wing**—with an all electric **PEMFC hybrid powerplant** operating on 700 bar compressed gaseous hydrogen as clean fuel. This design achieves over **5 hours of flight time**, including **4.5 hours of loiter** at 30 m (98.4 ft) MSL, while carrying a **185 kg (408 lbs) full payload**, with **no emissions but water vapor**.

Key innovations drive this performance:

- **Aerodynamics**: The box wing offloads up to 60% of rotor lift in cruise, yielding an **L/D > 9.5**, while the optimized rotor achieves a **Figure of Merit > 0.785**.
- **Propulsion**: A 210 kW (281 hp) PEMFC stack and a 6.7 kWh 10C-rated buffer battery combine to a 795 V DC bus, which powers two direct-drive 180 kW (241 hp) PMSMs, delivering high shaft efficiency with no gearbox losses and enhanced autorotation.
- **Cooling**: A compact, water-cooled thermal management system keeps the stack below 90 °C (194°F) using 150 kW (201 hp) compact radiators and a high-flow axial fan, even during hover.
- **Structures**: A CFRP semi-monocoque fuselage, faired hub, and ultra-light rotor transmission compress structural weight fraction to **0.47** at MTOW 1648 kg (3633 lbs), aided by **composite elements** and **supercritical shafting**.
- **Safety & Redundancy**: Redundant cooling, crashworthy tanks, stack diagnostics, and a stability augmentation system ensure **single-point-failure tolerance** and alignment with **EASA CS-27 certification** pathways.

Designed to operate from the **Wright Brothers National Memorial** to the **Alligator River Wildlife Refuge**, *Wyvern* embodies the spirit of innovation at the dawn of flight with a relatively high-TRL (≥ 6) solution that aspire to establish a new mode of **quiet, clean, and certifiable** vertical flight of the future. With its **flame-free, turbine-matching performance**, *Wyvern* aspire to be a visionary leap toward **sustainable rotorcraft aviation**.

References

[1] International Air Transport Association (IATA), "Net Zero Carbon 2050 Resolution," 77th Annual General Meeting, October 2021, Accessed: 2025-05-29.

[2] International Civil Aviation Organization (ICAO), "Long-Term Aspirational Goal for International Aviation for Net-Zero Carbon Emissions by 2050," 41st Assembly, September 2022, Held 25–28 September. Accessed: 2025-05-29.

[3] Garver, B., Rutherford, D., and Zheng, S., "CO2 Emissions From Commercial Aviation," *International Council on Clean Transportation*, 2020.

[4] Shell and Deloitte, "Decarbonizing Aviation: Clear for Take-off — Industry Perspectives," 2022, Accessed: 2025-05-29.

[5] U.S. Congress, "H.R. 3935 Enrolled Bill – FAA Reauthorization Act of 2024," U.S. Public Law No: 118-63, May 2024, Accessed: 2025-05-29.

[6] Lapena-Rey, N., Mosquera, J., Bataller, E., and Ort, F., "First Fuel-Cell Manned Aircraft," *AIAA Journal of Aircraft*, Vol. 47, No. 6, 2010, pp. 1825–1835.

[7] Romeo, G., Borello, F., Correa, G., and Cestino, E., "ENFICA-FC: Design of Transport Aircraft Powered by Fuel Cell and Flight Test of Zero Emission 2-Seater Aircraft Powered by Fuel Cells Fueled by Hydrogen," *International Journal of Hydrogen Energy*, Vol. 38, No. 1, 2013, pp. 469–479.

[8] Kallo, J., Flade, S., Stephan, T., and Schirmer, J., "Antares DLR H2 Test Bed for Electric Propulsion," *53rd AIAA Aerospace Sciences Meeting*, No. AIAA 2015-1305, AIAA, January 2015.

[9] Flade, S., Stephan, T., Thalau, O., Burberg, T., Schirmer, J., and Kallo, J., "Air Breathing (PEM) Fuel Cells in Aviation," *ECS Transactions*, Vol. 75, No. 14, September 2016, pp. 471–477.

[10] Datta, A. and Johnson, W., "Requirements for a Hydrogen Powered All-Electric Manned Helicopter," *12th AIAA Aviation Technology, Integration, and Operations (ATIO) Conference and 14th AIAA/ISSMO Multidisciplinary Analysis and Optimization Conference*, No. AIAA 2012-5405, AIAA, Indianapolis, IN, September 2012.

[11] Datta, A. and Johnson, W., "Power Plant Design and Performance Analysis of a Manned All-Electric Helicopter," *AIAA Journal of Propulsion and Power*, Vol. 30, No. 2, March 2014, pp. 610–622.

[12] Moffitt, B. A. and Zaffou, R., "Polymer-Electrolyte Fuel Cells for UAV Applications Providing Solutions to Revolutionize UAVs," *SAE Power Systems Conference*, No. 2012-01-2161, Phoenix, AZ, October 2012, Held October 30–November 1.

[13] Hirschberg, M., "Flying in the Skai with Hydrogen," *Vertiflite*, Vol. 65, No. 4, July/August 2019.

[14] Moorman, R. W., "Future Fuel: HyPoint's Hydrogen Revolution," *Vertiflite*, Vol. 67, No. 5, September/October 2021.

[15] Swartz, K. I., "Piasecki Relaunches the Heliplex," *Vertiflite*, Vol. 69, No. 4, July/August 2023.

[16] Host, P., "Hydrogen Begins to Take Off," *Vertiflite*, Vol. 70, No. 4, July/August 2024.

[17] Hein, T. and Hickman, D., "Education on Hydrogen Use Critical to the Rise of Hydrogen Aviation," *Vertical Magazine*, May 2023.

[18] Hirschberg, M., "Hydrogen is a Game Changer for Vertical Flight," *Forbes Aerospace & Defense*, July 2024.

[19] Warwick, G., "Joby Beats Range Target for Hydrogen-Electric Air Taxi Demonstrator," *Aviation Week*, July 2024.

[20] Swartz, K. I., "Unither Bioelectronics and Robinson Helicopter Partner on Hydrogen," *Vertiflite*,

Vol. 70, No. 4, September/October 2024.

[21] Maurya, S., Chopra, I., and Datta, A., "Steady and Unsteady Hover Test of a Lift Compounding Rotorcraft," *Journal of Aircraft*, Vol. 60, No. 1, January 2023, pp. 130–142.

[22] Uppoor, V., Zheng, H., and Chopra, I., "High Advance Ratio Wind Tunnel Testing of a Slowed Mach-Scaled Rotor with Full-Wing and Trailing Propeller Lift and Thrust Compounding," *Proceedings of the 81st Annual Forum of the Vertical Flight Society (VFS)*, Virginia Beach, VA, May 2025, Held May 20–22.

[23] Johnson, W., "NDARC: NASA Design and Analysis of Rotorcraft," NASA-TP 20220000355, Mar. 2023.

[24] Harris, F. D., "Introduction to Autogyros, Helicopter, and Other V/STOL Aircraft," NASA-SP 2012-215959, Oct 2012.

[25] Landgrebe, A. J., "An analytical and experimental investigation of helicopter rotor hover performance and wake geometry characteristics," , No. AD0728835, 1971.

[26] Johnson, W., Silva, C., and Solis, E., "Concept vehicles for VTOL air taxi operations," *AHS Specialists"Conference on Aeromechanics Design for Transformative Vertical Flight*, No. ARC-E-DAA-TN50731, 2018.

[27] Datta, A., "PEM fuel cell model for conceptual design of hydrogen eVTOL aircraft," , No. 20210000284, Jan. 2021.

[28] Ahluwalia, R. K., Wang, X., and Steinbach, A., "Performance of advanced automotive fuel cell systems with heat rejection constraint," *Journal of Power Sources*, Vol. 309, 2016, pp. 178–191.

[29] Horizon Educational, "Liquid Cooled Fuel Cell Stacks," 2025, Accessed: 2025-05-22.

[30] Bousman, W. G., *Airfoil Dynamic Stall and Rotorcraft Maneuverability*, No. 209601, 2000.

[31] Harris, F. D., "Rotor performance at high advance ratio: theory versus test," Tech. Rep. NASA/CR-2008-215370.

[32] Kaplan, N., Patil, M., Chopra, I., and Datta, A., "Wind Tunnel Testing and Aeromechanics Predictions on Slowed Mach-Scaled Thrust Compounding Rotorcraft with a Trailing Propeller," *Journal of the American Helicopter Society*, Vol. 70, No. 1, January 2025, pp. 1–14.

[33] Uppoor, V., Patil, M., and Chopra, I., "Wind Tunnel Testing of a Slowed Mach-scaled Hingeless Rotor with Lift and Thrust Compounding," *Proceedings of the Vertical Flight Society (VFS) 6th Decennial Aeromechanics Specialists Conference*, Santa Clara, CA, Feb 2024.

[34] Cho, S. H., Gonzalez, V., Bhandari, S., Tischler, M., and Cheung, K., "Hover/Low Speed Dynamics Model Identification of a Coaxial Tricopter in Hover using Joint Input-Output Technique," *Vertical Flight Society 75th Annual Forum*, Vol. 5, 2019.

[35] Gul, S. and Datta, A., "Development of an aeromechanics solver for loads and stability of hingeless tiltrotors," *Journal of Aircraft*, Vol. 60, No. 1, 2023, pp. 143–159.

[36] Anand, A., Safdar, M. M., Marepally, K., and Baeder, J. D., "A Comprehensive Review of Neural Network Training Approaches for Airfoil Design and Optimization," *AIAA SCITECH 2025 Forum*, 2025, p. 0271.

[37] Anand, A., Marepally, K., Safdar, M. M., Lee, B., and Baeder, J. D., "Generalizable deep learning module for rotorcraft inverse design applications," *AIAA SCITECH 2024 Forum*, 2024, p. 0460.

[38] Anand, A., Marepally, K., and Baeder, J. D., "Deep Learning Framework for Design and Optimization of Rotor Blades," *VFS Forum*, Vol. 80, 2024.

[39] Hélicoptères Guimbal, "Cabri G2," 2025, Accessed: 2025-05-28.

[40] Donguy, P., "Development of a helicopter rotor hub elastomeric bearing," *Journal of Aircraft*, Vol. 17, No. 5, 1980, pp. 346–350.

[41] Falls, J., Datta, A., and Chopra, I., "Integrated Trailing-Edge Flaps and Servotabs for Helicopter Primary Control," *Journal of the American Helicopter Society*, Vol. 55, No. 3, 2007.

[42] Mcgeer, B. T. and Von Flotow, A. H., "Variable-twist rotor blade controlled by hub pitch angle and rotational speed," U.S. Patent 7857598B2, Dec. 2010.

[43] Robinson Helicopter Company, "R44 Maintenance Manual – Flight Controls," 2011, Accessed: 2025-05-26.

[44] Jude, D., Lee, B., Jung, Y. S., Petermann, J., Govindarajan, B. M., and Baeder, J. D., "Application of a Heterogeneous CFD Framework Towards Simulating Complete Rotorcraft Configurations," *Proceedings of the Vertical Flight Society 74th Annual Forum*, 2018.

[45] Schiktanz, D. and Scholz, D., "Box wing fundamentals—An aircraft design perspective," *DGLR Dtsch. Luft-und*, 2011, pp. 601–615.

[46] Bainbridge, D., Bacharoudis, K., Cini, A., Turner, A., Popov, A., and Ratchev, S., "Advanced assembly solutions for the airbus RACER joined-wing configuration," Tech. rep., SAE Technical Paper, 2019.

[47] Edwards, J. W. and Wieseman, C. D., "Flutter and divergence analysis using the generalized aeroelastic analysis method," *Journal of Aircraft*, Vol. 45, No. 3, 2008, pp. 906–915.

[48] Lynn, R., "Wing-rotor interactions," *Journal of Sound and Vibration*, Vol. 4, No. 3, 1966, pp. 388–402.

[49] White, W., "Unanticipated Right Yaw in Helicopters," FAA Advisory Circular AC 90-95, Dec. 1995.

[50] National Transportation Safety Board, "Loss of Tail Rotor Effectiveness in Helicopters," NTSB Safety Alert SA-062, Mar. 2017.

[51] Prouty, R. W., *Military Helicopter Design Technology*, Krieger Publishing Company, 1998.

[52] Sinnige, T., Nederlof, R., and van Arnhem, N., *Aerodynamic Performance of Wingtip-Mounted Propellers in Tractor and Pusher Configuration*.

[53] Robinson Helicopter Company, "Robinson R22 Illustrated Parts Catalog," Robinson catalog, May 2021.

[54] Wiesner, W., "Tail Rotor Design Guide," Boeing Vertol Company. Prepared for the Army Air Mobility Research and Development Laboratory AD-775391, Jan 1974.

[55] Naval Air Systems Command, "Structural Design Requirments (Helicopters)," Department of the Navy AR-56, 17 Feb. 1970.

[56] Prasad, N., Gokhale, A., and Wanhill, R., *Aluminum-Lithium Alloys: Processing, Properties, and Applications*, Elsevier Science, 2013.

[57] Tishchenko, M. N., Nagaraj, V. T., and Chopra, I., "Preliminary design of transport helicopters," *Journal of the American Helicopter Society*, Vol. 48, No. 2, 2003, pp. 71–79.

[58] Chernoff, M., "Analysis and Design of Skid Gears for Level Landing," *Journal of the American Helicopter Society*, Vol. 7, No. 1, 1962, pp. 33–39.

[59] Ng, W., Patil, M., and Datta, A., "Hydrogen Fuel Cell and Battery Hybrid Architecture for Range Extension of Electric VTOL (eVTOL) Aircraft," *Journal of the American Helicopter Society*, Vol. 66, 2021.

[60] Ng, W. and Datta, A., "Hydrogen Fuel Cells and Batteries for Electric-Vertical Takeoff and Landing Aircraft," *Journal of Aircraft*, Vol. 56, No. 5, September/October 2019, pp. 1765–1782.

[61] Artyushkova, K., Reshetenko, T., Roth, C., Santoro, C., Serov, A., André, J., and Chatenet, M., "Editorial for the Virtual Special Issue of Journal of Power Sources "Low temperature fuel cells and electrolysers" - Science and Engineering: let's play this game hand in hand!" *Journal Of Power Sources*, 2022.

[62] Datta, A. and Johnson, W., "Powerplant Design and Performance Analysis of a Manned All-Electric Helicopter," *Journal of Propulsion*, Vol. 30, No. 2, February 2014, pp. 490–505.

[63] Takahashi, T., Ikeda, T., Murata, K., Hotaka, O., Hasegawa, S., Tachikawa, Y., Nishihara, M., Matsuda, J., Kitahara, T., Lyth, S. M., et al., "Accelerated durability testing of fuel cell stacks for commercial automotive applications: a case study," *Journal of The Electrochemical Society*, Vol. 169, No. 4, 2022, pp. 044523.

[64] Toyota Motor Corporation, "Toyota Mirai Fuel Cell Vehicle Posters," 2020, Accessed: 2025-05-29.

[65] Mercier, C., Gierczynski, A., and Hanappier, N., "Light helicopter demonstrator with high-compession engine: flight test results," 2017.

[66] Fristam Pumps USA, "FPR Performance Curves Model: 751 (1750 RPM, Inlet 3", Outlet 2")," 2022, Accessed: 2025-05-26.

[67] National Fan Co., "Eagle Heavy Panel Mount Exhaust Fan Specification Sheet," 2025, Accessed: 2025-05-26.

[68] Budynas, R. G., Nisbett, J. K., et al., *Shigley's mechanical engineering design*, Vol. 9, McGraw-Hill New York, 2011.

[69] Lisle, T. J., Little, C. P., Aylott, C. J., and Shaw, B. A., "Bending fatigue strength of aerospace quality gear steels at ambient and elevated temperatures," *International Journal of Fatigue*, Vol. 164, 2022, pp. 107125.

[70] Rashid, H., Place, C., Mba, D., Keong, R., Healey, A., Kleine-Beek, W., and Romano, M., "Reliability model for helicopter main gearbox lubrication system using Influence Diagrams," *Reliability Engineering & System Safety*, Vol. 139, 2015, pp. 50–57.

[71] Gordon, C. C., Blackwell, C. L., Bradtmiller, B., Parham, J. L., Barrientos, P., Paquette, S. P., Corner, B. D., Carson, J. M., Venezia, J. C., Rockwell, B. M., Mucher, M., and Kristensen, S., "2012 Anthropometric Survey of U.S. Army Personnel: Methods and Summary Statistics," Tech. Rep. NATICK/TR-15/007, U.S. Army Natick Soldier Research, Development and Engineering Center, Natick, Massachusetts, 2014.

[72] Pitt, D. M. and Peters, D. A., "Theoretical Prediction of Dynamic-Inflow Derivatives," *Vertica*, Vol. 5, No. 1, Mar. 1981, pp. 21–34.

[73] Saetti, U. and Rogers, J., "Revisited Harmonic Balance Trim Solution Method for Periodically-Forced Aerospace Vehicles," *Journal of Guidance, Control, and Dynamics*, Vol. 44, No. 5, 2021, pp. 1008–1017.

[74] Saetti, U. and Horn, J. F., "Load Alleviation Control Design Using Harmonic Decomposition Models, Rotor State Feedback, and Redundant Control Effectors," *American Helicopter Society 74th Annual Forum Proceedings*, May 14-17, 2018.

[75] Prouty, R. W., *Helicopter Performance, Stability, and Control*, Krieger Publishing Company, Inc., 1st ed., 1986.

[76] Sridharan, A., Chopra, I., and Turnour, S., "Mast Bumping Simulation and Mitigation Analysis for Teetering Rotor Systems," *American Helicopter Society Aeromechanics Design for Transformative Vertical Flight 2018*, 01 2018.

[77] H3X Technologies, "HPDM-180R," 2025, Accessed: 2025-05-26.

[78] Ffowcs Williams, J. E., Hawkings, D. L., and James, L. M., "Sound Generation by Turbulence and Surfaces in Arbitrary Motion," *Philosophical Transactions of the Royal Society of London. Series A, Mathematical and Physical Sciences*, Vol. 264, No. 1151, 1969, pp. 321–342.

[79] Farassat, F., "Linear Acoustic Formulas for Calculation of Rotating Blade Noise," *AIAA Journal*, Vol. 19, No. 9, 1981, pp. 1122–1130.

[80] Ahluwalia, R., Peng, J.-K., Wang, X., Papadias, D., and Kopasz, J., "Performance and cost of fuel cells for urban air mobility," *International Journal of Hydrogen Energy*, Vol. 46, No. 74, 2021, pp. 36917–36929.

[81] Harris, F. D. and Scully, M. P., "Rotorcraft Cost Too Much," *Journal of the American Helicopter Society*, Vol. 43, No. 1, 1998, pp. 3–13.

[82] SP Global Commodity Insights, "California hydrogen pump prices for light-duty vehicles reach new highs," 2024, Accessed: 2025-05-23.

[83] US Environmental Protection Agency, "Climate Change Indicators: Wildfires," Accessed: 2025-05-15.